SYNTHESIS AND STUDY OF 2D ATOMIC CRYSTAL: GRAPHENE FOR NEMS APPLICATIONS

MEENAKSHI ANNAMALAI
B.E (Electrical and Electronics Engineering), GCE, Salem, India
M.Sc. (Microelectronics), NUS, Singapore

A THESIS SUBMITTED

FOR THE DEGREE OF DOCTOR OF PHILOSOPHY

DEPARTMENT OF
ELECTRICAL AND COMPUTER ENGINEERING

NATIONAL UNIVERSITY OF SINGAPORE

2013

DECLARATION

I hereby declare that the thesis is my original work and it has been written by me in its entirety. I have duly acknowledged all the sources of information which have been used in the thesis.

This thesis has also not been submitted for any degree in any university previously.

Meenakshi Annamalai
15th May 2013

ACKNOWLEDGEMENTS

This thesis brings the end of my long four year journey as a PhD student in NUS. There were mixed emotions during this period and I had always felt whether I could sustain this long term commitment due to frequent failures associated with intermittent success. The displeasure linked during my study is undocumented and the words you read in this section represent only my success story. It was because of the multitude of people addressed below, that this dissertation was possible.

At this moment of accomplishment, I would like to thank my supervisor Dr. Moorthi Palaniapan for initiating this study and for his guidance during my study. I am also extremely indebted to Dr. John Thong, deputy head (research and graduate programmes) of ECE department, for providing me with all the research facilities, timely guidance and help when I was facing difficult situations. I would like to express my deep gratitude to Dr. Daniel Pickard for generously providing all the consumables for my research work without expecting anything in return. I also wish to express my very great appreciation to him for providing professional guidance and valuable technical support during the collaborative work. I would like to thank Dr. Venky Venkatesan, director of Nanoscience and Nanotechnology Initiative (NUSNNI), and Dr. Mark Breese, co-director of NUSNNI, for all their technical support during the irradiation study. I owe earnest thankfulness to Dr. Veeravalli Bharadwaj for his constant motivation and moral support. Special thanks go to Dr. Vincent Chengkuo Lee and Dr. Zhu Chunxiang for reviewing my PhD proposal and providing me with valuable suggestions. Their heartfelt appreciation after my qualifying exam was truly an inspiration.

I thank NUS for providing me the scholarship during my doctoral studies. I also appreciate all the administrative help provided by the ECE department staff. I wish to acknowledge the

invaluable help provided by the staff of CICFAR (Centre for Integrated Circuit Failure Analysis & Reliability), especially Mrs. Ho Chiow Mooi, Mr. Koo Chee Keong and Mrs. Linn Linn throughout my research studies. Mrs. Ho was always beside me during the hard moments and motivated me to go forward. Her generous care and professional support has always been a genuine encouragement.

Along the way, I got incredible opportunity to collaborate with various research groups which is the true reason for success of many experiments shown in this thesis. I've been fortunate to collaborate with Dr. Shen ZeXiang's research group at NTU (Nanyang Technological University) and I sincerely thank him for providing the Raman facility. Specifically I would like to thank Dr. Sinu Mathew for his advice throughout the experimental studies and his in depth involvement while drafting journal papers. Assistance provided by Dr. Sinu Mathew and Mr. Zhan Da during Raman measurements is greatly appreciated. I would like to acknowledge Dr. T. K. Chan for his support during the irradiation study. I like to thank Mr. Mahdi Jamali for all the fruitful technical discussions. I wish to acknowledge the help provided by Mr. Jae Sung during the etching of the samples. I would like to extend my warm thanks to Mr. Vignesh Viswanathan for introducing me to Dr. Daniel Pickard and for giving me an excellent support during the patterning of devices. I also would like to acknowledge him for his constant motivation. I owe my sincere thanks to Dr. Krishna Agarwal for giving me a good exposure to matlab programming.

During the very early days of my PhD studies I was fortunate to have been associated with Dr. Khine Lynn and Mr. Niu Tian Fang who made me feel most comfortable in the VLSI (Very Large Scale Integrated Circuit) lab where I first began my research studies. I would always be grateful to Dr. Wong Chee Leong for all the technical advice he has given me. The one thing which I always admire about him is the way he keeps things organized and I have learnt this very good aspect from him though I'm still tad bit disorganized.

I greatly value the friendship I share with my fellow postgraduate students, especially Prakash Pitchappa, Ramprakash Kathiresan, Rangarajan Jagadeesan, Hari Krishnan, Ponnivalavan Babu, Alagu Narayanan, Mohan Gunasekaran, Aravind Raghavendra, Murthy Krupati and Karthik. Their support and care helped me stay focussed in my studies when I had setbacks. I will always cherish the great moments I had with them discussing about research, life and everything else in between.

It gives me great pleasure to thank my sister Mrs. Solai Cauvery for providing me shelter when I first landed in Singapore. Since then she has been my confidant and a great mentor. The time I have spent with her and her family will always be a lasting part of my fond memories.

I thank my parents-in-law Mr. SV. K. Radhakrishnan and Mrs. Lakshmi Radhakrishnan, for supporting me in my decisions. I would like to convey my appreciation to my father-in-law for his constant concern and advice when I had examinations and research difficulties.

My elder sister Alagammai Palaniappan and my younger brother Lakshman Annamalai are truly my role models. I admire their good work ethic and the hard work they put in, in every task they do. At this most precious moment, I would like to say that I deeply love them both in spite of all the small clashes we have had since childhood.

I want to thank my wonderful parents Dr. Annamalai Lakshmanan and Mrs. Kothai Annamalai for their unconditional love and support they have given me since my childhood. Their love for the family and each other without any expectations continues to inspire me. My mother’s gold medal achievement during her under graduation and my father’s hard efforts as a medical practitioner has always been my educational inspiration. During these years they have stood beside me through thick and thin and have helped me reach great heights.

I really fall short of words to express my genuine appreciation to my loved ones, especially my husband Sevugan K Radhakrishnan and my cute little princess Neha Sevugan. I would like to thank them both for understanding my mood swings and for helping me in every possible aspect.

I dedicate this important accomplishment of my life to my wonderful parents, my loving husband and my sweet little daughter.

Meenakshi Annamalai
NUS, Singapore
21st January 2013

TABLE OF CONTENTS

SUMMARY

This study examines the mechanical properties of novel two-dimensional materials with an extensive emphasis on graphene and its potential applications. Nanomechanical graphene (monolayer and multilayer) devices were fabricated by mechanical exfoliation of graphite over trenches in SiO_2. Mechanical properties and the effects of anchor geometry on the mechanical behaviour have been probed using atomic force microscopy (AFM). An analytical framework and finite element modelling has been proposed to support the experimental findings. The adopted test methods can be extended to characterize other nanomaterials and to elucidate this, results obtained from molybdenum disulfide (MoS_2) have been presented. The first observation of surface morphology variation in few-layer graphene using AFM nanoindentation and thermal engineering of the ripples has been described. Graphene irradiation using helium ions and its effects on the mechanical properties has been studied for the very first time. The devices have also been patterned to obtain structures with sub -10 nm feature sizes using helium ion microscope.

LIST OF TABLES

LIST OF FIGURES

LIST OF SYMBOLS

υ_f	Fermi velocity
$\hat{\sigma}$	Pauli matrix
k	Quasi particle momentum
e	Strain
T	Stress
S	Elastic compliance
C	Modulus of elasticity
E	Young's modulus
G	Shear modulus
υ	Poisson's ratio
f_{shear}	Shear frequency
f_{bending}	Bending frequency
f_0	Resonance frequency
ρ	Density of graphite
l	Length
h	Thickness
a	Radius
A	Area
m	Mass
F	Force
k_c	Cantilever spring constant
x	Cantilever deflection
P	Uniformly distributed load
D	Flexural rigidity, Deflection sensitivity of cantilever
d_0	Maximum displacement

r	Radial coordinate
U	Strain energy
ε_0	Permittivity of free space
ε_r	Relative permittivity
V_S	Applied voltage
g	Initial gap
t_{air}	Air gap
ε_{ox}	Relative permittivity of SiO_2
t_{ox}	Residual oxide thickness
k_1	Linear spring constant
k_3	Nonlinear spring constant
d_{crit}	Critical deflection amplitude
$d_{cantilever}$	Cantilever deflection
δ	Deflection of graphene
Z_{piezo}	Piezo scanner displacement
T	Pre-tension
φ	Damage cross-section

CHAPTER 1 : INTRODUCTION

"Graphene is a splendid material, and its rapid rise to fame shows how quickly science can respond to new discoveries. Within a year or so of Andre Geim's and Konstantin Novoselov's first work with graphene, it became the subject of dozens of sessions at large science meetings. Many scientists, seeing a rich research opportunity, stopped what they were doing and turned to graphene."

–Dr. H. Frederick Dylla (Executive Director of American Institute of Physics) [1]

1.1 Motivation and Background

The steady miniaturization of electromechanical devices brings about the promise of revolutionizing electronic systems in tasks as diverse as information processing, molecular manipulation and sensing. Nanoelectromechanical Systems (NEMS) is one of the most active areas in contemporary electromechanical systems research. Due to advances in technology and scaling of devices, MEMS (Microelectromechanical Systems) based devices has reached nanoscale dimensions. Silicon has, so far, been the staple building block for state of the art MEMS. Its high Young's modulus (~165 GPa) and good electronic properties make it ideal as a structural material for devices such as resonators, switches and valves [2]–[6]. However, as devices continue to scale down in dimensions and scale up in operating frequencies, it may soon become necessary to explore novel materials to meet future performance demands.

In recent times, graphene has garnered much interest due to its unique characteristics. Graphene is a newly isolated material whose structure consists of a single atomic sheet of sp^2-bonded carbon [7]. The promise of graphene as a material for next generation NEMS lies in its extraordinary mechanical and electronic properties. Despite its single-layer configuration, graphene maintains an exceptionally high Young's modulus of ~1 TPa [8][9] which is an order of magnitude larger than silicon. Hence, devices of the same dimension made from graphene have significantly larger stiffness and can potentially operate at frequencies 2 – 3 times higher than that of similar silicon-based structures. In addition, the

exceptional breaking strength of graphene ~130 GPa [8] also allows for very thin, large area sheets to be suspended without the concern of mechanical fracture, a critical requirement since MEMS devices typically involve free-standing structures that exhibit motion upon actuation. Being robust, stiff and stable, graphene has exciting potential as a structural material for future NEMS. These devices also open up the possibility of integrated systems featuring graphene sensors and graphene-based electronics.

1.2 Objectives

The research interests during this study are in close conjunction with the needs of intriguing novel materials. The main purpose of this research study is to explore the mechanical properties and potential applications of a newly isolated two-dimensional (2D) material, graphene.

The first objective of this work is to extract the mechanical properties of the fabricated devices using AFM. Two methods of sensing mechanical deformation have been proposed. The first method involves electrostatic actuation of the devices and measuring the deflection using AFM imaging. The second technique involves the use of an AFM as a nanoindenter to sense the mechanical deformation of the structures by obtaining force-deflection curves. By adopting these characterization techniques, the mechanical properties of the devices which include linear and nonlinear spring constants, Young's modulus, 2D elastic modulus and pre-tension of the devices can be extracted. This work also aims to develop analytical modelling and finite element simulations (FEM) to support the experimental findings.

The second objective is to modify the surface morphology of graphene which would enhance its properties for various applications. First experiments of inducing ripples in few-layer suspended graphene using AFM nanoindentation and engineering the surface corrugations

through temperature treatment has been proposed. This capability would particularly be useful for making flexible nanoscale devices and electronics based on strain engineering.

The third objective is to create defects in suspended graphene devices (monolayer and few-layer) using helium ion irradiation and to explore the mechanical properties of the defective structures for the very first time. This study also aims to show the capability of reconstruction of graphene lattice after irradiation and its ability to remain suspended without any detrimental effects in its mechanical properties. The stability of graphene and its high tolerance to irradiation imposed damages indicates the ruggedness of the material and its promising use in the future graphene based NEMS under strident conditions.

The fourth objective of this work is to use the cutting edge tool to pattern the graphene devices. Nanopatterning of the structures using helium ion microscope (HIM) has been employed to show the potential capability of obtaining sub -10 nm feature sizes. Such efforts clearly demonstrate the use of the emerging technology to obtain nanoscale devices with enhanced design and performance variations.

The graphene samples used in this study have been fabricated through micromechanical exfoliation of graphite and subsequent transfer to patterned substrates. The working device structures can be consistently fabricated through the adopted technique.

1.3 Overview

Fabrication and characterization of the recently isolated 2D material graphene has been documented in this thesis. Chapter 2 reviews the uniqueness of carbon allotropes and in particular the structure of graphene and its properties. This chapter also describes the various fabrication methodologies to extract graphene.

The various fabrication and characterization techniques adopted in this study are detailed in Chapter 3. The extraction of the mechanical properties of the fabricated suspended graphene drum structures using AFM is documented in Chapter 4. Analytical modelling and FEM simulations have also been detailed to support the experimental findings. The resonance characteristics of the structures obtained using plate theory and FEM simulations have also been described. This chapter also documents the potential applications of nanomechanical graphene devices.

Chapter 5 details the mechanical properties of monolayer and few-layer graphene devices obtained from AFM nanoindentation. This chapter also describes the continuum mechanics approach to extract the mechanical properties (Young's modulus and pre-tension) of the devices from the obtained experimental force-deflection curves. The effect of anchor geometry on the mechanical properties of the devices has also been discussed. This technique has been extended to study the other newly isolated 2D material, MoS_2 and the results obtained are also presented in this chapter.

First observation of introducing ripples in few-layer graphene through AFM nanoindentation is detailed in Chapter 6. The capability of engineering the extrinsic ripples through thermal treatment is also described.

Chapter 7 introduces the technique to irradiate graphene through helium ions and Raman spectroscopy study of the defect formation in the structures after irradiation. The first experimental measurements on irradiated graphene to extract its mechanical properties have also been described in detail.

The capability of using the cutting edge tool to pattern graphene has been documented in Chapter 8. The technique to pattern the fabricated devices (monolayer and multilayer) using helium ion microscope (HIM) has been demonstrated.

Chapter 9 concludes this study and indicates the possible future works.

CHAPTER 2 : REVIEW OF GRAPHENE AND ITS PROPERTIES

"Carbon has this genius of making a chemically stable two-dimensional, one-atom-thick membrane in a three-dimensional world. And that, I believe, is going to be very important in the future of chemistry and technology in general."

–Dr. Richard Errett Smalley (Nobel Lecture 1996) [10]

2.1 Carbon Wonderland: A Walk from Carbon to Graphene

Carbon is one of the most fascinating elements in group 14 (group IV) on the periodic table due to its versatility to form numerous number of compounds. Carbon can contribute to different forms of bonding which in turn span a large range of unique properties. The hybridization of atomic orbitals (sp^3, sp^2 and sp^1) in carbon enables the carbon atoms to form several types of valence bonds which in turn contribute to various different structures [11]. The three-dimensional (3D) crystalline pure forms of carbon, namely, graphite and diamond have been known to exist since ancient times. After the discovery of zero-dimensional (0D) bucky balls (spherical fullerenes) in 1985 by Richard Erret Smalley along with his co-workers [12] and one-dimensional carbon nanotubes (CNTs) (1D) in 1991 by Sumio Iijima [13], the allotropes of carbon have received tremendous attention from the research world. The existence of 2D crystalline form of carbon which is now termed as "graphene" and its existence was a theoretical debate until its experimental discovery in 2004 by Andre Geim et al. from Manchester University [14]. According to Landau and Peierls, it was earlier believed that 2D crystals are thermodynamically unstable and thus could not exist in nature [15][16]. Later in 1968, Mermin-Wagner theorem was further developed to validate this hypothesis which states that due to divergent contributions from thermal fluctuations, the long-range crystalline order would be destroyed in 2D crystals at any finite temperature and thus would result in melting of a 2D lattice [17]. The very recent observation of corrugations along the third dimension (ripples/wrinkles) in graphene provides justifications for its structural stability [18][19]. This 2D form of carbon is the mother of all graphitic systems which

include 0D fullerenes, 1D nanotubes and 3D graphite. Graphene can be stacked up to form graphite, rolled to form CNTs and wrapped into a sphere to form C60 (Buckminster fullerene). The crystal structure of the various sp^2 hybridized allotropes of carbon is shown in Figure 2-1, indicating that graphene can be used as a primary building block to create graphitic materials of all other dimensionalities [7].

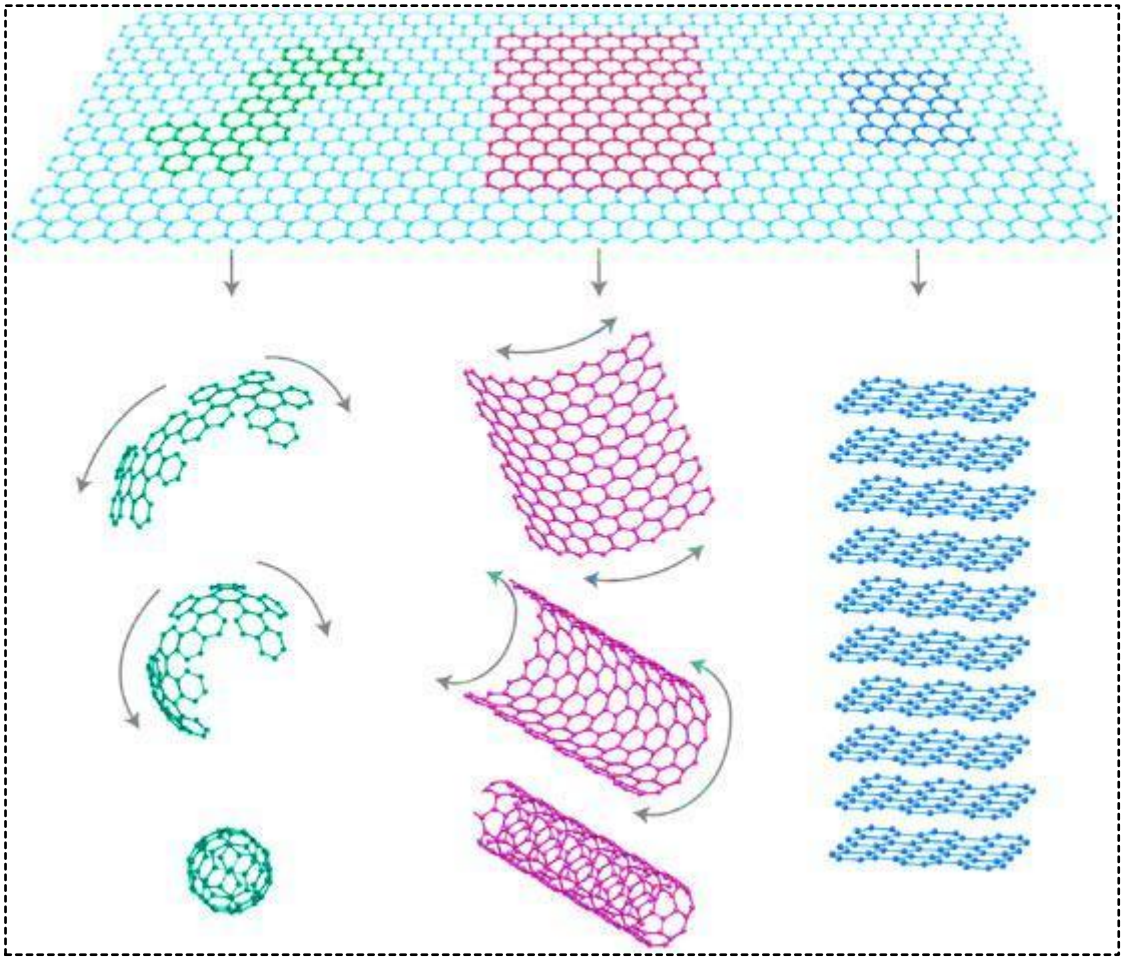

Figure 2-1: The sp^2 hybridized allotropes of carbon formed using a single atomic layer of graphene. (Left to right) 0D buckyball, 1D nanotube and 3D graphite (adapted from Ref. [7]).

2.2 Structure of Graphene

Graphene is one atom thick and consists of sp^2-bonded carbon atoms [7]. It condenses to form a honeycomb lattice due to its sp^2 hybridization. The interaction of 2s orbital with $2p_x$ and $2p_y$ orbitals causes the formation of sp^2 hybridized orbitals. It is a 2D hexagonal structure, with each atom forming three bonds (σ bonds) with each of its nearest neighbour's

through the three valence electrons localized along the plane at an angle of 120° [7]. These covalent carbon-carbon bonds in graphene are responsible for the strong mechanical properties. Whereas the electronic properties are strongly influenced by the π-bonds which are formed as the electron cloud for $2p_z$ orbital is spread normal to the plane. The carbon-carbon bond length in graphene is ~0.142 nm [20]. The graphene hexagon has six ring carbon atoms which have six free bonds which include four single bonds and two resonance bonds. These carbon atoms covalently bind to six other carbon atoms as shown in Figure 2-2. Monolayer graphene sheets stack to form graphite with an interplanar spacing of ~0.335 nm [21] and are held together by van der Waals (VdW) forces of attraction.

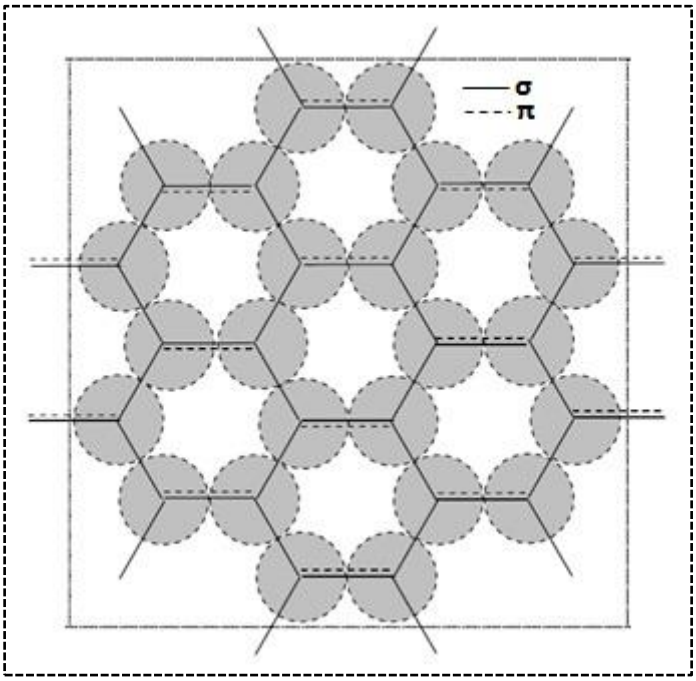

Figure 2-2: Seven hexagons made using 24 carbon atoms in a single graphene sheet occupying an area of ~0.8 nm^2 (adapted from Ref. [22]).

The hexagonal lattice structure of graphene was confirmed through transmission electron microscopy (TEM) studies. It was also found that suspended graphene exhibited ripples on the surface with an amplitude of about 1 nm. These intrinsic ripples in graphene provide justifications for its structural stability [19].

2.3 Graphene Fabrication Methodologies

2.3.1 Graphene Synthesis from Graphene Oxide and Graphene Intercalation Compounds

Fabrication of graphene from graphite oxide and graphene intercalation compounds (GIC) was the very first developed methods for graphene synthesis. Insertion of an acid or alkali metal in between carbon lamellae which is termed as "intercalation" and exfoliation of graphite with nitric and sulphuric acids was reported by Schafhaeutl et al. [23]. But this method yielded graphite with a widened interlayer spacing which resulted in electronic decoupling between graphene layers. Brodie showed that graphitic oxide (GO) can be obtained by treating pure graphite with nitric acid or potassium chlorate [24]. Boehm et al. reported that lamellae of carbon can be obtained by rapid heating of graphite oxide or by reduction of graphitic oxide in an alkaline suspension [25]. But, the quality of graphene produced by this method is low. Further advancements to this technique was developed and it was shown that reduction of graphite oxide by focussed solar radiation [26] or by direct laser reduction of graphite oxide film coated DVD disc will also result in thin graphene films [27].

2.3.2 Micromechanical Exfoliation of Bulk Graphite

In this method, an adhesive tape is used to separate graphite crystals in order to obtain very thin graphene flakes. After obtaining an optically transparent flake, the tape is dissolved in acetone and then transferred to a silicon wafer. This technique is now modified and has been made simple and reliable by the elimination of letting graphene float in a liquid. The modified method adopted by Andre Geim et al. is now termed as "scotch tape" method [14]. In this technique, graphite flakes are cleaved several times using a scotch tape until thin layers of graphene sheets are obtained. The graphene sheets are then transferred to a substrate by pressing down the tape and gently removing it away as indicated in Figure 2-3. The substrate which is usually used in this method SiO_2 (~300 nm) on silicon as it gives good

optical interference which makes graphene visible under an optical microscope [28]. The only disadvantage of this method is that fair amount of time and luck is needed to obtain suspended/supported structures and the level of difficulty increases when the graphene flake has to be deposited at a specific location on a substrate. However, this method is widely being used to fabricate nanomechanical graphene devices as it produces good quality and defect free graphene sheets.

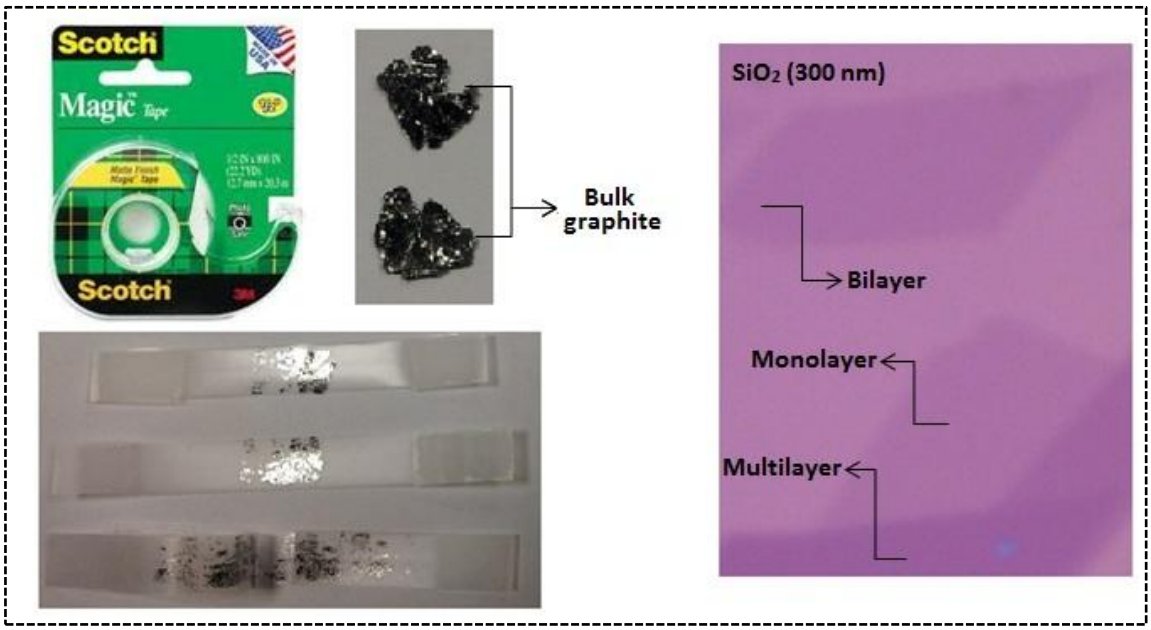

Figure 2-3: Micromechanical exfoliation of bulk graphite (left) and graphene transferred onto a SiO_2 (300 nm)/Si substrate through scotch tape transfer (right).

2.3.3 Chemical Vapour Deposition

In chemical vapour deposition (CVD) method, a metal substrate like copper is annealed in a furnace to about 1000 °C under low vacuum and in the presence of methane and hydrogen gases [29]. A catalytic reaction between methane and the metal substrate takes place, causing the deposition of carbon atoms from methane onto the surface of the metal. The furnace is then quickly cooled down to obtain contiguous graphene layer and to avoid the aggregation of carbon layers to form bulk graphite [29]. Apart from copper, nickel and cobalt are also used as metal substrates. Direct synthesis of graphene on nickel by this method is shown in

Figure: 2-4(a) [30]. Graphene obtained through this technique can be transferred to any arbitrary substrate by spin coating a polymer such as polydimethysiloxane (PDMS) or polymethyl methacrylate (PMMA) as a support and then the metal can be removed using an appropriate etchant. The supported graphene on a polymer can now be positioned on top of a desired substrate and the polymer can be dissolved using a solvent as shown in Figure: 2-4(b) [29]. The experimental conditions and the metal used play very important role to obtain graphene with less impurities. For instance, nickel and cobalt absorb more carbon atom than copper which leads to the formation of graphite crystal on the metal surface instead of a monolayer of graphene. To avoid this either copper or thin nickel film (~300 nm) coated on silicon substrate is used [30]. The presence of more hydrogen and methane gas enhances the reaction in the former and increases the number of carbon atoms deposited in the latter. Additionally, the annealing temperature and the purity of the substrate used also greatly influence the production of graphene [31]. Apart from these difficulties, due to the difference in thermal expansion coefficient (TEC) of graphene and the metal substrate used, CVD graphene is found to have wrinkles. Plasma enhanced chemical vapour deposition (PECVD) is also used to fabricate graphene and the method involves an additional radio frequency (RF) alternating current (AC) to be passed through the substrate which enhances the carbon deposition onto the substrate by ionizing the gases in the chamber [32].

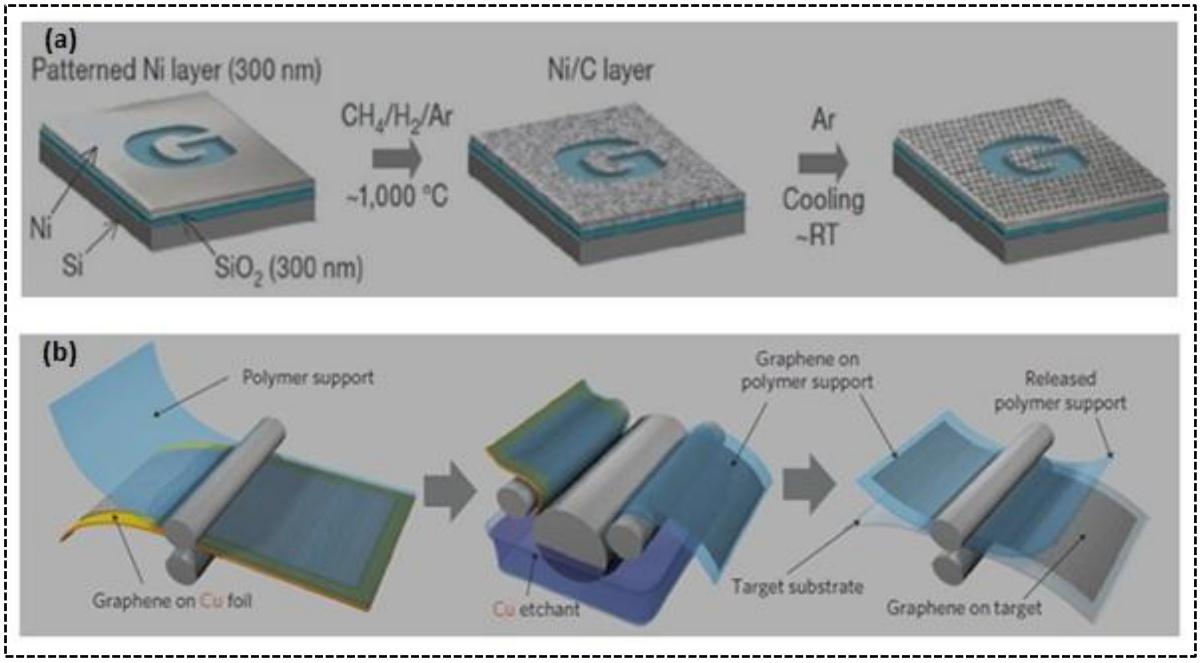

Figure: 2-4: (a) Direct synthesis of large area graphene sheets on thin nickel layers using CVD (adapted from Ref. [30]) (b) Roll-to-roll production of graphene films (30 inch) grown on copper foils and transferred on a target substrate (adapted from Ref. [29]).

2.3.4 Epitaxial Growth of Graphene

Epitaxial graphene can be grown from silicon carbide (SiC) crystal by heating it at around 1500 °C. In the event of heating, sublimation of silicon occurs thus leaving a layer of carbon on the surface [33][34]. Few-layer graphene on SiC fabricated by this method is shown in Figure 2-5(a). Graphitization of SiC is greatly influenced by the heating parameters and controlling the grain sizes and number of graphene layers is difficult. Another way of producing epitaxial graphene can be achieved through molecular beam epitaxy (see Figure 2-5(b)). In this method, a graphite filament is heated (1000–1100 °C) in an ultra-high vacuum chamber which leads to the sublimation of carbon atoms from graphite which in turn generates a molecular beam of carbon atoms in vacuum. This molecular beam does not interact and thus travels through free space until it hits a metal substrate like iridium to form a graphene layer [35][36]. The main disadvantage of this technique is the requirement of ultra high vacuum which makes the process very difficult.

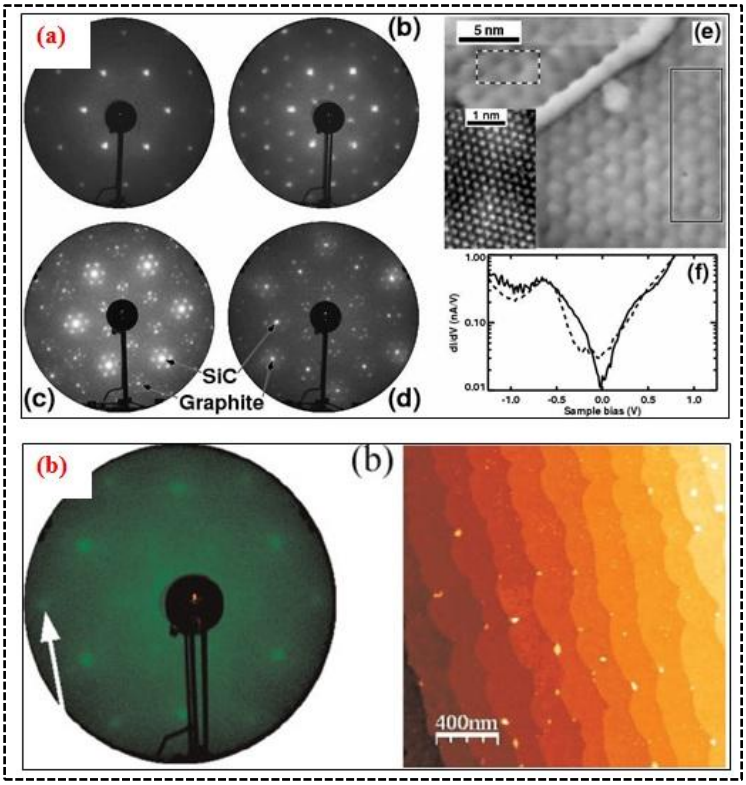

Figure 2-5: (a) Low energy electron diffraction (LEED) patterns of few layer graphene on SiC(0001) (adapted from Ref. [34]) (b) LEED pattern and AFM image showing 1.5 ML (Monolayer) graphene epitaxially grown on SiC (adapted from Ref. [35]).

2.3.5 Chemical Synthesis

This technique incorporates the dispersion of graphite from a solution as indicated in Figure 2-6. Graphite flakes are sonicated in a solution and the non-exfoliated graphite is separated by centrifugation from graphene [37][38]. Long sonication time needed to disperse graphite and obtaining graphene layers without breaking are the disadvantages of this technique.

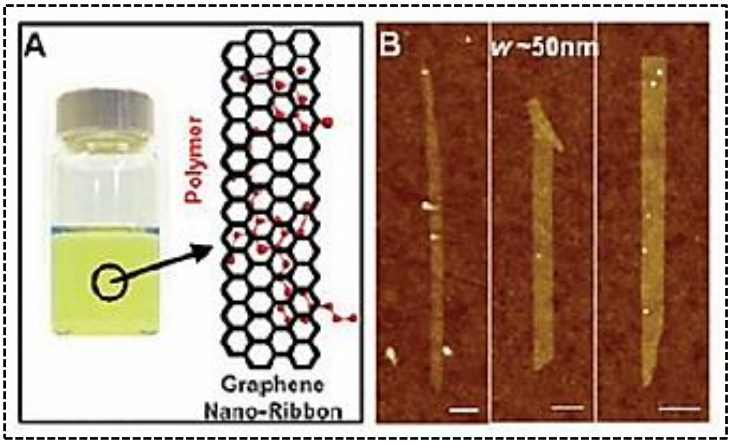

Figure 2-6: Photograph of a polymer PmPV/DCE with GNRs stably suspended in the solution and ultra narrow ribbons 1.5, 1.4, 1.5 nm respectively (adapted from Ref. [37]).

2.3.6 Stamping Method

In this fabrication process, micropillars/protrusions are created and coated with glue which is then used to exfoliate graphene from highly oriented pyrolytic graphite crystals (HOPG) [39][40]. The illustration of the stamping process is shown in Figure 2-7.

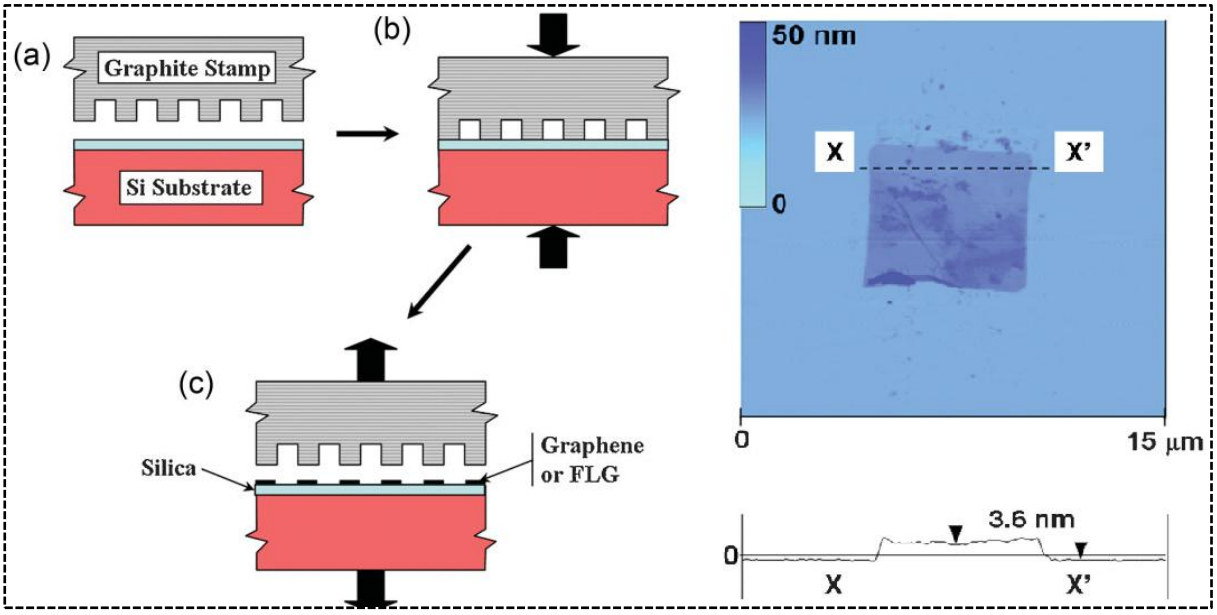

Figure 2-7: Schematic illustration of the stamping method (left) and AFM image showing a stamped square of graphene along with the profile across a location (right) (adapted from Ref. [39]).

2.3.7 Electrostatic Force Assisted Exfoliation

Graphene of desired thickness is obtained by applying a bias voltage (see Figure 2-8) and since graphene sheets are weakly bound in graphite, they can be easily removed by applying

an electrostatic force [41][42]. Bias voltage determines the number of graphene layers to be separated and deposited on the target substrate.

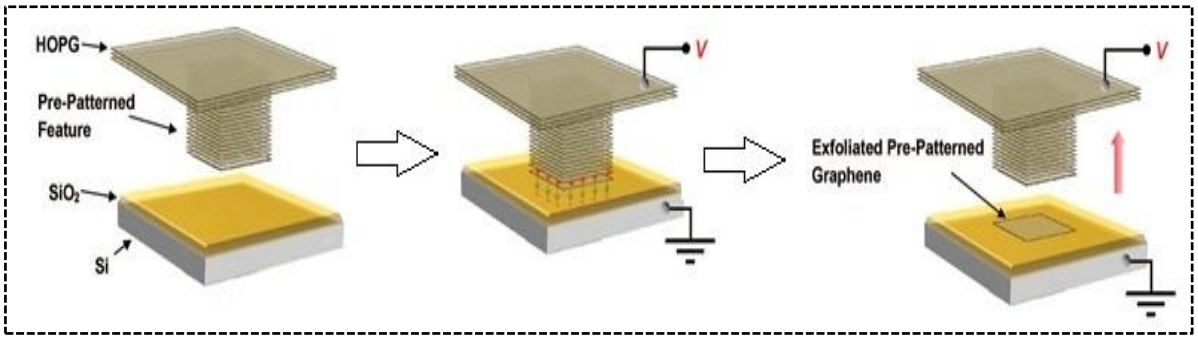

Figure 2-8: Schematic illustration of electrostatic force assisted exfoliation of pre-patterned graphene (adapted from Ref. [41]).

2.3.8 Other Methods

Graphene can also be fabricated through various other techniques and to name a few, unzipping graphene from carbon nanotubes (CNTs) as shown in Figure 2-9 [43][44], pyrolysis of sodium ethoxide [45] and through exothermic combustion reaction of carbon dioxide [46]. However, due to the extreme high quality of exfoliated graphene prepared by micromechanical exfoliation of Kish graphite and the ability to consistently produce suspended graphene sheets, scotch tape method is widely being used. In this study, this method has been adopted due to the above mentioned reasons.

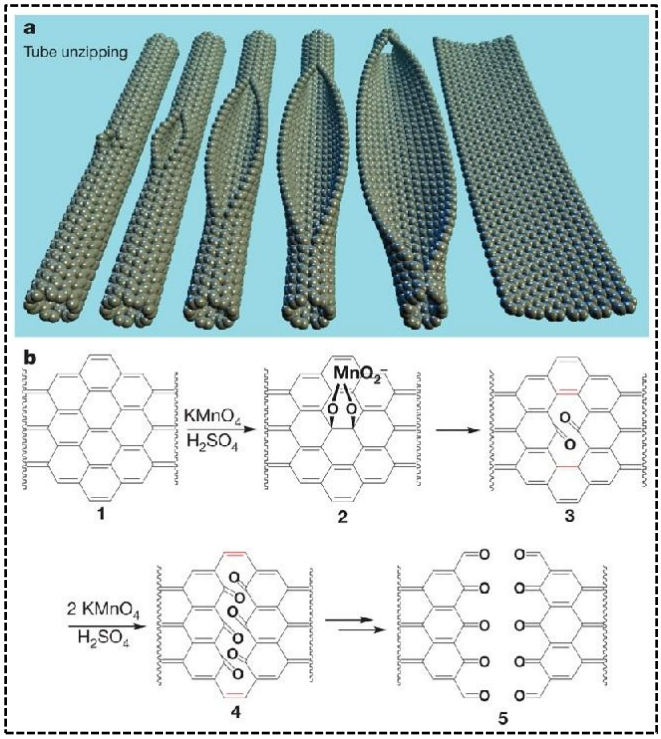

Figure 2-9: Unzipping graphene from CNT through an oxidation process (adapted from Ref. [43]).

2.4 Electronic Properties

The conduction and valence bands of graphene overlap and hence it is a zero-gap semiconductor or a semi-metal. As discussed in Section 2.1, the π bonds in graphene are mainly responsible for its unusual electronic properties and the electronic band structure of graphene is shown in Figure 2-10. Wallace et al. in early 1947 reported that electron momentum *k* is linearly related for low energies near the six edges (Dirac points) of the 2D Brillouin zone which leads to the behaviour of electrons like massless Dirac fermions/Graphinos [47]. The low energy electronic state follows a linear relationship instead of a parabolic dispersion relation and can be described by Dirac equation for fermions [48].

$$\hat{H} = \hbar v_f \begin{pmatrix} 0 & k_x - ik_y \\ k + ik_y & 0 \end{pmatrix} = \hbar v_f \hat{\sigma}.k \qquad (2.1)$$

where v_f is the Fermi velocity, $\hat{\sigma}$ is the Pauli matrix and *k* is the quasi particle momentum.

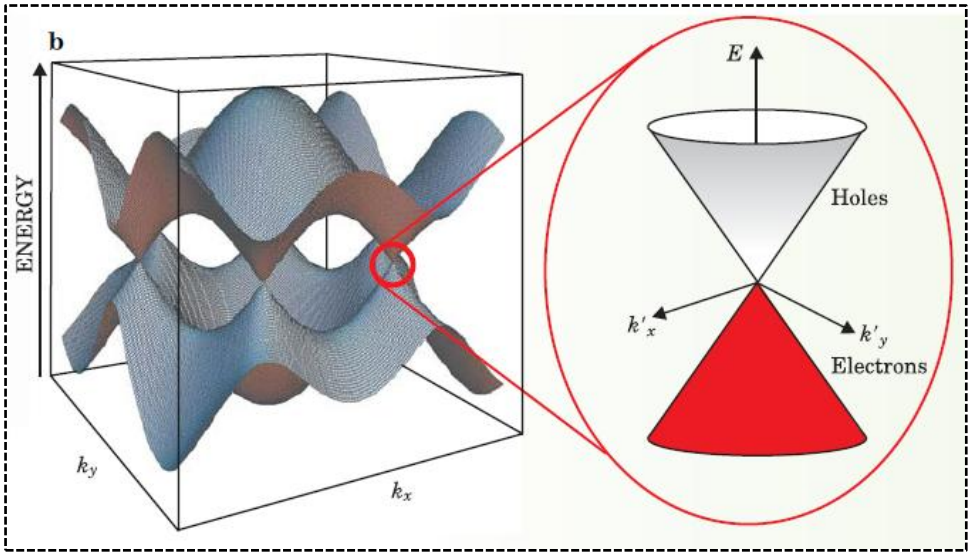

Figure 2-10: 3D representation of a single layer graphene sheet showing that the overlap of the conduction and valence band shrinks to a single point (adapted from Ref. [49]).

Transport measurements on mechanically exfoliated graphene indicate that it possesses remarkably high electron mobility independent of the carrier type under ambient conditions with values exceeding 2×10^5 $cm^2V^{-1}s^{-1}$ [50]. The corresponding resistivity of graphene was found to be 10^{-6} Ωcm (lower than the resistivity of silver!!). It is also observed that, even when the charge carrier concentrations turn nearly zero, minimal conductivity is observed in both monolayer [51] and bilayer graphene [52]. The room temperature thermal conductivity of graphene was measured to be $\sim5\times10^{-3}$ $Wm^{-1}K^{-1}$ [53]. Unlike other metals, quantum Hall effect (QHE) is observed even at room temperature in monolayer graphene [54]. Whereas in a bilayer graphene, a normal QHE can be observed after doping it to break the symmetry between the two graphene monolayers to obtain an energy band gap [52]. Many of these unique characteristics make graphene suitable for various applications in nanotechnology such as integrated circuits [55], transistors [14] and transparent conducting electrodes [56], to name a few.

2.5 Mechanical Properties

The covalent C-C bonds in graphene are the strongest bonds which gives rise to exceptional mechanical properties. In order to understand its mechanical properties it is worthwhile to recapitulate the mechanical properties of graphite. A detailed description of physics of graphite can be found in B.T Kelly's book which was published in 1981 [57]. The main contributions of this book on mechanical properties have been outlined in this section.

Elastic constant of a material is defined as the ratio of stress to strain. The equations which describe the relation of stress and strain for a hexagonal lattice structure like graphite are indicated below.

$$\begin{aligned} e_{xx} &= S_{11}T_{xx} + S_{12}T_{yy} + S_{13}T_{zz} \\ e_{yy} &= S_{12}T_{xx} + S_{11}T_{yy} + S_{13}T_{zz} \\ e_{zz} &= S_{13}T_{xx} + S_{13}T_{yy} + S_{33}T_{zz} \\ e_{zx} &= S_{44}T_{zx} \\ \mathrm{e}_{zy} &= S_{44}T_{zy} \\ e_{xy} &= 2(S_{11} - S_{12})T_{xy} = S_{66}T_{xy} \end{aligned} \tag{2.2}$$

where e is the strain, T is the stress and S is the elastic compliance. The above six equations can be written in their inverse form as follows.

$$\begin{aligned} T_{xx} &= C_{11}e_{xx} + C_{12}e_{yy} + C_{13}e_{zz} \\ T_{yy} &= C_{12}e_{xx} + C_{11}e_{yy} + C_{13}e_{zz} \\ T_{zz} &= C_{13}e_{xx} + C_{13}e_{yy} + C_{33}e_{zz} \\ T_{zx} &= C_{44}e_{zx} \\ T_{zy} &= C_{44}e_{zy} \\ T_{xy} &= \frac{1}{2}(C_{11} - C_{12})e_{xy} = C_{66}e_{xy} \end{aligned} \tag{2.3}$$

where C is the modulus of elasticity. The two constant C and S can be related as follows.

$$
\begin{aligned}
C_{44} &= S_{44}^{-1} \\
(C_{11} - C12) &= (S_{11} - S_{12})^{-1} \\
\frac{C_{13}}{X} &= S_{13} \\
\frac{C_{33}}{X} &= S_{11} + S_{12} \\
\frac{(C_{11} = C_{12})}{X} &= S_{33}
\end{aligned}
\tag{2.4}
$$

The Young's moduli parallel to the hexagonal and basal planes are E_c (S_{33}^{-1}) and E_a (S_{11}^{-1}) respectively. The Shear modulus parallel to the basal planes is given by $G = S_{44}^{-1} = C_{44}$.

In order to determine the elastic constant Baker and Kelly measured the resonance frequency of free-free beam cantilevers (natural graphite flakes). The length and thickness of the beam were 0.4 cm to 1 cm and 0.01 to 0.05 cm respectively. The vibrations of these flakes can either be dominated by shear or bending. The resonance frequency due to shear and bending are given below.

$$
\begin{aligned}
f_{\text{shear}} &= \frac{1}{4l}\left(\frac{\mathrm{G}}{\rho_0}\right)^{1/2} \\
f_{\text{bending}} &= \left(\frac{Et^2}{12\rho_0}\right)^{1/2} \frac{(1.875)^2}{2\pi l^2}
\end{aligned}
\tag{2.5}
$$

Where f is the resonance frequency, G (C_{44}) is the shear modulus, E (S_{11}^{-1}) is the Young's modulus, ρ_0 is the density of graphite; l and t are the length and thickness of the cantilever. Shear frequency is inversely proportional to length and bending frequency is inversely proportional to square of the length.

The vibrations in as-received graphite samples were shear dominated with G = 0.1 GPa while irradiated graphite crystals were dominated by bending with E = 0.6 TPa. The value of G obtained is much lower than expected due to dislocations. A group at Union Carbide Parma Laboratories performed a detailed study to determine the elastic shear constant value using

ultrasonic pulses, sonic resonance, and static test methods. The elastic constants found by them are tabulated below in Table 2-1.

Table 2-1: Summary of elastic constants and compliances of graphite

Elastic Moduli	Elastic Compliance
C_{11} = 1.06± 0.02 TPa	S_{11} = 0.98 ± 0.03 TPa^{-1}
C_{12} = 180 ± 10 GPa	S_{12} = -0.16 ± 0.06 TPa^{-1}
C_{13} = 15 ± 5 GPa	S_{13} = -0.33 ± 0.08 TPa^{-1}
C_{33} = 36.5 ± 1 GPa	S_{33} = 2.3 ± 0.2 TPa^{-1}
C_{44} = 0.18 to 0.35 GPa C_{12}/C_{11} = 0.17 ± 0.01	$-S_{12}/S_{11}$ = 0.16 ± 0.06 $E = 1/S_{11}$ = 1.02 ± 0.03 TPa

The C_{44} values seems to be spread out and this is due the fact that irradiated and non-irradiated samples exposed to fast neutrons with irradiated samples giving the higher value. This result is comparable to what was obtained during the resonance frequency measurements where irradiation increased C_{44} by reducing basal plane dislocations. As this value matches the value found in the specific heat data, this highest value is taken as the true value.

The experimentally measured Poisson's ratio C_{12}/C_{11} is 0.17. The Poisson's ratio along the basal plane of graphite is $-S_{12}/S_{11}$. From the expression that relates *C* and S, the Poisson's ratio υ of graphite along the basal plane is found to be 0.16 ± 0.06.

Hence, utilizing the enhanced electronic and mechanical attributes of graphene, will lead to a new class of next generation NEMS. However, systematic study of the influence of layer number on the mechanical properties of graphene is largely unexplored experimentally. Hence this study aims to extract the mechanical properties of exfoliated monolayer, few-layer and multi-layer pristine graphene and irradiated graphene structures. The effects of vacuum annealing on the mechanical properties of the device structures have also been studied. Moreover, experimental alteration of the surface morphology of graphene and engineering

the morphology through temperature treatment has been explored which enables the fabrication of flexible nanolectronic devices. The capability of patterning sub -10 nm features in suspended graphene through HIM has been demonstrated which opens up as an emerging technology to fabricate electromechanical devices with varying design and performance parameters.

CHAPTER 3 : FABRICATION AND CHARACTERIZATION METHODS

In this chapter, the fabrication and characterization techniques adopted for this study are discussed with details.

3.1 Device Fabrication Methodology

The suspended nanomechanical graphene drum structures used in the experiments were prepared by mechanical exfoliation [14][58] of Kish Graphite (NGS Naturgraphit GmbH) which consists of Bernal stacked layer of graphene sheets. The graphene sheets are held together by weak VdW forces and are separated by a distance of ~3.35 Å [39]. The fabrication steps adopted in Chapters 4 and 8 are summarized in Figure 3-1. To fabricate the trench structures that support the suspended graphene sheets, oxidized silicon die (285 nm SiO_2 thickness) was first patterned, using optical lithography, with line structures which were then metallized with gold to act as contact electrodes. Circular holes, of ~3.8 μm diameter, were defined in the oxide in between the gold lines and etched in buffered hydrofluoric acid (BHF) solution to obtain trench structures. The depth of the trenches is determined by the duration in which the patterned substrates were immersed in the BHF solution. In the fabricated substrates, the oxide is not entirely etched through to the substrate (i.e. some oxide remains at the bottom of the trenches) as this prevents unsuspended drum structures from shorting the entire graphene sheet to the underlying silicon substrate.

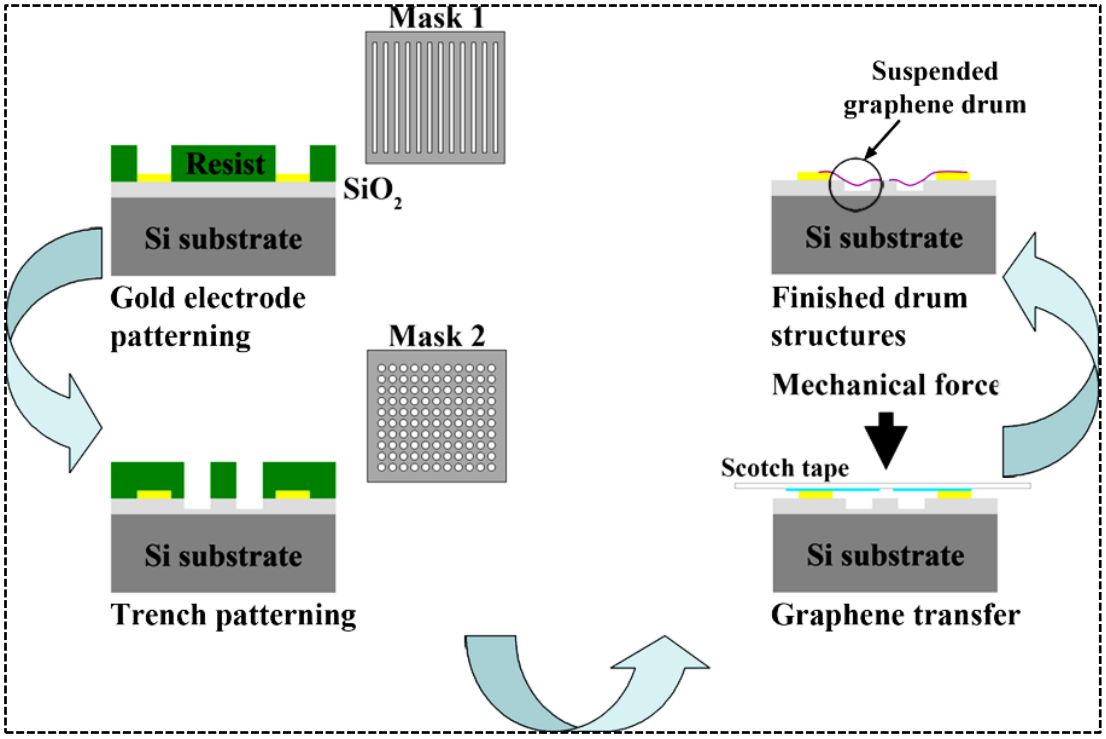

Figure 3-1: Fabrication of suspended nanomechanical graphene drum structures. The process starts with an oxidized silicon die with 285 nm oxide thickness. Two optical mask patterns were used in the process, the first to define the electrodes and the second to define the circular trenches.

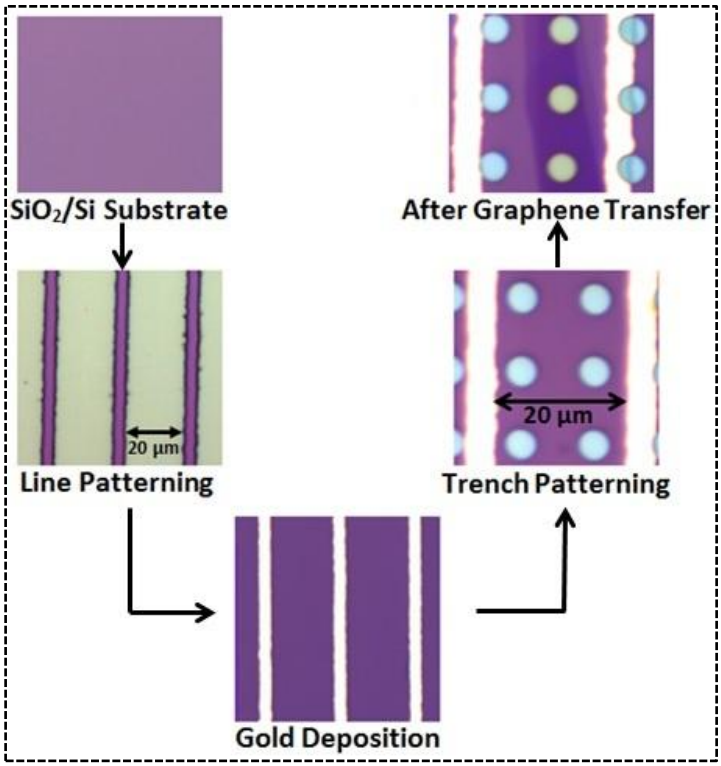

Figure 3-2: Actual optical images obtained during each fabrication step.

Graphite flake was cleaved several times using a scotch tape until thin layers of graphene sheets were obtained. The graphene flakes were then transferred to the pre-patterned substrate by pressing down the tape and gently removing it away. The resultant devices were completely covered (circular plates) or partially covered graphene structures (semi-circular plates) which are clamped along its periphery by VdW forces of attraction. Graphene sheets of up to 30 μm x 30 μm can be obtained by this process with each sheet covering 4 – 6 circular trenches, although not all the covered trenches will be suspended.

The pre-patterned substrates shown in all other chapters were prepared as follows. The trench structures to support the graphene were fabricated by a UV photo-lithography process. A SiO_2 (285 nm)/Si die was patterned using optical lithography to obtain an array of holes ~3.8 μm in diameter. The patterned substrates were subsequently etched using SF_6 plasma to define the trench structures. The fabrication sequence of making suspended graphene devices and an optical micrograph of a typical sample is shown in Figure 3-3.

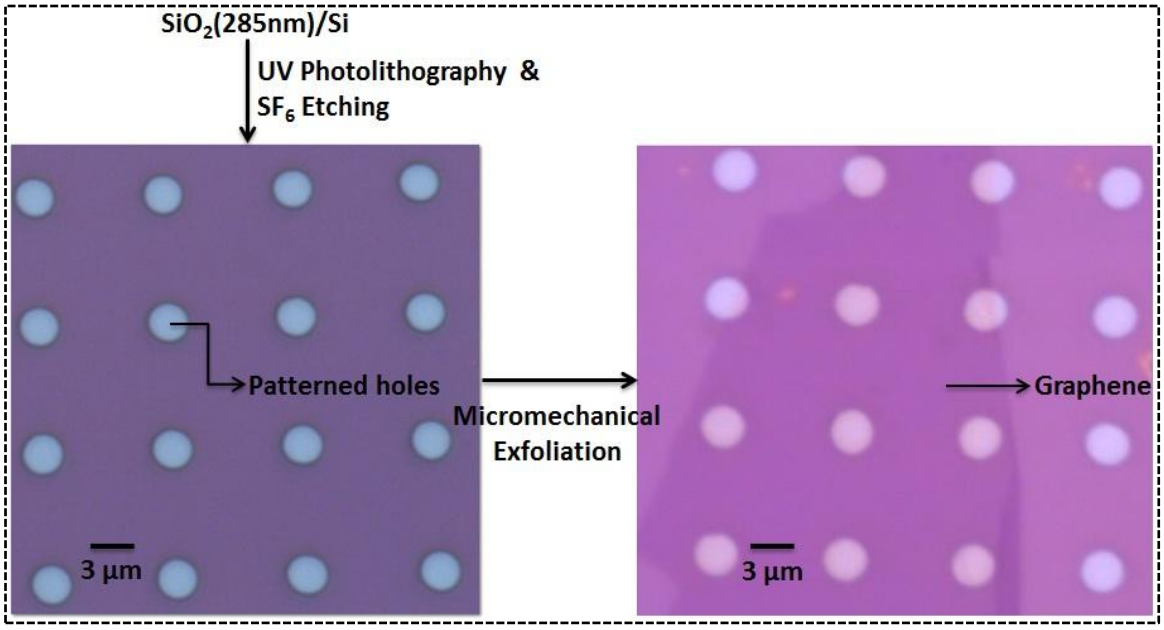

Figure 3-3: Fabrication sequence of suspended nanomechanical graphene structures.

3.2 Atomic Force Microscopy (AFM)

AFM is a high-precision type of scanning probe microscopy. It is a Nobel Prize-winning invention by Binning et al. in 1986 [59]. It has wide range of applications and is found to be extremely useful in characterizing features from nanometer to micrometer scale.

3.2.1 Principle of AFM Measurement

The AFM consists of a microcantilever (force sensor) with a sharp tip at its free end and measures the forces acting between the tip and the sample surface. This force can be described using Hooke's law,

$$F = -k_c . d_{cantilever} \tag{3.1}$$

in which F is the force, k_c is the spring constant and $d_{cantilever}$ is the cantilever deflection. These interatomic forces are in the range of 10^{-9} N. The cantilever probes are typically made from silicon nitride or silicon. The design variations allow for varied spring constants and resonance frequencies. The motion of the cantilever probe is controlled using a feedback loop and piezoelectric scanners. The deflection of the cantilever during scanning of the sample is measured using a laser spot that is reflected from the top surface of the cantilever onto a position sensitive photodetector. The resulting deflection map generates the topography of the sample. The schematic of an AFM is shown in Figure 3-4.

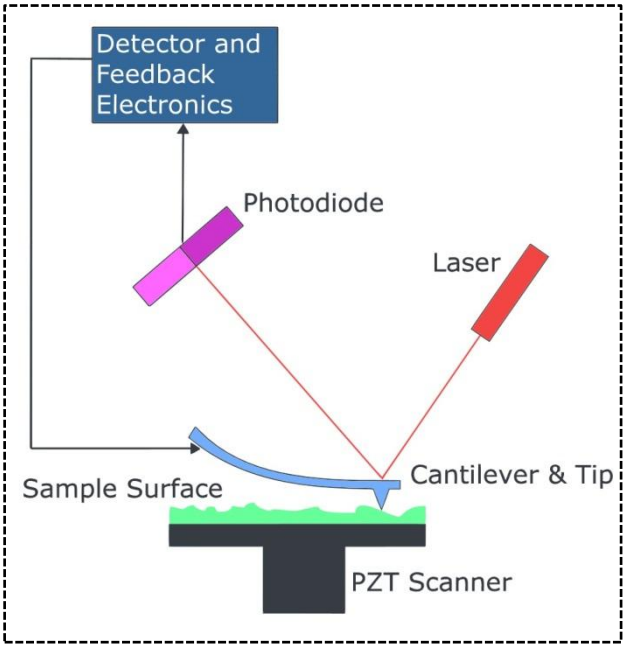

Figure 3-4: Schematic of an AFM setup (adapted from Ref. [60]).

3.2.1.1 The Primary AFM Working Modes

The primary modes of imaging include contact mode, tapping mode or intermitted contact mode and non-contact mode. In the contact mode, the force between the probe and the sample is kept constant by maintaining a constant cantilever deflection. In this mode the interatomic forces are repulsive and the probe is in close proximity to the sample (few angstroms). In the tapping mode, the cantilever is oscillated at its resonance frequency and the probe taps the sample surface while scanning. A constant tip-sample interaction is maintained by constant oscillation amplitude. This mode allows for high resolution imaging of the samples which are easily damaged when scanned in contact mode. In non-contact mode, the interatomic forces between probe and sample are attractive VdW forces. The probe does not contact the surface and the feedback loop monitors the changes in the oscillation amplitude due to attractive VdW forces and thus the surface topography is obtained.

In this thesis all the AFM images have been obtained by operating the AFM in tapping mode. Apart from imaging, AFM has been used as a nanoindenter to extract the force versus

deflection curves of the samples. The principle of material characterization by nanoindentation is described in the next sub-section.

3.2.2 AFM Nanoindentation

Nanoindentation technique provides a unique opportunity to probe the mechanical properties of devices using depth sensing instruments (DSI). The feasibility of this technique using an AFM makes it a very simple and effective technique to measure the mechanical properties of devices in the nanoscale. In this technique, an AFM probe tip is forced onto the device surface by applying loads and the corresponding probe displacement and piezo displacement is recorded by obtaining a force curve as shown in Figure 3-5. This technique opens up a possibility to apply loads as small as few nano-Newtons (nN) and measures displacement in the range of few nanometers, thus providing depth sensing in nanoscale. The representation of an AFM nanoindentation experiment on suspended graphene devices is shown in Figure 3-6.

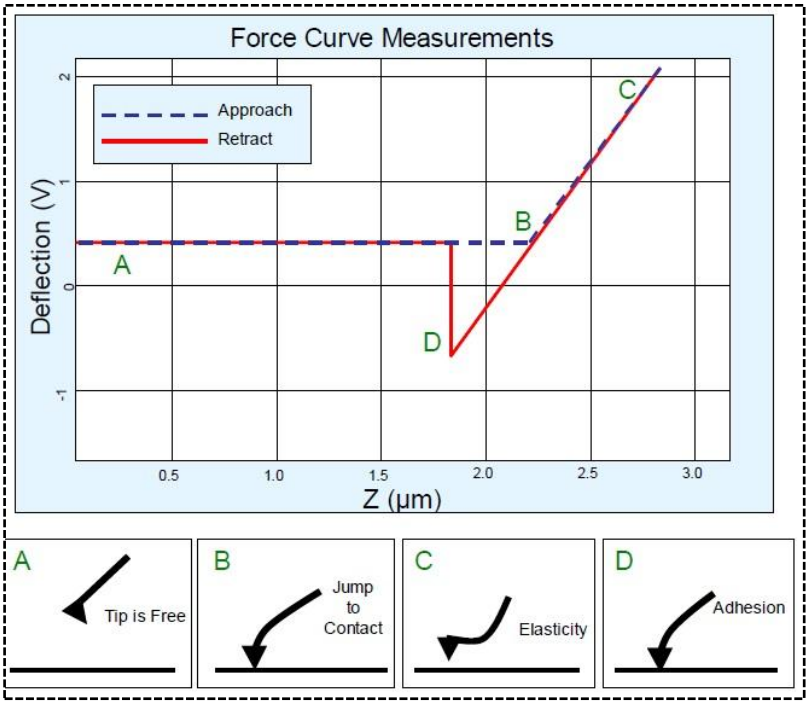

Figure 3-5: A typical force curve showing one recording cycle (adapted from Ref. [61]).

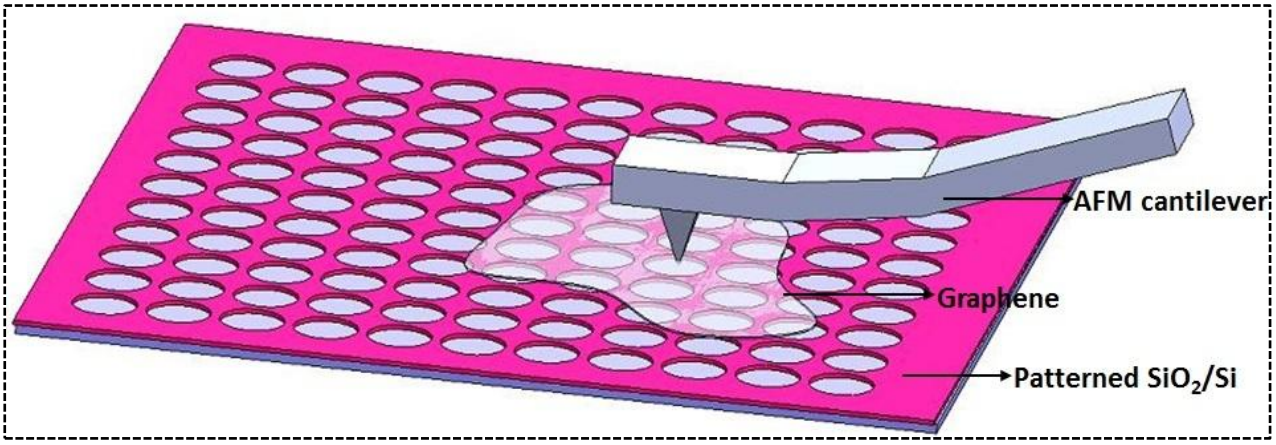

Figure 3-6: Representation of an AFM nanoindentation measurement on suspended graphene devices.

3.3 Raman Spectroscopy

Raman spectroscopy is a Nobel Prize winning invention by C. V. Raman [62]. This non-destructive spectroscopic technique involves monochromatic light scattering process, usually from visible, near infrared or near ultraviolet regime which is used for material identification and characterization. The interaction of the monochromatic incident beam on the sample causes the photons of the light to be absorbed by the sample and then reemitted. In the event of scattering process, two phenomena take place which includes Rayleigh's scattering (intense elastically scattered beam) and Raman scattering (weak inelastically scattered beam) as indicated in Figure 3-7. The scattered radiation is composed of components with frequency same as the incident radiation along with modified frequency. The light due to Raman scattering is focused onto the detector and the elastically scattered light is filtered out. Raman shift can be analysed using the captured wave numbers and subsequently the information about the vibrational, rotational and other low frequency transitions in molecules can be obtained.

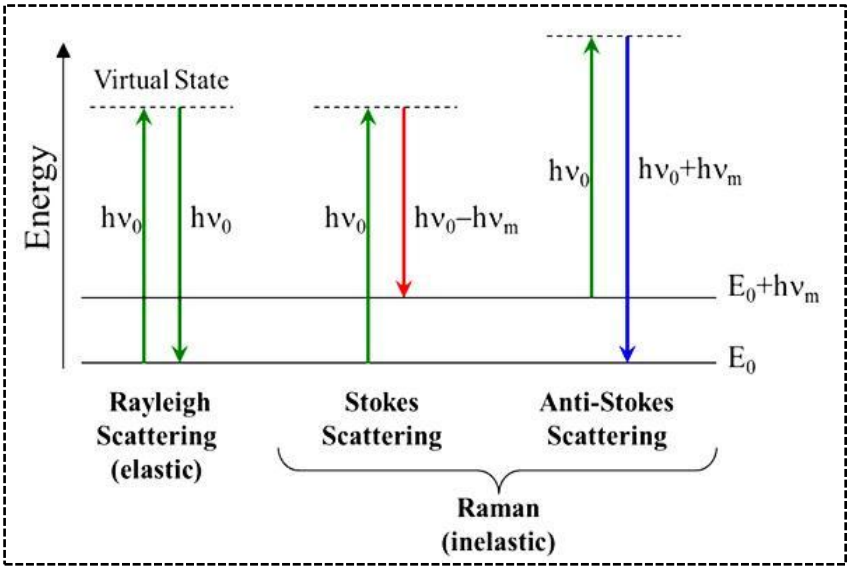

Figure 3-7: Energy transitions for Rayleigh and Raman scattering (adapted from Ref. [63]).

3.3.1 Raman Scattering of Graphene

Raman spectrum of graphene gives information about the in-plane vibration of the sp^2 hybridized carbon atoms (G band), stacking orders (2D band or G') and defects (D band) [64]. The G mode is associated with the doubly generated longitudinal optical (LO) and in-plane transverse optical (iTO) phonons at zone center [65]. The 2D mode originates from a double resonance process consisting of inter-valley inelastic-scattering events involving two D phonons (near K point) with opposite momenta [64] while the 2D' mode arises from intra-valley double resonance process involving two D' phonons near the Γ point [64][66]. The intensity of G mode increases with increase in graphene thickness whereas the 2D mode broadens and gets blue shifted as the number of graphene layers increase. Typical Raman spectra obtained from graphene is shown in Figure 3-8.

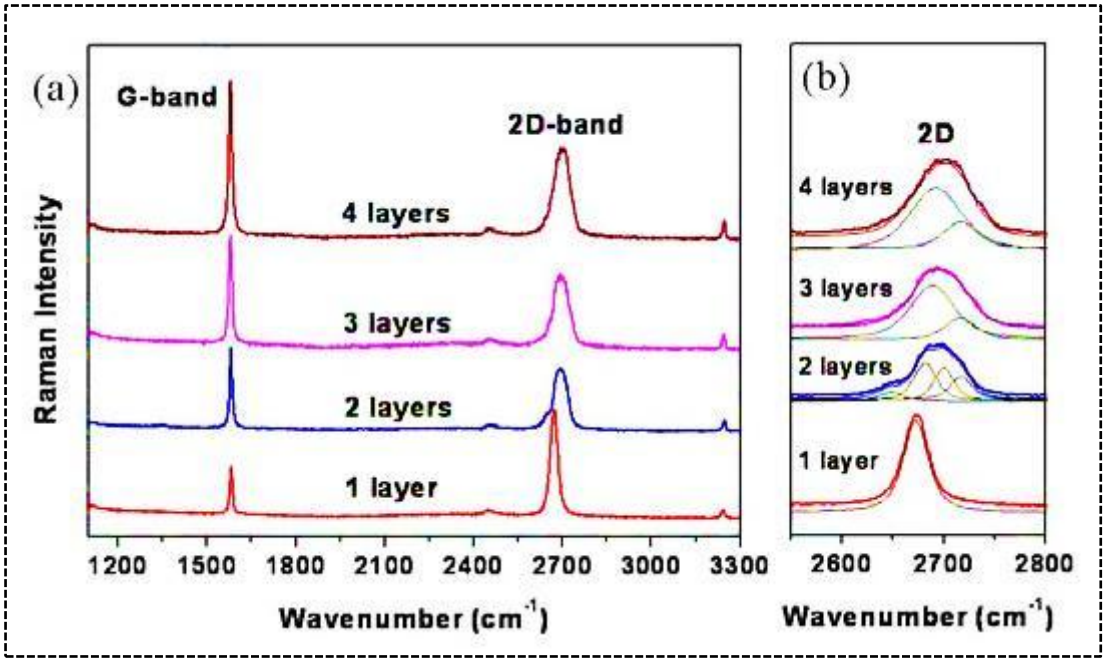

Figure 3-8: Typical Raman spectra of monolyer and few layer graphene (left) showing the broadening of 2D band (enlarged on the right) (adapted from Ref. [65]).

Raman spectroscopy has been used in this thesis to characterize suspended graphene structures. Although AFM topography can provide the thickness of the graphene samples, the method is not accurate for estimating monolayer and few-layer graphene as the error bar in the AFM is ±1 nm. Hence only for multilayer structures (> 8 nm) AFM has been used to extract the thickness.

3.4 Singletron Accelerator

The ion beam facility at Centre for Ion Beam Applications (CIBA) in NUS is equipped with a 3.5 MV singletron accelerator from High Voltage Engineering Europa (HVEE) in conjunction with five beam lines. The schematic of the facility along with a photograph is shown in Figure 3-9. The energy of the ion beam which originates from the accelerator is controlled by a 90° analysing magnet. The ion beam and the target chamber can be precisely chosen using a switching magnet. Magnetic quadrupole lens is used to focus the ion beam before the target chamber by creating a demagnified image of the object slits. The steerer table allows for rough focussing and monitoring of the beam. The defining slits and the

aperture enable to define the beam diameter and optimization. Using a computer controlled software the dose and the scanning can be controlled for irradiation tasks.

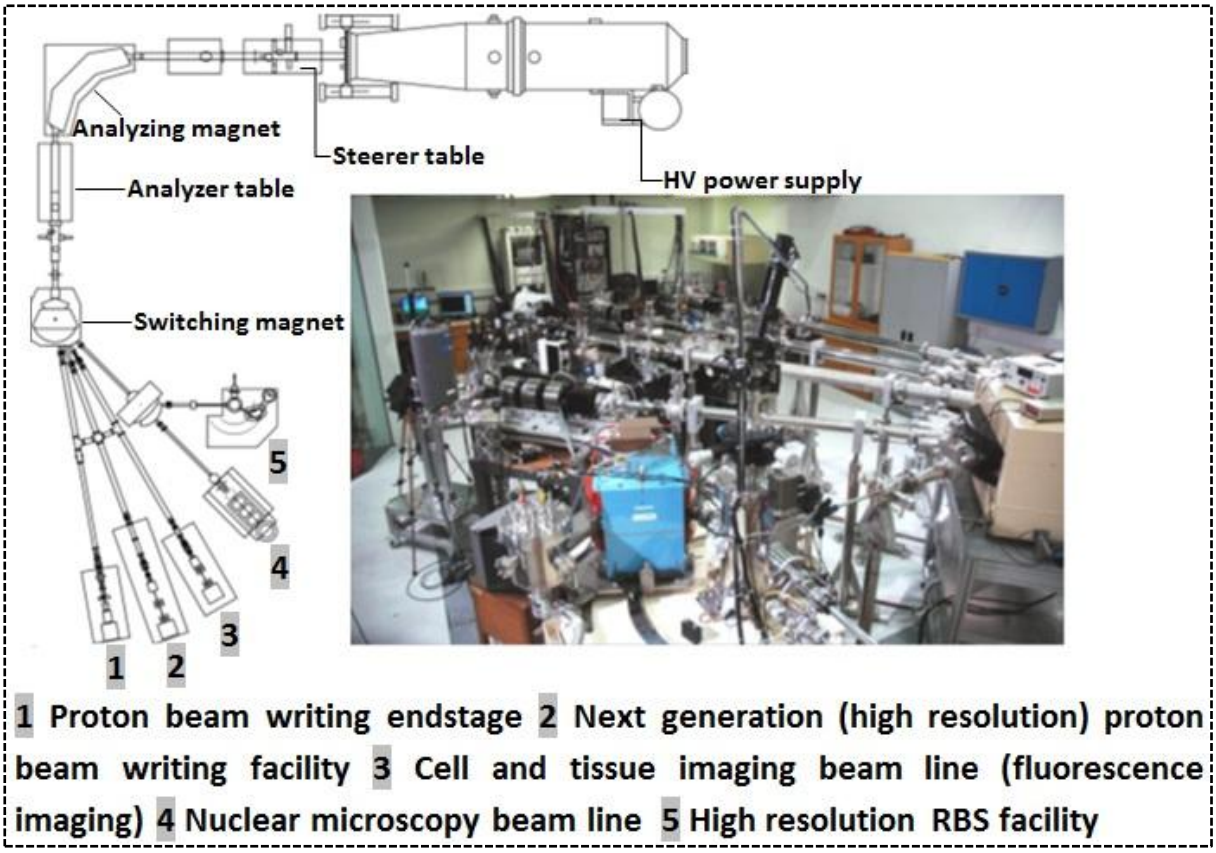

Figure 3-9: Schematic of the ion beam facility at CIBA (Department of Physics, NUS) (left) and a photograph of the facility (right).

In this thesis, the helium ion irradiation experiments were carried out using this 3.5 MV singletron facility. The experimental procedures and the obtained results are discussed in detail in Chapter 7.

3.5 Helium Ion Microscope (HIM)

A new cutting edge tool in the field of nanofabrication is the Carl Zeiss Orion NanoFab. The photograph of the instrument and the schematic of the tool are shown in Figure 3-10. The two most important technology advancements of this tool are ion source and the nature of the beam interaction with the sample that is being imaged. This technique is based on the field ionization of helium ions using a cryogenically cooled metal tip such as tungsten which is

truncated by trimer of atoms (metal tip is positively biased and is exposed to very low quantities of helium under vacuum and is modified such that only three atoms remain at the edge of the tip). Under large bias, ion streams are emitted by the trimer which is then aligned and focussed by optics column to obtain the helium ion beam. This beam is rastered across the sample to obtain images. Apart from imaging, HIM has the capability to directly pattern arbitrary features with sub -10 nm dimensions on both supported and suspended graphene [67][68]. This is a direct patterning method without using any resists. Moreover, one has the freedom to pattern any arbitrary design and the patterned structures will be devoid of any contamination arising from the resists used in conventional lithography methods.

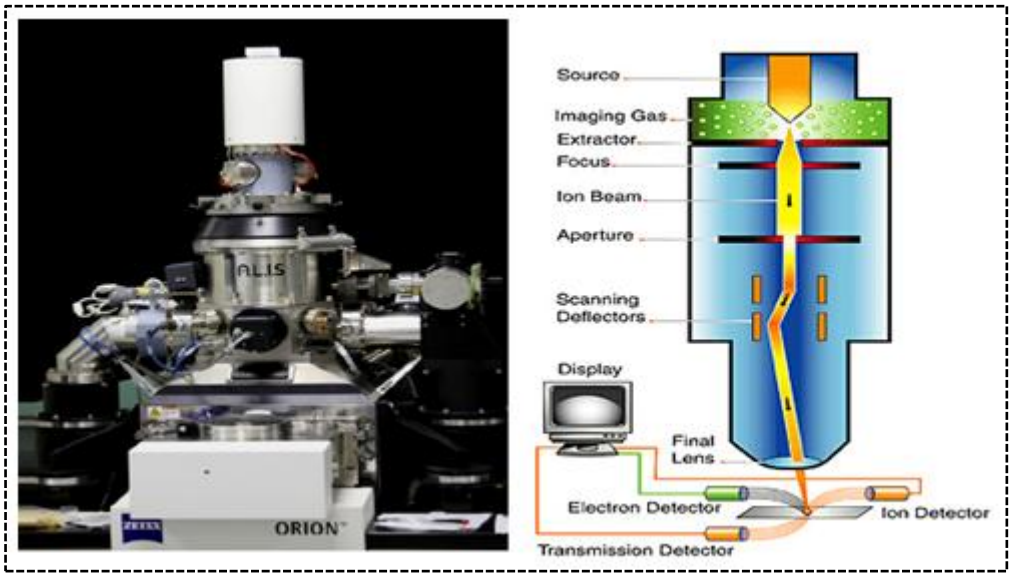

Figure 3-10: Photograph of HIM (left) and the schematic of the tool (right) (adapted from Ref. [61]).

This tool has been used to pattern the fabricated samples and the results are shown in detail in Chapter 8.

CHAPTER 4 : FABRICATION AND CHARACTERIZATION OF GRAPHENE DRUM STRUCTURES

4.1 Introduction

Various published work in recent years have established the feasibility of suspended graphene as nanoscale electromechanical devices, with much of these studies focusing on the resonance properties of graphene sheets. Few-layer graphene sheets suspended over a silicon dioxide trench have been demonstrated to operate as clamped-clamped beam resonators at frequencies as high as 70 MHz with Q-factors of ~100 [69]–[71]. Drum structures fabricated from graphene oxide have also been shown to resonate at frequencies up to ~60 MHz with Q-factors of ~4000 by Robinson et al. [72], although the Young's modulus of graphene oxide is significantly lower (~185 GPa). Due to their low mass and superior stiffness (compared to silicon), graphene structures hold plenty of promise in mass sensing applications. The sensitivity of a resonant mass sensor is proportional to the mass of the sensing element and inversely proportional to its resonance frequency [73]. Few-layer graphene structures have lateral dimensions of a few microns and are no more than a few nanometers thick [69]–[71], which makes their mass very small. The substantially higher Young's modulus of graphene also makes such structures much stiffer and hence resonates at higher frequencies. This makes the mass/resonance frequency ratio of graphene structures significantly better than silicon-based ones which in turn results in an improvement in the mass sensitivity. However, before graphene structures can be employed in practical devices, it is first necessary to characterize the mechanical properties of the structures themselves. While previous studies [69]–[71] have featured extensive measurements on structure characteristics such as resonance frequency and Q-factor, analytical modelling and simulation of the structures' mechanical behaviour remains somewhat lacking. Such efforts can help assess the potential performance of graphene structures in various applications. Various theoretical studies on the mechanics of graphene sheets based on atomistic [74], continuum [75] and hybrid [76]–[78]

models have also been presented; however, these studies do not involve measurements on actual graphene structures.

4.2 Experimental Details

The devices for characterization were prepared by adopting the technique described in Section 3.1.

4.2.1 Test Setup for Characterization

Suitable candidates for measurement were identified optically, looking for few-layer graphene sheets suspended over a trench and contacting at least one gold electrode line. The graphene sheet is in electrical contact with the electrode as long as part of the sheet overlaps the gold line. This overlapping is verified by topographical scans using AFM. An optical micrograph of one of the graphene drum samples (labeled Device 2) is shown in Figure 4-1(a). The 285 nm thick oxide layer appears violet under optical microscopy with pieces of graphene turning up in colours ranging from deep violet to blue, depending on the layer thickness. However, optical imaging is insufficient for quantifying the number of layers of the selected graphene sheets and hence AFM was employed to measure the thickness.

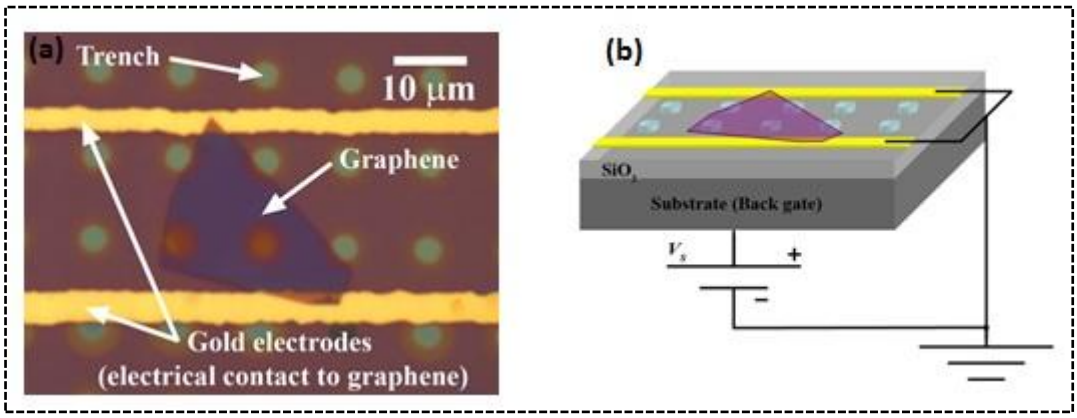

Figure 4-1: (a) Optical micrograph of a suspended graphene drum device (labeled as Device 2). (b) Wiring of the graphene drum structure for static deflection measurements. A voltage V_S was applied across the back gate and the graphene.

Static deflection experiments were then carried out to investigate the mechanical properties of the suspended graphene drums. Both fabrication and device testing were carried out at room

temperature (~28 °C). The devices were wired up as shown in Figure 4-1(b) and a voltage V_S was applied across the back gate and the graphene. Since the graphene is grounded (0 V potential) and the back gate is positively biased at V_S, an electrostatic force is induced between the two surfaces which in turn works to deflect the suspended graphene. This deflection was then detected using AFM (JEOL JSPM-5200). The AFM is highly sensitive to topographical changes in the out-of-plane direction and can pick up height variations as small as 1 nm. The AFM scans obtained provide information on both the peak displacement amplitude as well as the deflection mode shape of the drum structure.

The micrograph in Figure 4-2(a) is a two-dimensional representation of the topographical data of the scanned region, with the colour contrast being a direct indication of the height of the sample at a particular scan point. The darker regions represent areas which are lower in height compared to the brighter regions. Figure 4-2(b) is a three-dimensional plot of the data and Figure 4-2(c) is a graph of the height variation across the diameter of the sample, showing the cross-sectional profile of the graphene.

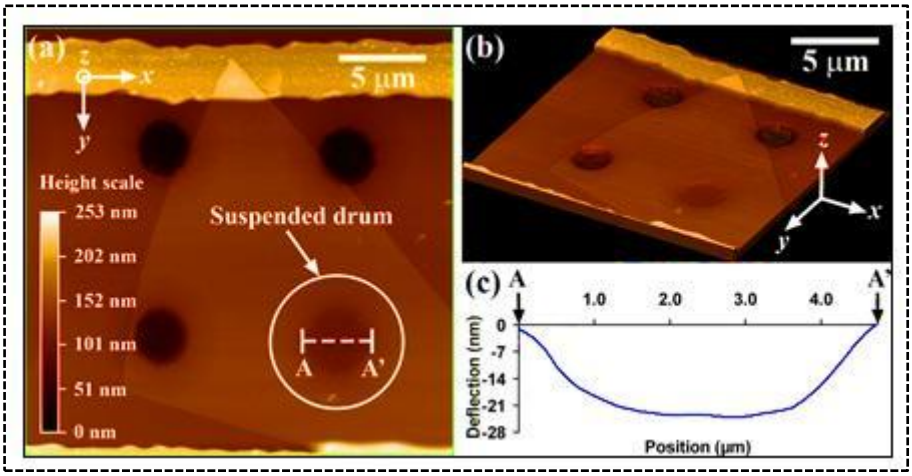

Figure 4-2(a): AFM scan of Device 2 at V_S = 0 V. The colour contrast in the micrograph is representative of the topographical data at each region (refer to height scale). The suspended graphene drum is located at the lower right. (b) A 3D representation of the scan in (a) showing the layer suspension and the thinness of the graphene. (c) Graph of the height variation at the diameter AA' of the device showing initial sag of 24 nm.

Despite the best efforts taken during sample preparation, it was unable to obtain suspended drum structures that were completely flat over the trench opening but instead all the devices fabricated had an initial sag which caused them to have a parabolic cross-sectional profile despite no actuation voltage V_S being applied (see Figure 4-2(c)). As graphene is extremely lightweight and has extraordinary stiffness, it is unlikely that the weight of the structure pulling down at its central point could cause this much sag or initial deflection. It is also improbable that compressive stress is the cause for the initial sag as it is known that suspended graphene sheets are instead affected by uniaxial tensile stress [79]–[80], which would in fact stretch the graphene and reduce the degree of initial sag. The most plausible explanation for the presence of the initial sag is that the area of material covering the trench is greater than the area of the opening, resulting in the excess graphene having to fit into the trench itself which gives rise to some sagging. Similar phenomenon is observed for other devices fabricated by mechanical exfoliation of graphene [81].

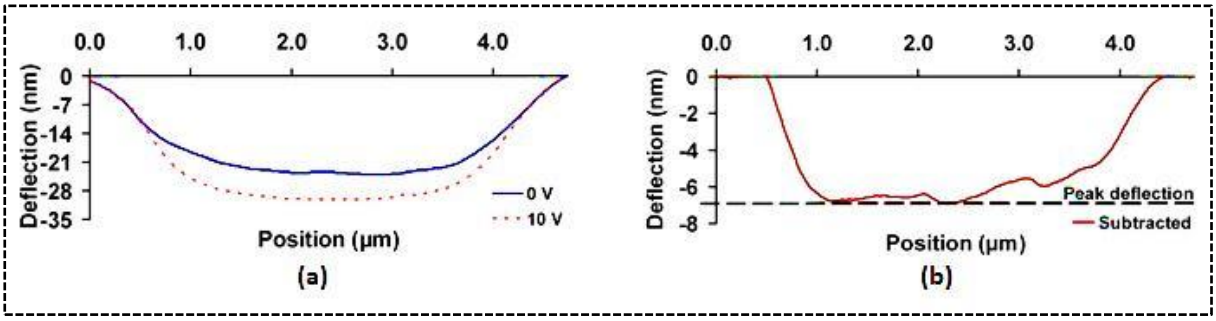

Figure 4-3: (a) Cross-sectional profiles of Device 2 when unbiased (V_S = 0 V) and when biased at V_S = 10 V. (b) Resultant cross-section obtained after subtracting the biased and unbiased profiles. The peak deflection of Device 2 at V_S = 10 V is 6.9 nm.

To determine the static deflection induced, a scan of the unbiased device was first taken to determine the initial state of the drum. A second scan of the same region was then taken while a voltage V_S was applied to the back gate. The cross-sectional profile of the unbiased scan was then subtracted from the biased scan (see Figure 4-3) and the resulting profile is the deflection mode shape of the graphene drum with the lowest point of the profile being the peak deflection. By performing the profile subtraction, the deflection at each point of the

sagging graphene sheet, caused by the applied electrostatic force, is extracted. Hence, the subtracted profile provides a reasonable indication of the change in the deflection from the initial state of the drum. This method of determining the peak deflection and deflection mode shape was used for all our subsequent measurements.

The drum structures are essentially clamped circular plates made of graphene and hence their mechanical motion can be modelled using plate theory. The following section presents a theoretical framework for analyzing the static deflection of the graphene drums.

4.3 Analytical Modelling and Finite Element Simulations

The nanomechanical graphene drums are geometrically similar to solid circular plates and hence, it would be meaningful to use plate theory for estimating the peak deflections of these structures. When the deflections of the drum structure are small in comparison with its thickness, pure bending theory can be accepted. However, for large deflections (i.e. when the deflections are greater than half the thickness), stress-stiffening becomes significant and the spring constant of the drum increases with deflection magnitude [82]. The relationship between applied force and deflection thus becomes nonlinear. As our drum devices exhibit large deflection in experiment, their mechanical behaviour cannot be modelled using pure bending theory. In order to estimate the peak deflections of these structures, an approximate solution has been derived below.

4.3.1 Approximate Solutions for Large Deflection of Uniformly Loaded Graphene Drums

The four devices used in experiments are clamped graphene drums; hence an approximate solution for maximum deflection is derived for graphene drums with clamped boundaries. Due to the structural similarities between graphene drums and solid circular plates, the equations derived below are based on plate theory.

From the classical theory of plates, we know that, the peak deflection d_0 is at the centre of the plate and is given by [82],

$$d_0 = \frac{Pa^4}{64D} \tag{4.1}$$

where P is the uniform loading, a is the radius of the plate and D is the flexural rigidity. For a thin elastic plate of thickness h,

$$D = \frac{Eh^3}{12\left(1-\nu^2\right)} \tag{4.2}$$

where E is the Young's modulus and ν is the Poisson's ratio.

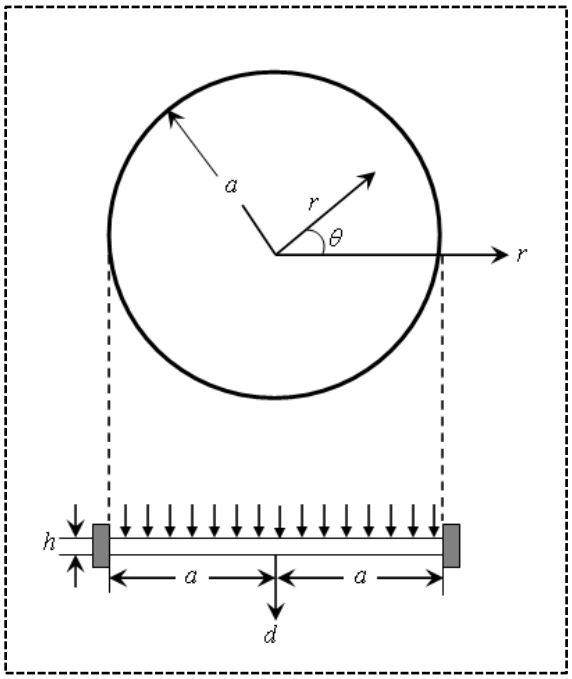

Figure 4-4: Clamped drum structure under uniformly distributed load.

A clamped drum structure under uniformly distributed load is shown in Figure 4-4. The boundary conditions for clamped graphene drums are $\left(d_0\right)_{r=a} = 0$ and $\left(\frac{\mathrm{d}d_0}{\mathrm{dr}}\right)_{r=a,0} = 0$. The parameter d_0, r and a represent the maximum displacement, radial coordinate and radius of the graphene drum respectively.

In order to derive the equations for large static deflection, an energy method proposed by Timoshenko, S. P. is used [82]. His method has been outlined in this section, but the final derived equation is specific to graphene drums.

The shape of the deflected drum for large deflections is assumed to be the same as in small deflections. Hence, the deflection *d* at any point of the circular plate can be described by,

$$d = d_0\left(1-\frac{r^2}{a^2}\right) \tag{4.3}$$

As the deflection of the drum is symmetric about the centre (i.e. *d* is a function of *r*), the corresponding equation describing the strain energy U_{bend} due to bending of the plate is,

$$U_{bend} = \frac{D}{2}\int_0^{2\pi}\int_0^{a}\left\{\left(\frac{\partial^2 d}{\partial r^2}\right)^2 + \frac{1}{r^2}\left(\frac{\partial d}{\partial r}\right)^2 + \frac{2\nu}{r}\frac{\partial d}{d}\frac{\partial^2 d}{\partial r^2}\right\} r\mathrm{d}r\mathrm{d}\theta \tag{4.4}$$

As $d = d_0\left(1-\frac{r^2}{a^2}\right)$, the strain energy equation can be reduced to,

$$U_{bend} = \frac{D}{2}\int_0^{2\pi}\int_0^{a}\left\{\left(\frac{\partial^2 d}{\partial r^2}\right)^2 + \frac{1}{r^2}\left(\frac{\partial d}{\partial r}\right)^2 + \frac{2\nu}{r}\frac{\partial d}{d}\frac{\partial^2 d}{\partial r^2}\right\} r\mathrm{d}r\mathrm{d}\theta = \frac{32\pi}{3}\frac{{d_0}^2}{a^2}D \tag{4.5}$$

The polynomial expression representing the radial displacement *u* (from stretching of the circular plate) is given by,

$$u = r(a-r)(C_1 + C_2 r + C_3 r^2 + ...) \tag{4.6}$$

Each term in this equation should satisfy the boundary condition and *u* should be equal to zero at the centre and at the edge of the solid drum.

From Equations (4.3) and (4.6), the strain components ε_r and ε_t of the middle plane are estimated. The strain energy $U_{stretch}$ due to stretching of the middle plane is given by,

$$U_{stretch} = 2\pi \int_0^a \left(\frac{N_r \varepsilon_r}{2} + \frac{N_t \varepsilon_t}{2} \right) r\mathrm{d}r - \frac{\pi E h}{1-\nu^2} \int_0^a \left(\varepsilon_r{}^2 + \varepsilon_t{}^2 - 2r\varepsilon_r \varepsilon_t \right) r\mathrm{d}r \tag{4.7}$$

The strain on the middle surface of the drum can be neglected, when the maximum deflections of the drum are small in comparison to its thickness. However, when the deflections are comparable to the drum thickness or larger than the thickness itself, the effect of strain should be included.

The strain energy due to stretching of the middle plane can be reduced to the following equation by omitting the higher order terms.

$$\begin{aligned} U_{stretch} = \frac{\pi E h a^2}{1-\nu^2} \Bigg(& 0.250 C_1^2 a^2 + 0.1167 C_2^2 a^4 + 0.300 C_1 C_2 a^3 - 0.00846 C_1 a \frac{8 d_0{}^2}{a^2} \\ & + 0.00682 C_2 a^2 \frac{8 d_0{}^2}{a^2} + 0.00477 \frac{64 d_0{}^4}{a^4} \Bigg) \end{aligned} \tag{4.8}$$

When the total energy of the drum is minimum, the constants C_1 and C_2 are estimated.

$$\frac{\partial U_{stretch}}{\partial C_1} = 0 \text{ and } \frac{\partial U_{stretch}}{\partial C_2} = 0 \tag{4.9}$$

Substituting Equation (4.8) in Equation (4.9) yields two simultaneous equations. Solving the two equations gives,

$$C_1 = 1.202 \frac{d_0{}^2}{a^3} \text{ and } C_2 = -1.78 \frac{d_0{}^2}{a^4} \tag{4.10}$$

The expressions for the constants C_1 and C_2 are substituted in Equation (4.8) and the following equation for stretching energy is obtained.

$$U_{stretch} = 2.5907 \pi D \left(\frac{d_0{}^4}{a^2 h^2} \right) = 2.357 \left(\frac{1}{1-\nu^2} \right) \pi D \left(\frac{d_0{}^4}{a^2 h^2} \right) \tag{4.11}$$

The total strain energy is the sum of bending and stretching energies and is given by,

$$U_{bend} + U_{stretch} = \frac{32}{3}\pi D \frac{{d_0}^2}{a^2}\left(1 + \frac{0.2209}{1-\nu^2}\frac{{d_0}^2}{h^2}\right) \tag{4.12}$$

When the load on the plate increases, the middle plane of the drum gets stretched as the maximum deflection values tend to go beyond the values of the drum thickness. This stretching or strain effect in the middle surface of the graphene drum has been compensated by introducing a correction factor and the second term in Equation (4.12) represents this. By applying the principle of virtual displacements, the deflection of the drum can be obtained.

$$\frac{\mathrm{d}\left(U_{bend} + U_{stretch}\right)}{\mathrm{d}d_0}\delta d_0 = 2\pi \int_0^a P\delta d r \mathrm{d}r = 2\pi P \delta d_0 \int_0^a \left(1 - \frac{r^2}{a^2}\right)^2 r \mathrm{d}r \tag{4.13}$$

where P is the uniformly distributed load.

By substituting Equation (4.12) in Equation (4.13) and using the Poisson's ratio for graphene as $\nu = 0.16$ [57][81], we get,

$$d_0 = \frac{Pa^4}{64D} \times \frac{1}{1 + \frac{.4418}{1-\nu^2}\frac{d_0^2}{h^2}} = \frac{Pa^4}{64D} \times \frac{1}{1 + 0.453\frac{d_0^2}{h^2}} \tag{4.14}$$

When the maximum deflections of the drum are small compared to the thickness of the drum, then the last term in Equation (4.14) becomes negligible and the relationship between force and maximum deflection would be linear. When the deflection values get closer to the drum thickness or larger than the thickness itself, then the second term in Equation (4.14) would reduce the deflection value, i.e. a part of the total energy applied will go into stretching the middle plane of the drum, leaving less energy for bending, hence reducing the total displacement.

The maximum displacement of the graphene drum structure subjected to different distributed load values and the mode shape of the deflections were also validated using finite element simulations. The method adopted for simulation and results obtained are discussed in the following section.

4.3.2 Finite Element Simulation

The mechanical behaviour of the nanomechanical graphene drum structures were also simulated using the finite element tool ANSYS. FEM helps to achieve a detailed visualization of where the graphene drum structures deflect and also reveals the distribution of these displacements. The ANSYS software is capable of handling the nonlinear effects and has been used in this case to estimate the peak static deflections of the graphene drums and also the mode shape of the deflections.

The graphene drum structures were modelled as thin circular plates using elements which account for the lateral geometric deformation that takes place during large bending. The graphene drums were built using SOLID45 element type. This element type is used for 3-D modelling of solid structures and is capable of handling stress stiffening and large deflections. The material properties used in the simulations include Young's modulus E = 1TPa, Poisson's ratio ν = 0.16 and material density ρ = 2200 kg m^{-2}. These values used are the known values for bulk graphite [57]. The built graphene drums were anchored along its periphery to get clamped boundaries and a very fine meshing was done to get accurate deflection results. Figure 4-5(a) shows a meshed 4.74 μm diameter graphene drum with clamped boundaries and uniformly distributed load. The "large displacement static" static analysis option was chosen under solution controls to account for the nonlinearity in peak deflections.

The electrostatic force F was calculated using the parallel plate equation and applied as a uniformly distributed load over the circular surface in the model,

$$F = \frac{\varepsilon_0 \varepsilon_r A V_S^{\,2}}{2(g - d_0)^2} \tag{4.15}$$

where ε_0 = 8.854 × 10^{-12} Fm^{-1} is the permittivity of free space, ε_r is the effective relative permittivity, $A = \pi a^2$ is the area of the graphene drum, V_S is the applied voltage, g is the initial gap (= 285 nm – initial sag of the drum) and d_0 is the peak deflection. The effective relative permittivity ε_r accounts for possible electric field enhancement effects caused by the presence of residual oxide at the bottom of the trench structure and is given by,

$$\varepsilon_r = \frac{\varepsilon_{air} t_{air} + \varepsilon_{ox} t_{ox}}{t_{air} + t_{ox}} \tag{4.16}$$

where ε_{air} = 1 is the relative permittivity of air, t_{air} is the initial air gap (= trench depth – initial sag of the drum), ε_{ox} = 3.9 is the relative permittivity of SiO_2 and t_{ox} is the residual oxide thickness.

The electrostatic force is converted to uniform load/pressure ($P = F/A$) and is then applied on the top surface of the drum as shown in Figure 4-5(a). The pressure applied causes the drum to deflect. The outcome of this is recorded as the deflection profile with peak deflection value. Figure 4-5(b) shows the isometric view of the 3-D finite element model (built using ANSYS) used to simulate the electrostatic deflection of Device 2, actuated at V_S = 20 V. The simulated deflection profile (mode shape) is shown below with a peak deflection of 35.9 nm.

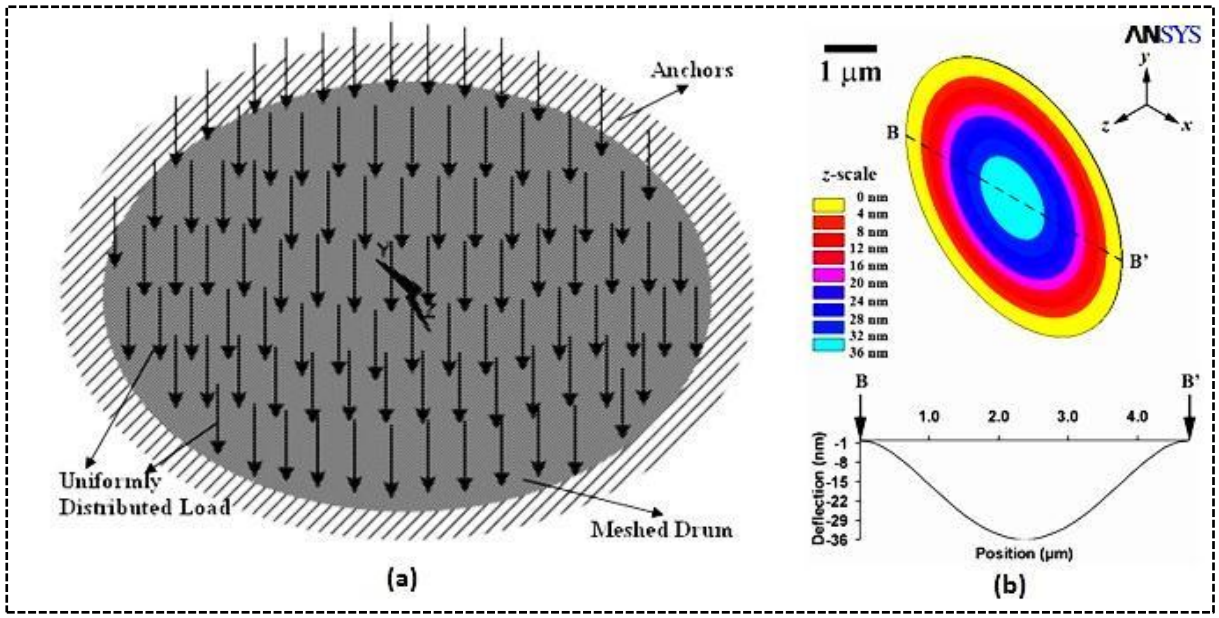

Figure 4-5: (a) Image of meshed Device 2 (4.74 µm diameter graphene drum) with clamped boundaries and uniformly distributed load. (b) Isometric view of Device 2 and its deflection profile indicating the maximum deflection (applied voltage V_S = 20 V).

A total of four nanomechanical graphene drum structures were fabricated and the measurements of their static deflection are presented in the following section. The analytical and finite element simulation models presented in this section were also used to obtain the theoretical/simulated deflections and mode shape of the samples and a comparison of the experimental results and modelled data are also made.

4.4 Experimental Results & Discussion

The static deflection experiment results from our four sample devices are presented in this section. Table 4-1 summarizes the dimensional characteristics of the four suspended drum structures that were successfully fabricated using the process depicted in Figure 3-1. The trench depths indicate the amount of oxide that was removed during BHF etching from the initial 285-nm thick oxide layer. This initial sag for each device is also indicated in Table 4-1.

Table 4-1: Summary of dimensional characteristics of the graphene drum structures

Label	Dimensions		Trench depth (nm)	Residual oxide thickness, t_{ox} (nm)	Initial sag (nm)
	Diameter, 2*a* (μm)	Thickness, *h* (nm)			
Device 1	3.86	12	85	200	18
Device 2	4.74	15	100	185	24
Device 3	5.70	8	200	85	114
Device 4	3.88	10	80	205	40

4.4.1 Static Deflection

Each of the four sample devices were wired up as shown in Figure 4-1(b) and their peak deflections were recorded at various applied V_S. The static deflection measurements for all four of our drum devices are summarized in Figure 4-6. The measurement error contributed by the AFM is about 1 nm. However, since the diameters of each drum structure are different, the electrostatic force experienced by each device varies for the same applied voltage V_S. The electrostatic force is calculated using Equation (4.15) and the peak deflection data is re-plotted as force-deflection curves in Figure 4-7. What is immediately apparent is the nonlinear relationship between applied electrostatic force and measured peak deflection which is consistent across all the samples. This is to be expected as the largest deflection for each device is about or larger than the thickness of the graphene sheet. A nonlinear force-deflection relationship was also observed by [9] during nanoindentation experiments on suspended monolayer graphene membranes. Using an assumed Young's modulus of 1 TPa for graphene, the theoretical deflections of all four samples were calculated using Equation (4.14) and simulated with ANSYS. These data are also presented in Figure 4-7.

For Device 1 and 4 (see Figure 4-7(a) and Figure 4-7(d)), the three sets of results are in good agreement, indicating that the actual Young's modulus of our graphene structures is indeed

close to 1 TPa. Prior theoretical [8] and experimental [9] studies on the mechanical properties of graphene have turned up similar values for its Young's modulus. However, some discrepancies in the experimental data can be observed for Device 2 and 3 (see Figure 4-7(b) and Figure 4-7(c)) which contradicts the previous conclusion. The source of these discrepancies may be better understood by studying the deflection mode shapes of the drums which will be discussed in the following section.

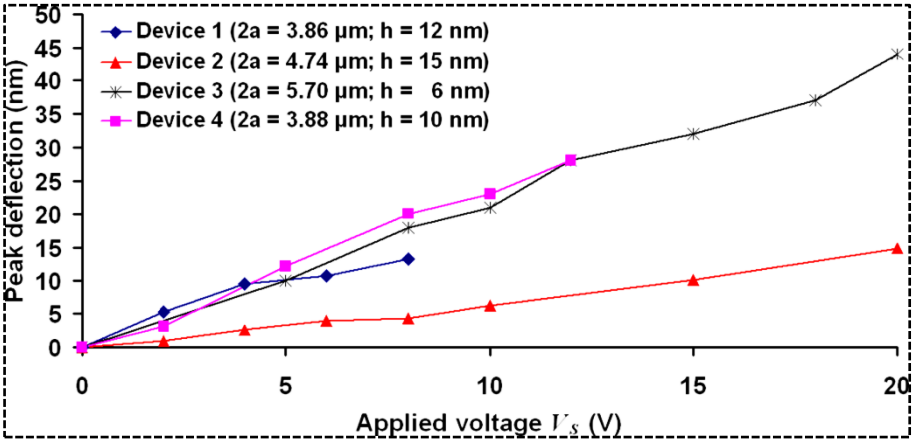

Figure 4-6: Measured peak deflection plotted against applied voltage V_S for Device 1 to 4.

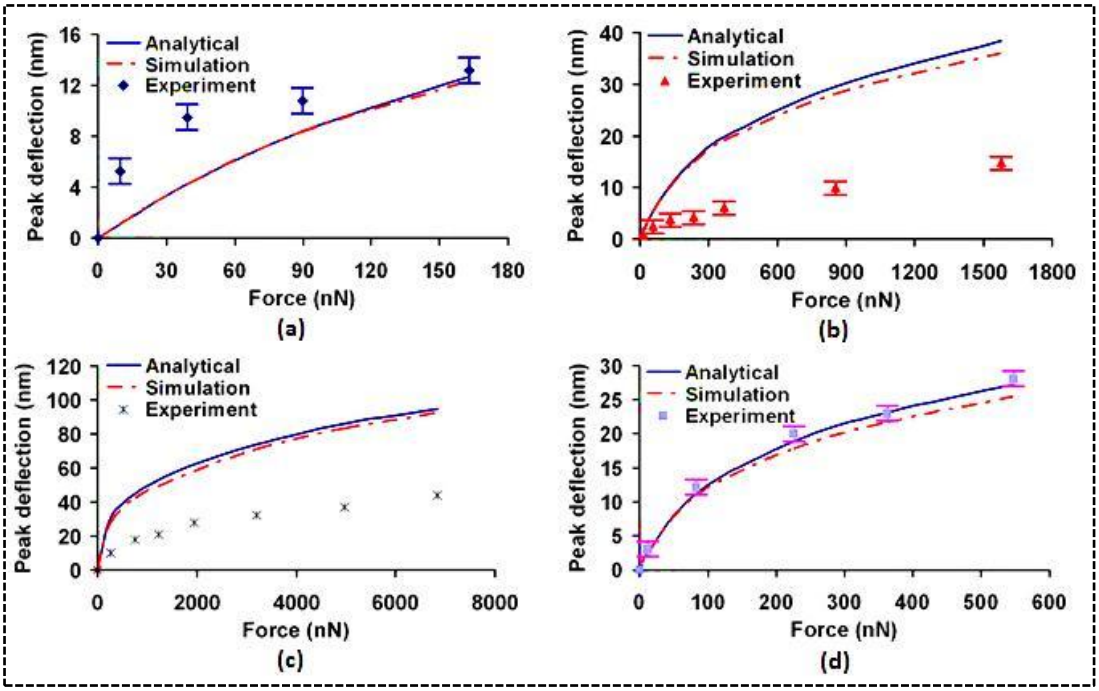

Figure 4-7: Analytical, simulated and experimental force-deflection plots for (a) Device 1, (b) Device 2, (c) Device 3 and (d) Device 4. Measurement error contributed by the AFM is ±1 nm as reflected by the error bars (error bars are omitted for (c) as the measurement span is significantly larger than the error). The electrostatic force is calculated using Equation (4.15) and with an effective relative permittivity.

Other mechanical parameters of the drums which can be deduced from the experimental force-deflection data include the linear and nonlinear spring constants. The equation of motion describing the nonlinear static deflection of the graphene drum is,

$$F = -k_1 d_0 - k_3 d_0^{\,3} \tag{4.17}$$

where F is the applied electrostatic force and k_1 and k_3 are the linear and nonlinear spring constants respectively. The analytical spring constants derived from Equation (4.14) are,

$$k_1 = \frac{17.2Eh^3}{a^2} \text{ and } k_3 = \frac{7.79Eh}{a^2} \tag{4.18}$$

Similar forms for the linear and nonlinear spring constants have also been derived in other studies [75]–[78].

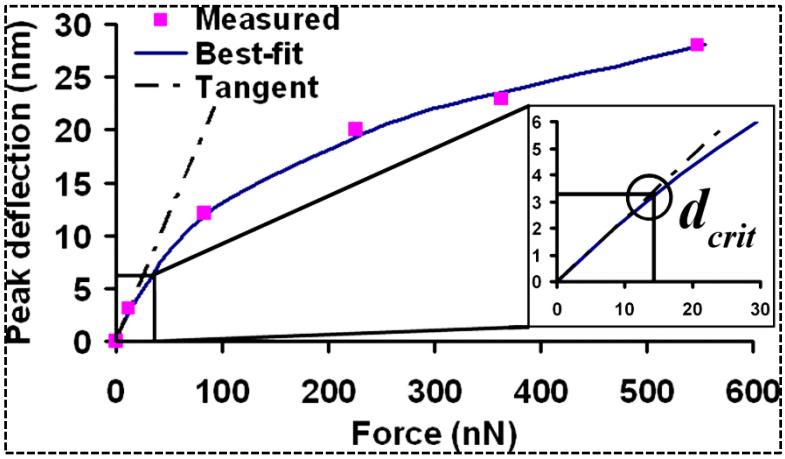

Figure 4-8: Best-fit curve (obtained using method of least squares) through the measured deflections for Device 4. The critical deflection amplitude d_{crit} is derived from the point at which the best-fit curve diverges from the tangent (shown in inset).

The experimental values for k_1 and k_3 can be obtained by fitting the measured deflections for each device to Equation (4.17) using the method of least squares. Figure 4-8 shows the best-fit curve for Device 4 from which the spring constants k_1 = 4.21 N m^{-1} and k_3 = 0.0197 N m^{-3} are acquired. In addition, the critical deflection amplitude d_{crit}, defined as the maximum amplitude which the drum can be actuated to before it displays nonlinear behaviour, can also

be derived from the best-fit curve. To achieve this, a straight line passing through the origin is drawn tangent to the best-fit curve (see Figure 4-8) with d_{crit} being the point at which the line and curve diverge.

Table 4-2: Summary of measured mechanical parameters of the graphene drum structures

Device	Measured		Analytical (Eq. (18))		FEM Simulation		d_{crit} (nm)	h (nm)	$\frac{d_{crit}}{h}$ (%)
	k_1 (N m^{-1})	k_3 (N m^{-3}) x 10^{16}	k_1 (N m^{-1})	k_3 (N m^{-3}) x 10^{16}	k_1 (N m^{-1})	k_3 (N m^{-3}) x 10^{16}			
1	6.11	4.00	7.98	2.51	7.18	2	2.34	12	19.5
2	37.6	12.7	10.33	2.62	9.81	2.64	3.96	15	26.4
3	3.24	8.47	1.08	0.767	0.821	0.832	1.42	8	17.8
4	4.21	1.97	4.57	2.07	4.38	2.12	3.36	10	33.6

Table 4-2 summarizes the measured mechanical parameters for each of the four samples. Analytical (derived using Equation (4.18)) and FEM simulated values have also been included. The measured spring constant values for Device 1 and 4 are in fairly good agreement with analytical calculations and simulation while, as is the case for the force-deflection curves, some deviation is observed for Device 2 and 3. The data presented in Table 4-2 shows that the drums can be actuated to about 18 – 34 % of their thickness before displaying nonlinear deflection. For the first three samples, we also observe that d_{crit} increases with h or with k_1. This appears to suggest that thicker or stiffer (with larger k_1) devices may actually be more resilient to nonlinear behaviour (i.e. they can sustain larger vibration amplitudes before exhibiting nonlinearity). However, a larger sample size is required to validate this conclusion. In the following section, an investigation of the

deflection mode shapes of the drums is presented which may reveal some of the causes for the non-conformal deflection behaviours of Device 2 and 3.

4.4.2 Deflection Mode Shape

The AFM scans also provide information on the curvature of the nanomechanical drum structures during actuation and these profiles are indicative of the structures' deflection mode shapes. A plot of the measured deflection mode shapes of Device 1 to 4 during actuation is shown in Figure 4-9. From the mode shapes, we can observe that while Device 1 and 4 (see Figure 4-9(a) and Figure 4-9(d)) maintain roughly parabolic deflection profiles, the mode shapes displayed by Device 2 and 3 (see Figure 4-9(b) and Figure 4-9(c)) are significantly different. The expected deflection mode shape of a clamped circular plate, obtained via analysis and simulation, are also shown in Figure 4-9. It is obvious that while the deflection profiles of Device 1 and 4 follow the analytical and simulated mode shapes quite closely, the mode shapes of Device 2 and 3 both do not match up. In both instances (for Device 2 and 3) it appears that the underlying trench may actually be the main contributor to the mode shape deformation. As the trench structures are prepared by means of wet etching (refer to Section 3), it is exceedingly difficult to achieve 90° sidewalls due to the isotropic nature of the etch. If the sidewall of the trench is not etched steep enough, the area near the circumference of the suspended graphene may actually stick to the sidewall as the drum deflects.

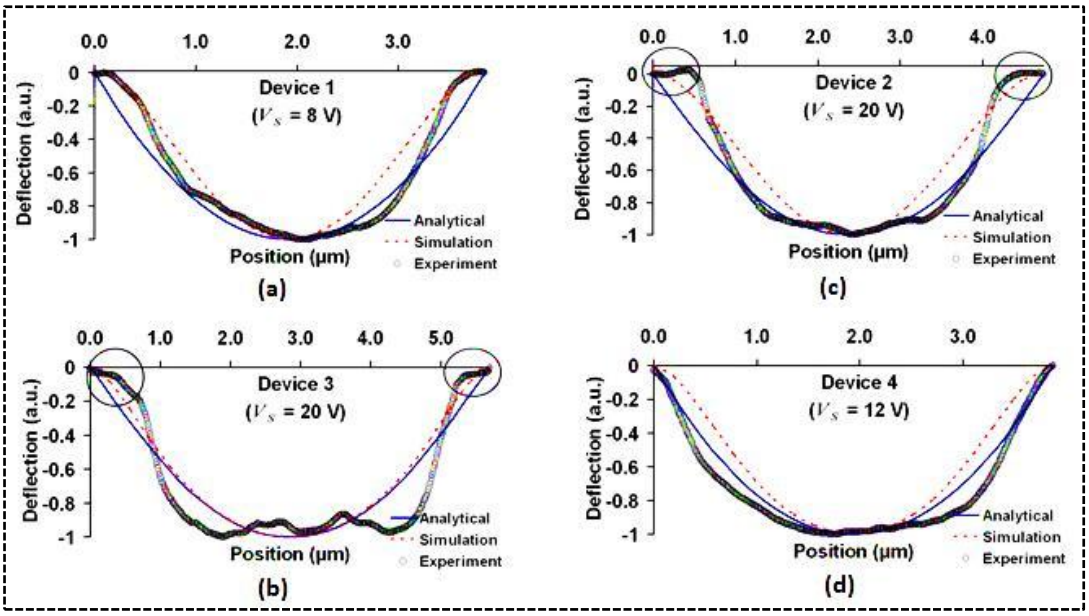

Figure 4-9: Analytical, simulated and experimental deflection mode shapes of (a) Device 1, (b) Device 2, (c) Device 3 and (d) Device 4 at their highest actuation voltages V_S.

The peak deflections are scaled so that only the shapes of the profiles are compared. The experimental mode shapes of Device 1 and 4 are in good agreement with theory and simulation. However, the mode shapes of Device 2 and 3 are flat near the circumference of the drums (see circled regions), possibly resultant from the graphene sticking to the sidewalls of the underlying trench.

To confirm this hypothesis, the graphene layers for both Device 2 and 3 were stripped from the substrate using oxygen plasma and an AFM scan was then carried out on the underlying trenches. Figure 4-10 shows the cross-sectional profile of the trenches overlaid with the deflection mode shapes of Device 1, 2, 3 and 4 (at their highest actuation voltages). It is clear, from the profiles in Figure 4-10, that part of the graphene layer is indeed touching the sidewalls of the trench for Device 2 and 3. The effect of this phenomenon is a reduction in the diameter of the suspended drum structure and an increase in its stiffness. The area exposed to the biased back gate also decreases, resulting in a reduction in the electrostatic force. These two effects combine to reduce the overall deflection of the drum, which is consistent with our results in Figure 4-10(b) and Figure 4-10(c), where the measured

deflections for both Device 2 and 3 are consistently less than the analytical and simulated data.

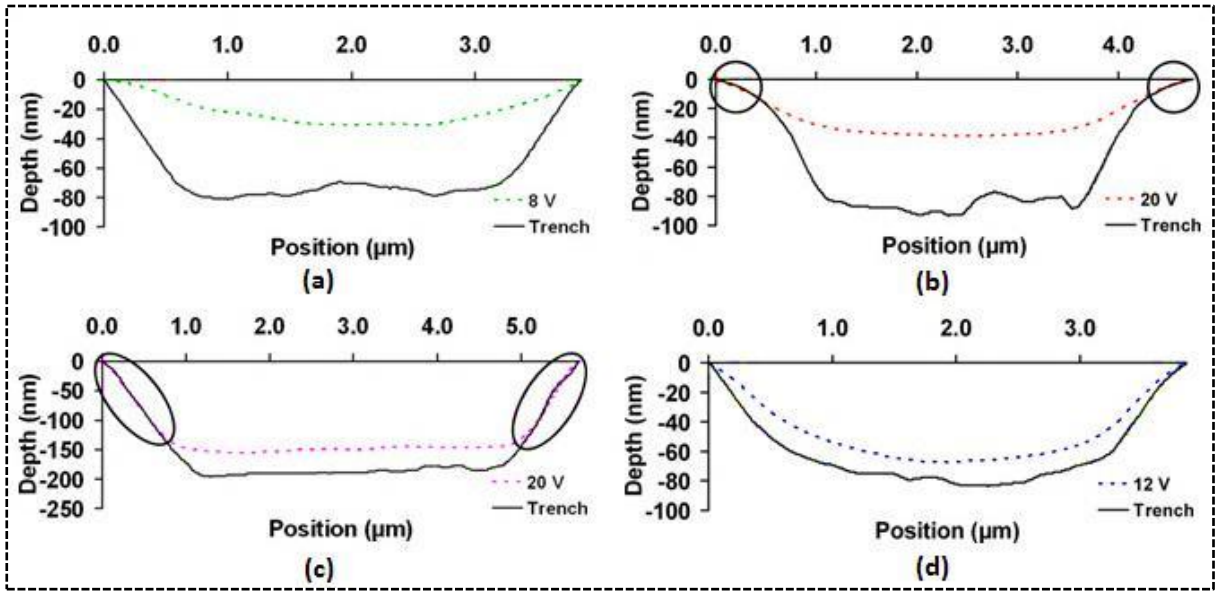

Figure 4-10: Cross-sectional profile of the underlying trenches overlaid with the deflection mode shape of the graphene layer of (a) Device 1 (actuated at V_S = 8 V), (b) Device 2 (actuated at V_S = 20 V), (c) Device 3 (actuated at V_S = 20 V) and (d) Device 4 (actuated at V_S = 12 V). The overlapping portions of the graphene and trench profiles are circled in (b) and (c).

It is likely that the graphene is sticking to the sidewalls of the trenches at these regions, hence altering the mode shape and peak deflection induced by the applied V_S. No overlapping was observed for Device 1 and 4. The electrostatic force magnitudes and analytical deflections of Device 2 and 3 were re-calculated using a reduced diameter of 3.85 μm and 4.22 μm (the diameter of the graphene layer that was not sticking to the sidewalls) respectively and the resultant analytical and experimental data is plotted in Figure 4-11. It can be observed that the theoretical and experimental data are now in better agreement, although the experimental measurements are still slightly lower. The sidewall sticking is likely to induce some tensile stress on the graphene sheet by stretching the sheet in lateral direction. The presence of this tensile stress, in effect, makes the graphene layer stiffer since the downward electrostatic force now has to overcome both the tensile stress and the mechanical restoring force of the layer in order to bend it. Hence, the possible presence of the tensile force makes the experimentally measured values still lower than the newly derived analytical deflections.

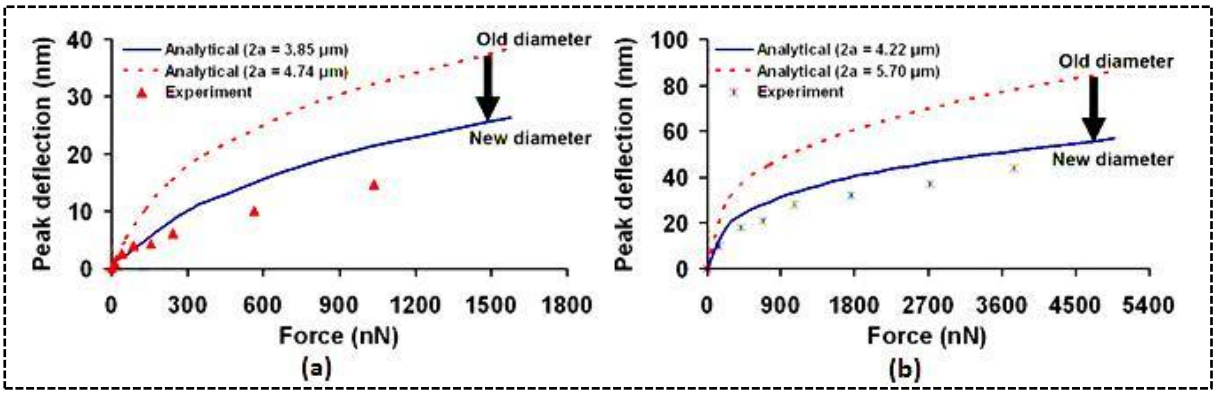

Figure 4-11: Analytically calculated deflections for (a) Device 2 and (b) Device 3 using reduced diameters 2a of 3.85 μm and 4.22 μm (the diameter of the graphene layer that was not sticking to the sidewalls) respectively.

The newly derived force-deflection relationships are in better agreement with the experimental measurements. With this understanding of the mechanical performance of our drum structures, their potential applications are discussed in the following section.

4.5 Potential Application for Graphene Drum Structures

A nanomechanical drum structure of this nature can find prospective applications as resonators or mass sensors. It is possible to actuate our graphene drums as resonator devices by adding a sinusoidal voltage to the DC bias applied to the back gate. The resonance frequency f_0 can be estimated by the Equation (4.19) [83],

$$f_0 = \frac{0.469}{a^2}\sqrt{\frac{Eh^2}{\rho(1-\nu^2)}} \tag{4.19}$$

where E is the Young's modulus, ν is the Poisson's ratio of graphene, m is the mass and h and a are the thickness and radius of the drum structure respectively.

The remarkable stiffness of graphene (Young's modulus of ~1 TPa) allows for extraordinarily small structures while maintaining high operating frequencies, highlighting its exciting potential as a material for next generation NEMS devices. Resonant mass sensing appears to be a very promising avenue for development as the small size and high operating

frequencies of graphene devices allow for significant improvement in sensitivity over silicon-based devices.

Resonant mass sensors work based on the principle of induced frequency shift when the overall mass of the sensor changes [73][84][85]. Assuming that the spring constant of the drum does not change significantly when the structure is mass loaded, the sensitivity of a drum-based mass sensor can be estimated by [73],

$$\left|\frac{\partial m}{\partial f}\right| = \frac{2m}{f_0} \tag{4.20}$$

where f_0 is the resonance frequency of the unloaded sensor. Table 4-3 summarizes the analytical (calculated using Equation (4.1)) and FEM simulated (using ANSYS) resonance properties of Device 1 and 4. Their potential mass sensitivities are also derived using Equation (4.20). Device 2 and 3 are omitted from the discussion as the presence of trench sidewall sticking is likely to have adverse implications on their resonance performance.

Table 4-3: Theoretical resonance characteristics and mass sensitivities of the graphene drum structures

Label	Mass, m (g)	Analytical f_0 (MHz)	Simulated f_0 (MHz)	Mass sensitivity (g Hz^{-1})
Device 1	3.08 x 10^{-13}	33.4	33.8	1.84 x 10^{-20}
Device 4	2.60 x 10^{-13}	26.9	27.2	1.93 x 10^{-20}

A mass sensor based on our graphene drum structure is, in theory, able to achieve mass sensitivities in the 10^{-20} g Hz^{-1} range. This sensitivity can be further improved by reducing the structure dimensions which would lower the mass of the drum and increase its f_0. This is a two order of magnitude improvement over silicon-based structures which have managed 10^{-18} – 10^{-12} g Hz^{-1} resolution [73][84][85]. Sensors have also been developed with carbon

allotropes such as fullerenes and CNTs. Additional modeling with graphene in nano-cantilever mode had been performed and the modeling results have been compared with single wall (SW) CNT-based resonators of similar dimensions. Summary of the results are shown in Table 4-4.

Table 4-4: Theoretical resonance characteristics and mass sensitivities of the graphene nano-cantilever and CNT structures

Label	Dimensions	Frequency (MHz)	Mass (g)	Mass Sensitivity (g/Hz)
SWCNT	Length, L = 3 μm Diameter, D = 1 nm	$f_0 = \frac{{B_0}^2 D}{8\pi L^2}\sqrt{\frac{E}{\rho}}$ [86] f_0= 0.43 B_0 = 1.875 E = 1 TPa; ρ = 1300 kg/m^3	3.06×10^{-18}	7.12×10^{-24}
Graphene Nanocantilever	Length, L = 3 μm; Width, w = 1 nm; Thickness, t = 0.335 nm	$f_0 = \frac{1}{2\pi}\sqrt{\frac{8EI}{\rho AL^4}}$ [83] f_0= 0.100 $I = (wd^3)/12$, E = 1 TPa, ρ = 2300 Kg/m^3	2.34×10^{-18}	2.34×10^{-23}

Though the numerical mass sensitivity values suggest, CNT's have better mass sensitivity than the graphene nano-cantilever of similar dimensions, graphene has other additional advantages. Graphene being a 2D flat sheet possesses larger surface area which allows for more contact with the added molecules or materials. Secondly, the graphene interface with other materials is found to be strong when compared to CNT's link to materials. The ultimate tensile strength of SWCNTs is 13 – 53 GPa, whereas graphene has a tensile strength of ~130 GPa which allows for better stress handling capabilities. Moreover, the mass sensitivity can be enhanced by varying the dimensions and designs of graphene based resonators. Sakhaee-Pour et al. demonstrated that a single layer of graphene is highly sensitive to an added mass of the order of 10^{-6} fg through molecular structural mechanics simulations [86]. Researchers from Columbia university reported graphene as a highly sensitive mass sensor (sensitive to around 1 zeptogram which is about 10^{-21} g) [71]. Zeptogram sensing from gigahertz

vibrations of single layer cantilever based nanosensor have also been reported [87]. Mass sensitivities of 10^{-24} g (yoctogram) have been reported for graphene based nanoribbon resonator through molecular dynamic simulation studies [88]. As the size of the sample decreases, determining the mass is prone to difficulties. Therefore, resolving mass of nanoparticles or single molecules need extremely high sensitive material. Graphene has an extra bonus of being a 2D material and a low electronic noise material, thus enabling ultra-sensitive and ultra-fast sensors based on graphene. It also allows for various design variations by simply carving the material and thus the properties of the designed resonators can be controlled which is demonstrated in Chapter 8 of the thesis.

4.6 Conclusions

The mechanical characterization of a nanomechanical graphene drum structure for NEMS devices was presented in this chapter. Drums of diameters 3.8–5.7 μm were fabricated with thicknesses ranging from 8 to 15 nm. The devices were actuated and measured for their electrostatic deflection using AFM. From the deflection measurements, the structures were found to have linear spring constants ranging from 3.24 to 37.4 N m^{-1} and could be actuated to about 18–34% of their thickness before displaying nonlinear deflection. An analytical framework, based on large deflection of circular plates, was also formulated to model the deflection behaviour. Finite element simulations were carried out, using ANSYS, to reinforce the analytical model. For two of the drum structures, the peak deflections and deflection mode shapes are in good agreement with analytical calculated values and FEM simulations. The experimental data agree well with analytical and finite element models using Young's modulus of 1 TPa. The resonance characteristics of the devices were then derived by both plate theory and FEM simulations. It was found that the drum structures can vibrate at frequencies in excess of 25 MHz. The small size and high theoretical operating frequencies of our graphene structures make them very promising for resonant mass sensing applications.

Sensitivities of up to 10^{-20} g Hz^{-1} can potentially be achieved. This is a two order of magnitude improvement over proposed silicon structures which have managed 10^{-18}–10^{-12} g Hz^{-1} resolution.

The test method adopted for extracting the mechanical properties of graphene in this chapter pose certain limitations. During the characterization, when the actuation voltages (electrostatic forces) get larger, imaging graphene through AFM becomes difficult due to image distortion and extraction of the actual membrane deflection gets tedious. In order to overcome this experimental difficulty, in the following chapter, a technique using AFM as a nanoindenter is proposed to precisely extract the mechanical properties of suspended graphene (monolayer and few-layer) devices. This technique also eliminates the need for an electrode to apply forces and the structures can be actuated through point contact mechanical perturbation.

CHAPTER 5 : MECHANICAL BEHAVIOUR OF GRAPHENE: AN AFM NANOINDENTATION STUDY

5.1 Introduction

In recent years, extensive research has been done to extract the electronic properties of graphene devices by making structures like single molecule gas detectors [90], transistors [14][91], p-n junctions [92], nanoribbons [93][94], quantum dot [95], nanoconstrictions [96], optical modulators [97], transparent conducting electrodes in organic light emitting diodes and light-emitting electrochemical cell [98][56] and spin valve devices [99]. However, the mechanical properties of suspended graphene have not been studied systematically to date although the possibility of making suspended graphene structures as nanomechanical devices have been demonstrated. Dynamic measurement studies have shown that mono/few layer suspended graphene sheets can be operated as nanoelectromechanical resonators [69]–[72][100]. Linear and nonlinear mechanical properties of graphene (8 nm to 15 nm) have been measured by electrostatic actuation and sensing through AFM (see Chapter 4) [101]. Static deflection measurements have also been made using AFM nanoindentation to extract the stiffness of multilayer graphene (2 – 8 nm) [79]. Similar test method has been adopted to determine the nonlinear elastic properties, and intrinsic strength of graphene [80]; bending rigidity and tension [70] of suspended graphene structures. Atomic resolution images of suspended graphene membranes and deflection of the freestanding membranes from their initial equilibrium height have been achieved using scanning tunneling microscopy (STM) [102][103]. Theoretical and computational studies on graphene have also been explored. Linear and nonlinear mechanics of graphene sheets have been extracted using various techniques like atomistic, continuum and hybrid approaches [74]–[77]. However, the influence of layer number (thickness of graphene) and anchor geometry on the mechanical properties of graphene based nanomechanical devices have not been widely explored so far. Therefore, this chapter aims to address this in detail.

The characterization technique adopted in this chapter is AFM nanoindentation. This method eliminates the difficulties and inaccuracies that arise from the electrostatic actuation and sensing through AFM imaging used in the previous chapter. This method is more straightforward and can be incorporated on devices without electrodes. Hence hereafter in all the following chapters this technique has be used to precisely extract the mechanical properties. Moreover, this method can be extended to study the mechanical properties of other nanomaterials and to demonstrate such a capability, MoS_2 which is also a 2D layered structure has been characterized and the results obtained are also shown in this chapter.

5.2 Device Characterization

The optical micrograph of a pristine sample is shown in Figure 5-1 from which a clear contrast between regions of different graphene thicknesses can be observed. The exact thickness of the graphene was confirmed using Raman spectroscopy which will be discussed in detail in the following sub-section.

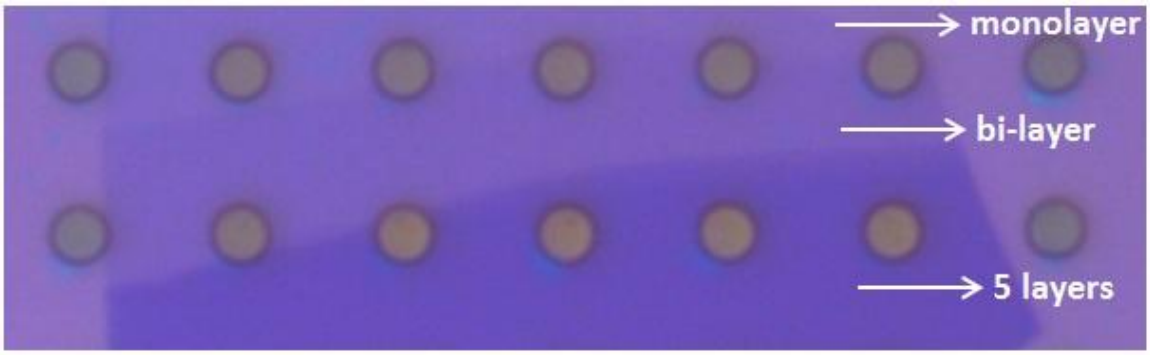

Figure 5-1: Optical microscopy image showing suspended graphene with different thicknesses over pre-patterned substrate.

5.2.1 AFM

After identifying the presence of graphene on the pre-patterned substrate, an AFM tapping mode image was obtained to confirm the suspension of graphene over circular trenches. An AFM silicon cantilever of ~74 KHz resonance frequency (FESP7 Veeco probe) was used to obtain the topographical image in ambient conditions. All the images were obtained from

JEOL JSPM 5200. An AFM topographic image of a monolayer suspended graphene is shown in Figure 5-2. In this study Raman spectroscopy has also been used to confirm the thickness of graphene.

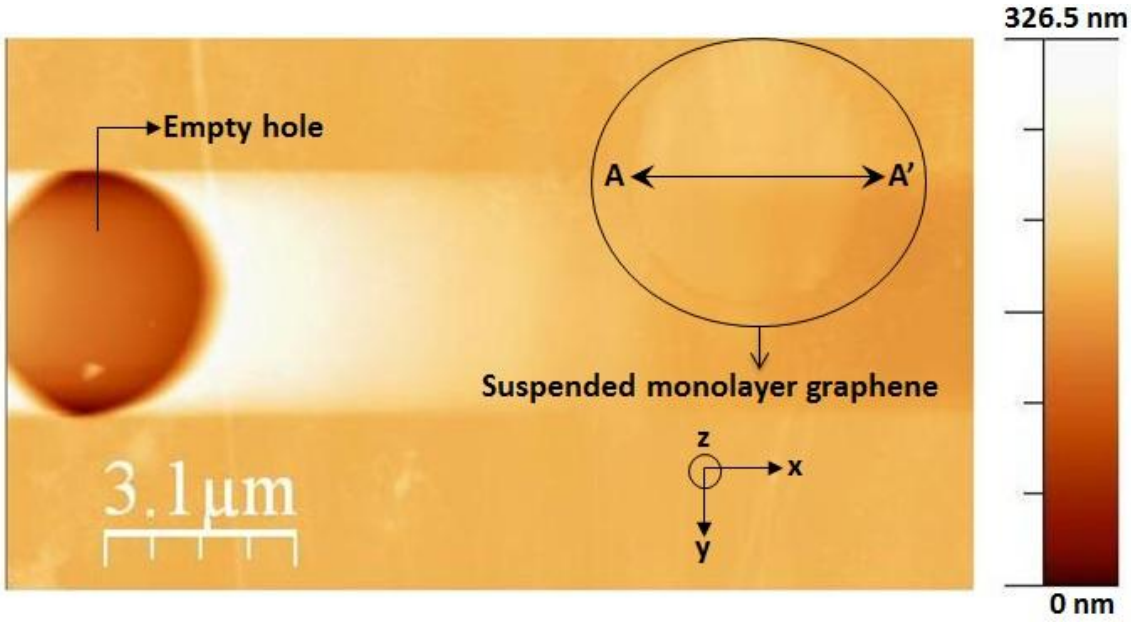

Figure 5-2: AFM topographical image of a suspended monolayer graphene (Device 1). The colour contrast in the micrograph is representative of the topographical data at each region (refer to height scale). The suspended graphene device (diameter – AA') is located at the right.

5.2.2 Raman Spectroscopy

Raman spectroscopy has proved to be the most reliable non-destructive method to determine the thickness of graphene [104][105][64]. It is also a widely used tool to probe the lattice defects and amount of charged impurities in graphene [106][107]. Moreover, the Raman spectrum also provides insights to the intrinsic characteristics of graphene. Visible Raman spectroscopy was carried out at room temperature using Renishaw Invia Raman system. The excitation wavelength used was 532 nm and the laser power at the sample was below 1.0 mW/cm^2. The above power density has been chosen to avoid laser induced lattice damage of graphene [108]. A 100X objective lens was used with a laser spot size of ~1 µm and the scattered light from the sample was collected in the back scattering geometry. The Raman spectrum was analysed by curve fitting using multiple Lorentzians with a slopping background. Typical Raman spectra of a single layer (Device 1) and five layer graphene

(Device 4) on SiO_2 (285 nm)/Si substrate obtained after indentation is shown in Figure 5-3(a) and Figure 5-3(b) respectively.

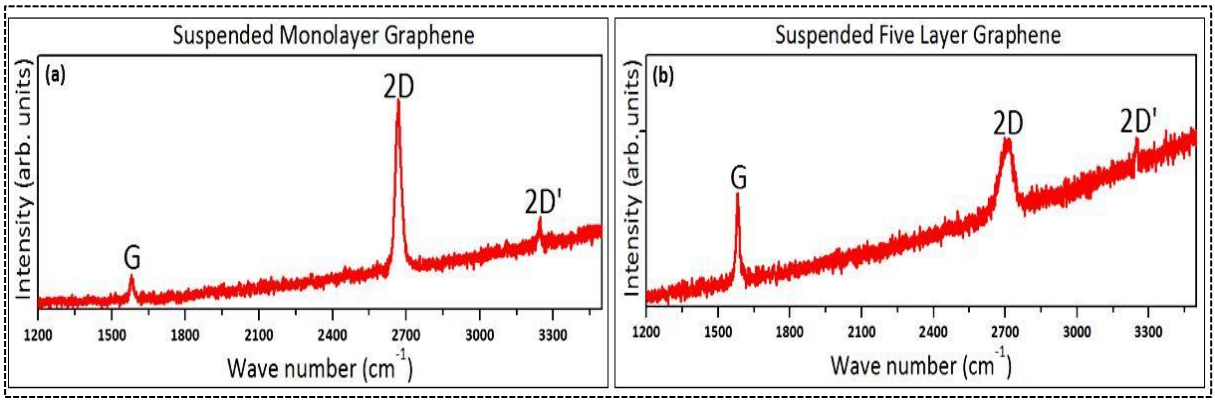

Figure 5-3: Raman spectra of a suspended monolayer graphene obtained after indentation (a) Device 1 (b) Device 2.

From Figure 5-3 it is clear that the D peak is inactive, and thus the graphene used in our experiments can be considered to have good crystalline quality. The very intense 2D (~2700 cm^{-1}) and 2D' (~3240 cm^{-1}) bands of each sample further confirmed that the graphene possess very good sp^2 hybridized crystalline quality. The relative intensity and shape of the G and 2D Raman peaks change with respect to number of graphene layers [64][104][109]. For visible excitation the G and 2D Raman peaks appear around 1580 cm^{-1} and 2700 cm^{-1} respectively. It is very obvious from figures Figure 5-3(a) and Figure 5-3(b) that the intensity of the G band increases relative to 2D band as graphene thickness increases. A monolayer graphene is identified by a sharp and symmetric 2D band peak. The 2D peak becomes broader as the layer number increases due to induced multiple double resonant scattering pathways. The full width at half maximum (FWHM) of the 2D peaks is estimated to be 24 cm^{-1} and 65 cm^{-1} in Figure 5-3(a) and Figure 5-3(b) respectively, which corresponds to monolayer and 5 layer graphene.

5.2.3 AFM Force-Distance Curves

The mechanical properties of graphene devices were obtained from AFM force curve measurements. First, a force distance curve was acquired on clean hard silicon substrate. This

curve was used as a reference for all calculations. A typical force curve obtained on a silicon substrate is shown in Figure 5-4. From the force curve, only the contact portion of the attract curve is used for the analysis which start from zero level force. All measurements were carried out in ambient conditions.

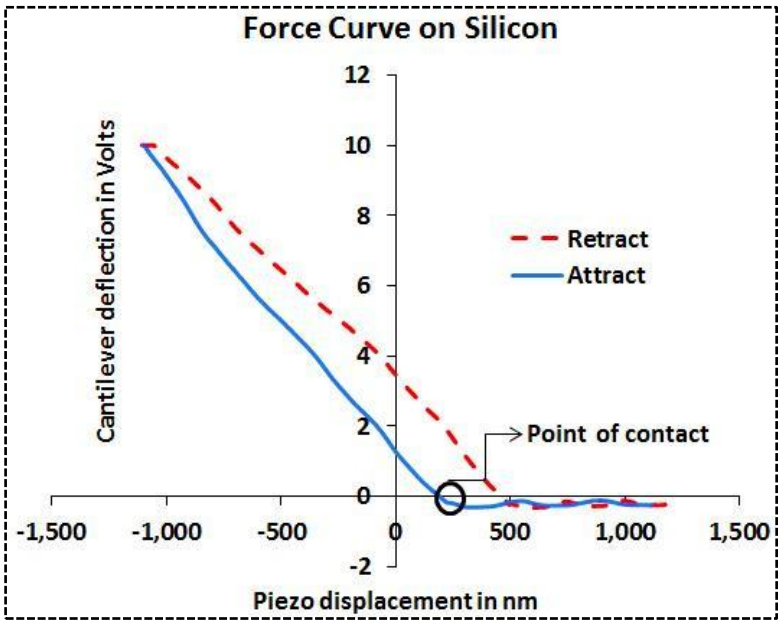

Figure 5-4: A typical F-Z curve obtained from a clean silicon substrate.

The inverse slope of the contact portion of the attract curve yields the deflection sensitivity of the cantilever. The cantilever deflection (nm) is obtained by [110],

$$d_{cantilever}\,(\text{nm}) = D \times d_{cantilever}\,(\text{Volts}) \tag{5.1}$$

where D is the deflection sensitivity of the cantilever (nm/V).

The force applied is related to the cantilever deflection by,

$$F = k_c \times d_{cantilever} \tag{5.2}$$

where k_c is the spring constant of the cantilever.

An AFM Silicon cantilever of ~74 KHz resonance frequency (FESP7 Veeco probe) was used for all the measurements shown in this this section. The frequency of the cantilever was obtained using the AFM in tapping mode. This value agrees well with the specifications provided by the manufacturer (75 KHz with a nominal spring constant of 2.8 N/m).

A topographic image of the suspended graphene was acquired using the AFM in non-contact mode. The probe tip was then moved to the center of the suspended graphene where the loads were subsequently applied. The deflection of the graphene device (δ) was then obtained from the following relationship [110].

$$\delta = Z_{piezo} - d_{cantilever} \tag{5.3}$$

where δ is the deflection of graphene, Z_{piezo} is the piezo displacement and $d_{cantilever}$ is the cantilever deflection.

The schematic of attract curves of a hard silicon substrate and graphene is shown in Figure 5-5(a). The δ–Z curve is then converted to F-d curve as shown in Figure 5-5(b). By subtracting the two curves, the final force versus deflection plot of graphene was thus obtained as shown in Figure 5-5(c).

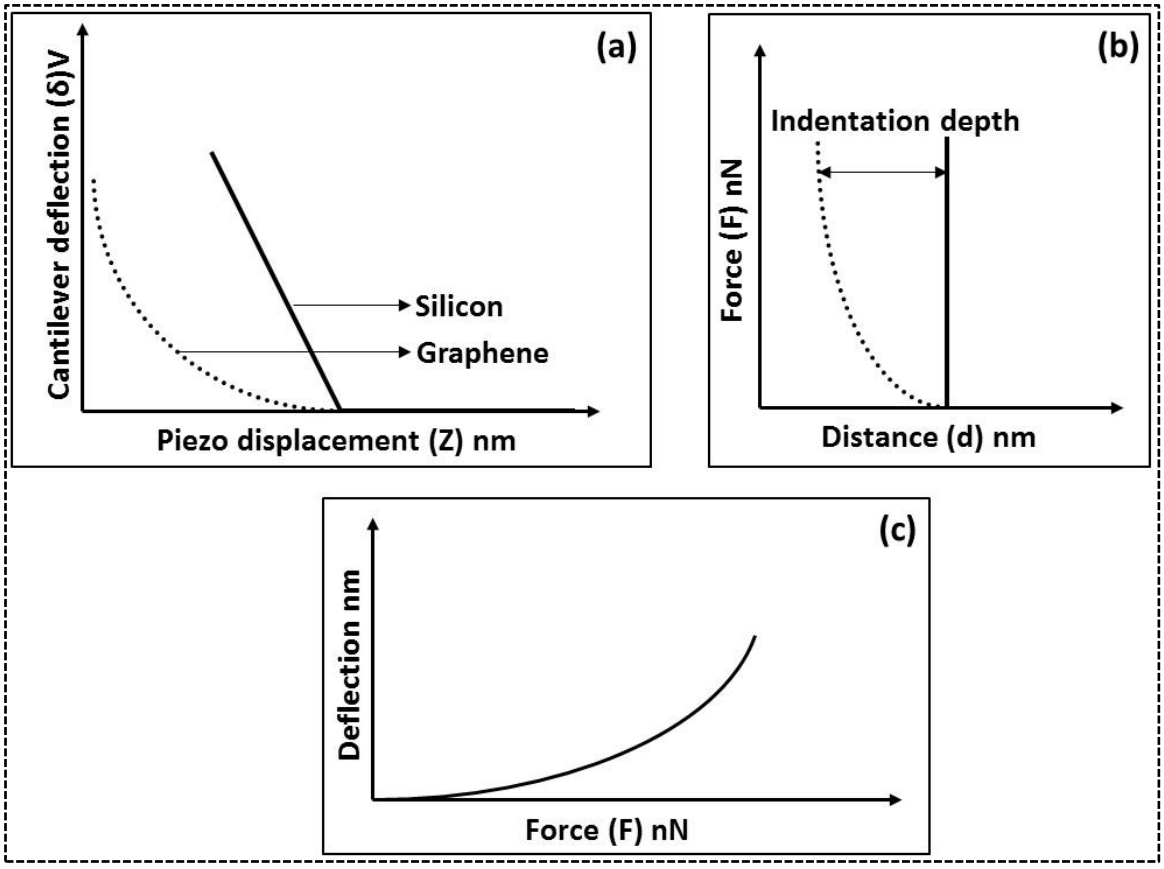

Figure 5-5: (a) A typical schematic force curve of a clean silicon substrate and suspended graphene. (b) Converted and resampled F-d curve. (c) Final force versus deflection of graphene.

5.2.3.1 Extraction of Elastic and Nonlinear Properties of Graphene Nanomechanical Devices

Force versus deflection curves were obtained for graphene devices with different thicknesses ranging from 3.35 Å to 16.75 Å (monolayer to 5 layers) [104]. All the curves exhibit nonlinear deflection behaviour which is similar to membrane behaviour. In this case, the deflection of the membrane does not linearly increase with increase in force due to stretching of the membrane and stress stiffening effects [82]. By modelling the deflection behaviour of graphene device based on continuum mechanics, the relationship between graphene deflection and the point force which is applied to the center of the device structure is obtained as indicated in Equation (5.4) [82][111]. As the radius of the AFM probe tip used for the experiments is 8±2 nm, which is much smaller than the lateral diameter of the graphene device which is ~3.8 μm, the forces applied can be assumed to be point loads.

$$F = \left(\frac{4\pi E h^3}{3(1-\upsilon^2)a^2} + \pi T \right)\delta + \left(\frac{q^3 E h}{a^2} \right)\delta^3 \tag{5.4}$$

where F is the point force applied to the center of the device structure, E is the Young's modulus of graphene, T is the pre-tension in the device structure, υ is the Poisson's ratio of graphene, a is the radius of the graphene, h is the thickness of the graphene and q is given by,

$$q = \frac{1}{(1.05 - 0.15\upsilon - 0.16\upsilon^2)} \tag{5.5}$$

where υ = 0.16 is the Poisson's ratio of graphene [111].

The linear term in the Equation (5.4) corresponds to the bending rigidity and stretching of the graphene. The cubical term corresponds to the stress stiffening effects and thus makes the force (F) versus deflection (δ) curve nonlinear. The Young's modulus and pre-tension of the device can be obtained by fitting the force versus deflection curve to Equation (5.4) [82][111].

The mechanical properties that can be extracted from the force versus deflection curve include linear and nonlinear spring constants. The equation that describes the nonlinear static deflection of graphene devices is

$$F = -k_1\delta - k_3\delta^3 \tag{5.6}$$

where F is the applied force, k_1 is the linear spring constant and k_3 is the nonlinear spring constant.

The Equation (5.6) can be directly related to Equation (5.4) and thus the analytical linear and nonlinear spring constant obtained are

$$k_1 = \left(\frac{4.3Eh^3}{a^2}\right) + \pi T \quad \text{and} \quad k_3 = \left(\frac{1.06Eh}{a^2}\right) \tag{5.7}$$

For an atomically thin graphene layer, the thickness (h) is negligible and the E term in Equation (5.7) represents the 2D elastic modulus.

The following section highlights the experimental results obtained from graphene devices. Measurement results from five different graphene devices with thickness ranging from 1 to 5 atomic layers are shown. Results from monolayer graphene device with partially anchored geometry have also been discussed.

5.3 Results and Discussion

High resolution AFM images were obtained in the region of interest and the probe tip was then moved to the center of the device structure. Subsequently the probe tip was pushed down by applying loads to the AFM cantilever and the corresponding force curves were obtained. A three dimensional image of a suspended graphene device and the corresponding force curve obtained on one of the device are shown in Figure 5-6 and Figure 5-7 respectively.

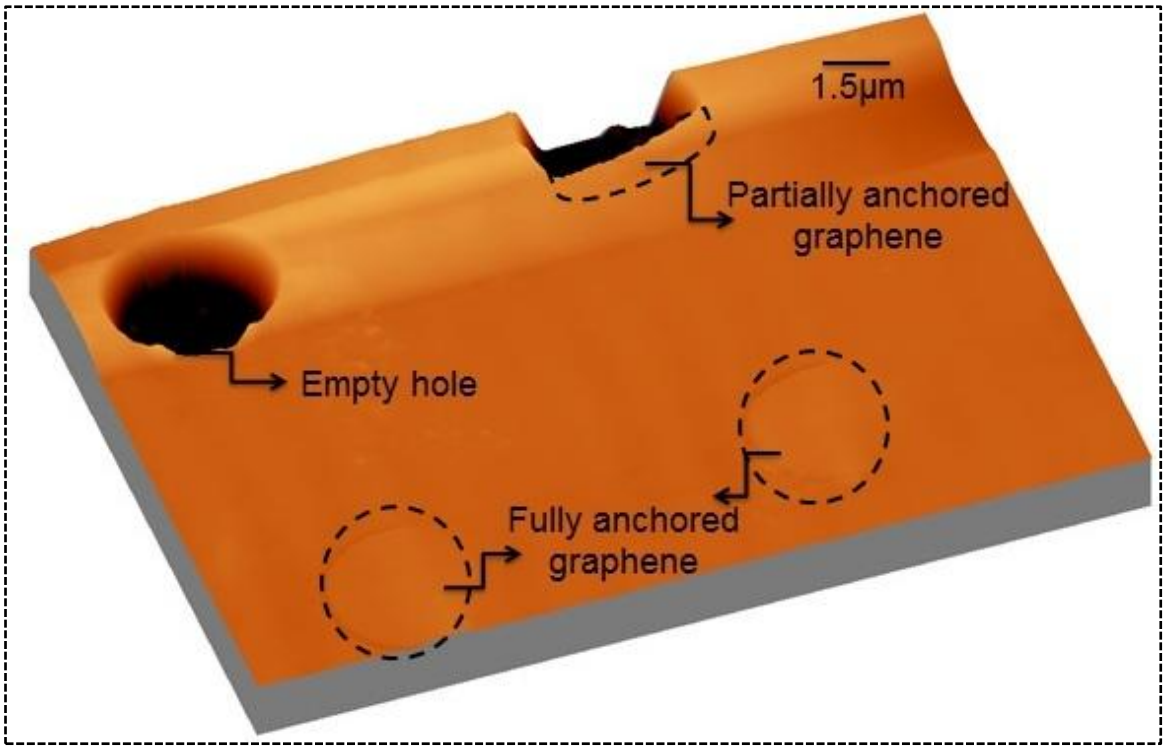

Figure 5-6: An AFM 3D topographic image showing an empty hole and suspended graphene with fully and partially anchored geometry.

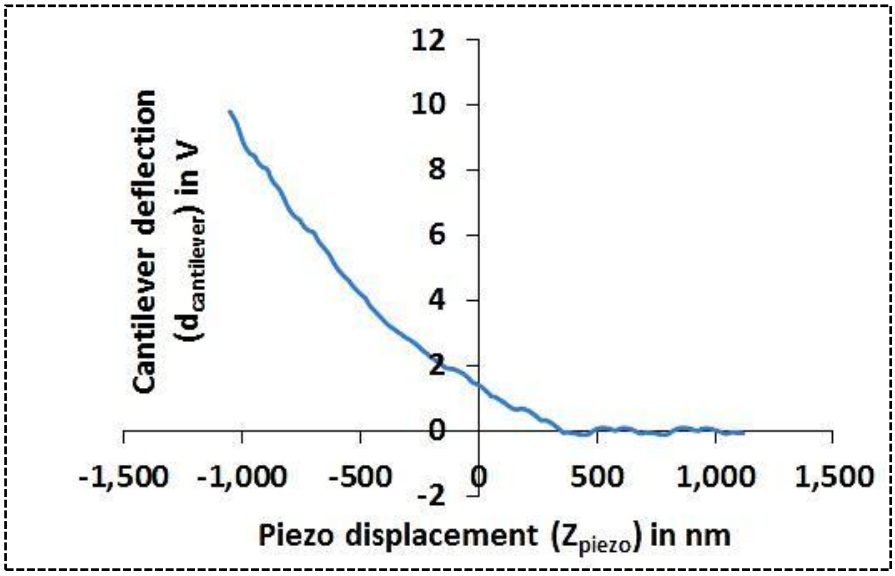

Figure 5-7: A typical attract portion of the force curve obtained from a fully anchored monolayer graphene device (Device 1).

Force versus deflection characteristics of five graphene devices are highlighted in this section. The dimensional characteristics of the five devices are shown in Table 5-1.

Table 5-1: Summary of dimensional characteristics of the graphene devices

Label	Dimensions		Number of graphene layers	Anchor geometry
	Diameter 2a (μm)	Thickness, *t* (nm)		
Device 1	3.76	.335	1	Fully anchored
Device 2	3.76	.67	2	Fully anchored
Device 3	3.8	1.005	3	Fully anchored
Device 4	3.8	1.675	5	Fully anchored
Device 5	3.25	.335	1	Partially anchored

AFM nanoindentation measurements on the five devices yielded the static deflection characteristics. The force versus deflection curves obtained for the five devices is shown in Figure 5-8. The experimental force versus deflection curves were fitted using Equation (5.6) for devices with fully anchored geometry and are shown with a red solid line in Figure 5-8(a) – (d).

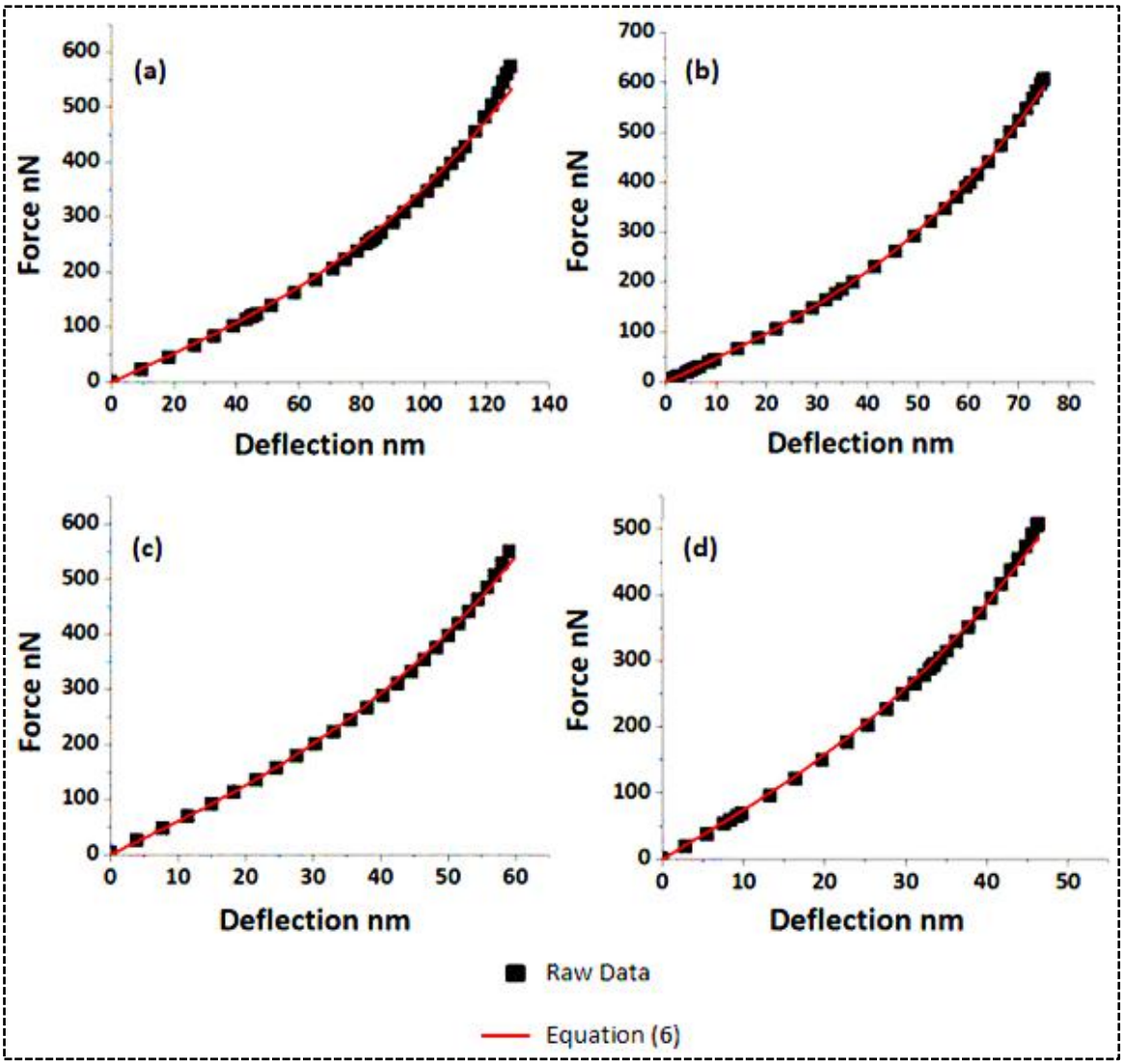

Figure 5-8: Experimental force versus deflection traces obtained for (a) Device 1, (b) Device 2, (c) Device 3 and (d) Device 4. All curves were obtained by adopting the method described in Section 5.2.3. The fitted curves (red solid line) were obtained using Equation (5.6) from Section 5.2.3.1.

From the AFM nanoindentation force versus deflection curves, we were able to extract the linear and nonlinear spring constants of the devices. The F-d traces were fitted using Equation (5.6) to obtain the linear and nonlinear spring constants of the devices. The relation of stiffness of the devices with respect to its thickness (number of graphene layers) is shown in Figure 5-9(a) and Figure 5-9(b) respectively.

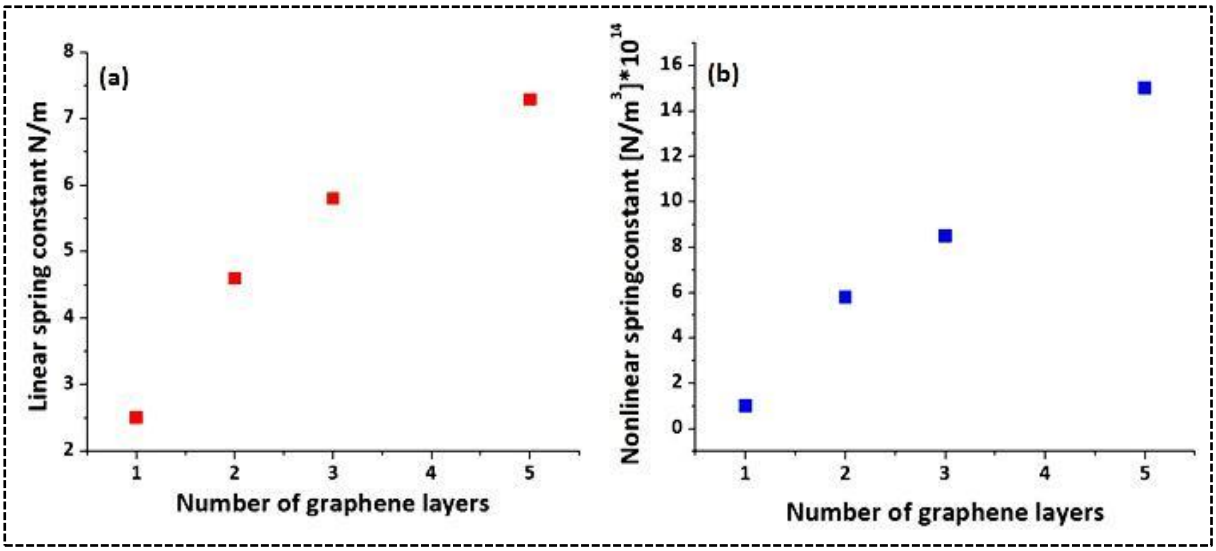

Figure 5-9: Graphene layer dependent (a) linear spring constant and (b) nonlinear spring constant.

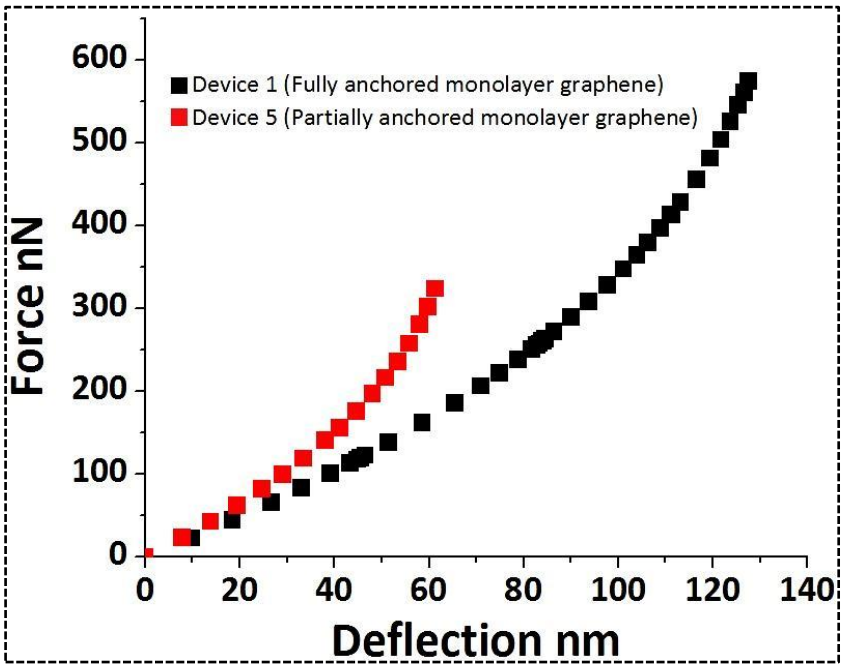

Figure 5-10: Experimental force versus deflection traces obtained for fully anchored monolayer graphene (Device 1) and partially anchored monolayer graphene (Device 5).

From the experimental results as shown in Figure 5-8, Figure 5-9 and Figure 5-10 it is very clear that the stiffness of the structure is dependent on its dimensions and anchor geometry. A monolayer graphene which is fully anchored along its periphery exhibits low stiffness compared to same thickness graphene which is partially clamped with lower lateral dimensions. Hence by varying the anchor geometry we are able to obtain structures of varying stiffness which would operate at different frequencies. This provides a

straightforward means by which resonators of varying frequencies can be designed. The possibility of using helium ion microscope to pattern the devices structures and thus providing a means to easily vary device frequencies have been discussed in detail in Chapter 8.

Moreover, from the k_1 and k_3 values obtained, the Young's modulus and pre-tension of graphene devices can be derived using Equation (5.7). The Young's modulus and the pre-tension of the devices are shown in Table 5-2. For Device 1 the deduced 2D elastic modulus is found to be 375 N/m which in good agreement with previous findings [9].

Table 5-2: Deduced Young's modulus and pre-tension of graphene devices

Label	Young's Modulus TPa	Pre-tension N/m
Device 1 (Monolayer)	1.12	0.79
Device 2 (Bilayer)	3.25	1.46
Device 3 (3 layers)	3.25	1.86
Device 4 (5 layers)	3.43	2.3

It is found that the pre-tension increases with increase in graphene thickness which is similar to the increasing trend observed for graphene with thickness greater than 2 nm [80]. The variation in Young's modulus and pre-tension is due to the different adhesion forces of the graphene to the substrate and the stacking faults in multilayer graphene. The van der Waals forces of attraction strongly influence the mechanical behaviour of monolayer and multilayer graphene. In a suspended monolayer graphene this force only influences the adhesion between graphene and the underlying SiO_2/Si substrate. On the other hand, in a multilayer graphene, it controls the graphene and substrate adhesion as well as the adhesion between graphene layers (inter layer coupling) [112][113]. The varying adhesion strength causes the

contact stiffness (clamping boundary condition) to be different for different graphene thicknesses. Hence when the static deflection curves are fitted to the same model, it yields a varying pre-tension and Young's modulus for different layers of graphene.

The various reported experimental and theoretical values of the Young's modulus of graphene range between 0.5 TPa to 6.88 TPa [79][114]–[121]. Most of the reported theoretical values were obtained based on a single sheet of graphene. The theoretical study of Young's modulus based on the number of graphene layers (1 – 5) show no significant change in the values [118]. This was because the boundary condition was assumed to be the same for mono and multi-layer graphene. But, in reality the clamping stiffness in the direction of thickness would greatly influence the mechanical properties of graphene based devices. It is also found that the size and chirality of graphene also influence the Poisson's ratio and Young's modulus of graphene [119]. In our experiments we find that the Young's modulus of a monolayer graphene is ~1.12 TPa. On the other hand, we find that few layer graphene exhibits a Young's modulus of ~3 TPa when the force versus deflection plots are fitted to the same model. Firstly, the change in boundary condition does vastly affect the Young's modulus of the graphene thus resulting in large variation in the deduced values [79]. The material properties in Equation (5.4) are very sensitive to any slight variation in the boundary conditions and hence can result in the variation of calculated Young's modulus for different graphene thicknesses [111][120]. Secondly, it is difficult to precisely predict or observe the clamping conditions of each device and hence it cannot be factored into the model. Hence we believe that the value of 1.12 TPa derived for monolayer graphene is the best estimate for Young's modulus.

After indentation measurements all devices were tested using Raman spectroscopy to check for any defects. It is found that after the devices were perturbed through indentation, there is

no significant defect formation and the quality of graphene is maintained. This proves that the graphene is robust, stiff and stable although it a 2D material [121].

5.4 Characterization of MoS_2

The characterization technique described in detail in this chapter to study the mechanical behaviour of graphene can be extended to study other nanomaterials. In order to show such capability, MoS_2 which is a layered semiconducting material has been explored through nanoindentation in the following sub-sections.

5.4.1 Overview on MoS_2

Atomically thin semiconducting MoS_2 is a layered structure and a transition metal dichalcogenide. It has recently drawn much interest due to its large intrinsic band gap (~1.8 eV) [122]. MoS_2 is found to exhibit room temperature mobility of 200 $cm^2 V^{-1} S^{-1}$ and on/off ratios of 1×10^8 [122]. Like graphene, the individual sheets of MoS_2 are held together by weak VdW forces and an individual sheet of MoS_2 consists of one molybdenum layer in between two layers of sulphur. The distance between two sheets of molybdenum is ~6.15 A° and the separation between molybdenum and sulphur sheets are ~1.59 A° with each MoS_2 sandwich layer measuring 0.65 nm [123]. Very thin layers of MOS_2 can be obtained through exfoliation which is very much similar to the exfoliation technique described to fabricate graphene (see Section 2.3.2). This 2D material was used as an industrial lubricant and a catalyst in petroleum refineries until the development of a MoS_2 transistor by Radisavljevic et al. in 2011 [122]. From then, it has been reported to have many applications like field effect transistors and logic gates to name a few [122][124].

5.4.2 Mechanical Properties of MoS_2

The suspended MoS_2 structures and the substrates that hold the MoS_2 sheets were prepared by adopting the same procedure as described in Section 3.1. An optical micrograph of a 3 layer and a 5 layer suspended MoS_2 is shown in Figure 5-11.

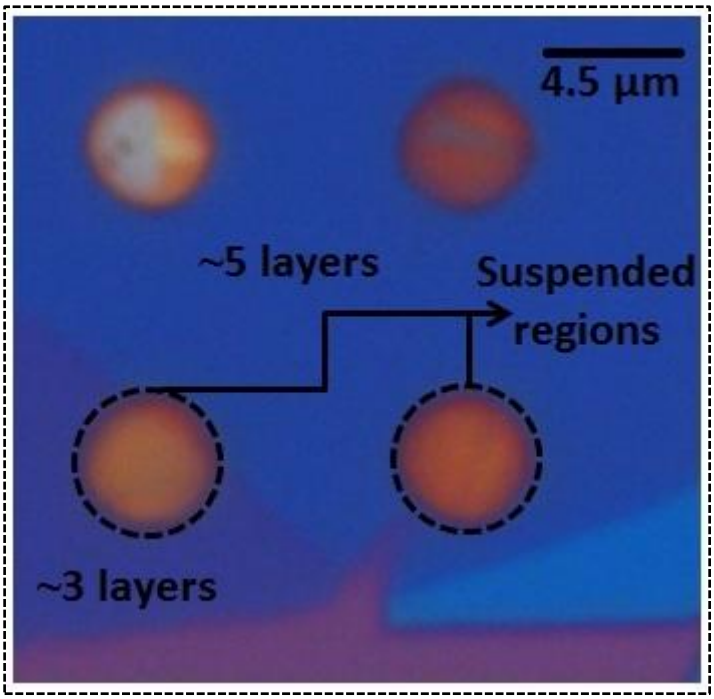

Figure 5-11: An optical micrograph showing a 3 layer and a 5 layer suspended MoS_2 on a SiO_2/Si substrate.

Nanoindentations were performed in ambient conditions with ~1.2 N/m stiffness cantilever on the suspended regions (~4.5 µm diameter) of MoS_2. The force curves obtained on a hard surface and a suspended 5 layer MoS_2 is shown in Figure 5-12 (a) and (b) respectively.

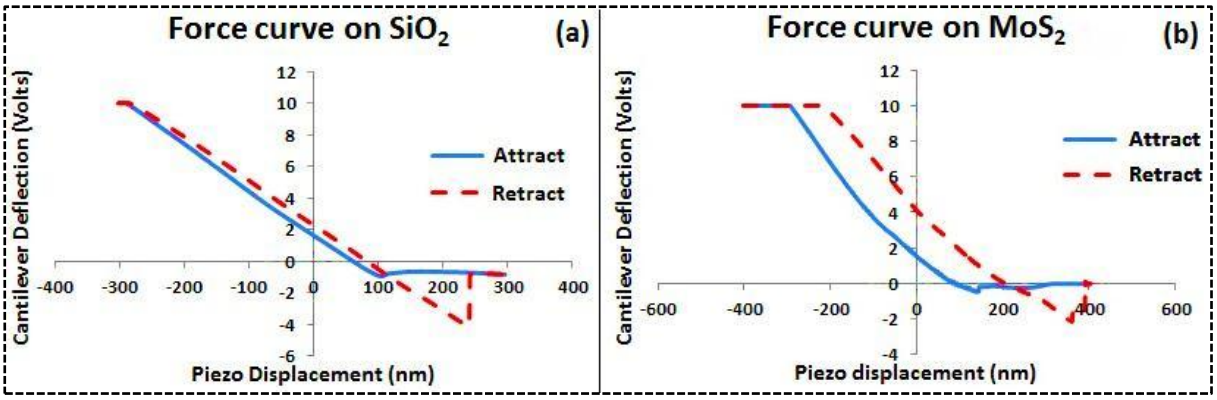

Figure 5-12: AFM force curves obtained on (a) SiO_2 surface (b) 5 layer suspended MoS_2

The mechanical properties of the devices were extracted by adopting the similar method used for suspended graphene structures. The Young's modulus and pre-tension of the MoS_2 were found to be 0.2–0.37 TPa and 0.15±0.09 N/m for 3, 5 and 8 layer MoS_2 samples which is in good agreement with the previous findings [125].

5.5 Conclusions

The nanoscale resolution of the AFM nanoindentation technique has enabled to obtain nonlinear static deflection characteristics of nanomechanical graphene structures of ~3.8 μm diameter and thickness ranging from 3.35 Å to 16.75 Å. Graphene devices whose periphery is fully anchored and partially anchored were also characterized and it was found that the mechanical properties of the devices are greatly influenced by the anchor geometry which provides a straightforward means to obtain devices with different fundamental vibrating frequencies. Linear and nonlinear spring constants varying from 2.5 N/m to 7.3 N/m and 1×10^{14} N/m^3 to 15×10^{14} N/m^3 were obtained for monolayer to five layers graphene devices. It is also found that a monolayer graphene exhibits a Young's modulus of 1.12 TPa and 2D elastic modulus of 375 N/m. The estimated pre-tension for the devices (0.79 N/m to 2.3 N/m) show an increasing trend with the increase in graphene thickness. Even after indentation the graphene devices were found to be defect free as shown by the absence of D peak in Raman spectrum. This study has thus enabled to understand the influence of layer number and anchor geometry on the mechanical properties of graphene devices. The low mass and high stiffness of graphene makes these devices as a good alternative for sensor applications (e.g. force, charge and mass sensors).

The characterization technique used to study graphene structures can be used to examine other nanomaterials and to demonstrate such capability, test structures containing suspended MoS_2 were also characterized by the AFM nanoindentation technique. Apart from extracting the mechanical properties of the test structures, this method can also be used to vary the surface morphology of the suspended graphene by inducing out-of-plane excitation which is demonstrated in the following chapter.

CHAPTER 6 : STUDY OF EXTRINSIC RIPPLE MORPHOLOGY OF GRAPHENE

6.1 Inroduction

The surface morphology of graphene is not perfectly planar and it is found to exhibit out-of-plane corrugations in the third dimension called “ripples/wrinkles” [19]. The reason for the presence of wrinkles is explained in Section 2.1. Ripples in graphene tend to vary the local atomic potential and hence influence the electronic properties [18]. These corrugations can affect the properties of graphene primarily by the formation of electron-hole puddles [126][127] and increasing the scattering rate [128][129]. It was also shown that ripples in graphene could enhance the spin-orbit coupling [130] and the spectroscopic measurements by Levi et al. revealed Landau levels in strained graphene nanobubbles without applying any external magnetic field [131].The above mentioned experimental report clearly demonstrates the presence of strain induced pseudo-magnetic fields in graphene [131]. Ripples in graphene are also reported to alter the chemical reactivity and hence can be utilized for regioselective chemical modification of graphene [132].

Ripples in graphene have been explored by various theoretical studies [133]–[139]. It is found that ripples could appear randomly across a suspended graphene sheet (intrinsic ripples) [19] and the ripple texture (orientation, wavelength and amplitude) can be controlled by manipulating the clamping conditions and making use of the negative thermal expansion coefficient of graphene [140]. It is also revealed that graphene is an electronic membrane and ripples can be introduced by changing the electro chemical potential [140]. It has been reported that the surface morphology of graphene can be changed under, applied uniaxial stress [141], in-plane shear [142] or strain [143], out-of-plane excitation [144]–[147] and thermal fluctuations [18]. The possibility of controlled tailoring of out-of-plane periodic

corrugations in graphene opens up a potential opportunity for making flexible nanoscale devices and electronics based on strain engineering [148]–[150].

Out-of-plane excitation is found to have a profound impact on the surface morphology of graphene [144]–[147]. This excitation technique can be effectively achieved through nanoindentation. Nanoindentation is a simple and widely employed tool to study the mechanical properties of materials under a point-contact perturbation as described in the previous chapter (See Chapter 5). The mechanical deformation of a 2D material during nanoindentation can subsequently modify its surface morphology by forming periodic ripples [144]–[146]. Theoretical studies on nanoindentation induced surface corrugations in graphene have been explored through molecular dynamics simulations and quasi-continuum method [144]–[146]. However, to date, there has been no experimental study on modifications in surface morphology of exfoliated suspended graphene after nanoindentation. In light of these theoretical reports, our experimental effort to control the local surface morphology of suspended graphene using nanoindentation and thermal engineering of the induced undulations would establish a novel route for the fabrication of flexible nanoelectronic devices.

In this chapter, the possibility of inducing surface corrugations and engineering the extrinsic ripples through temperature treatment in few-layer graphene using nanoindentation has been discussed in detail.

6.2 Experimental Details

The fabrication sequence (see Section 3.1) and the test method adopted to study the change in surface morphology of suspended graphene after mechanical deformation is illustrated in Figure 6-1. An optical micrograph of one of the fabricated suspended graphene structure is shown in Figure 6-2. Visible Raman spectroscopy (see Figure 6-3) and indentation (see

Figure 6-4) was carried out on the fabricated devices by following the procedure highlighted in Section 5.2. The FWHM of the 2D peaks in Figure 6-3(a–c) are 52, 64 and 67 cm^{-1} which corresponds to 2-, 4- and 5- layer graphene respectively [64][66].

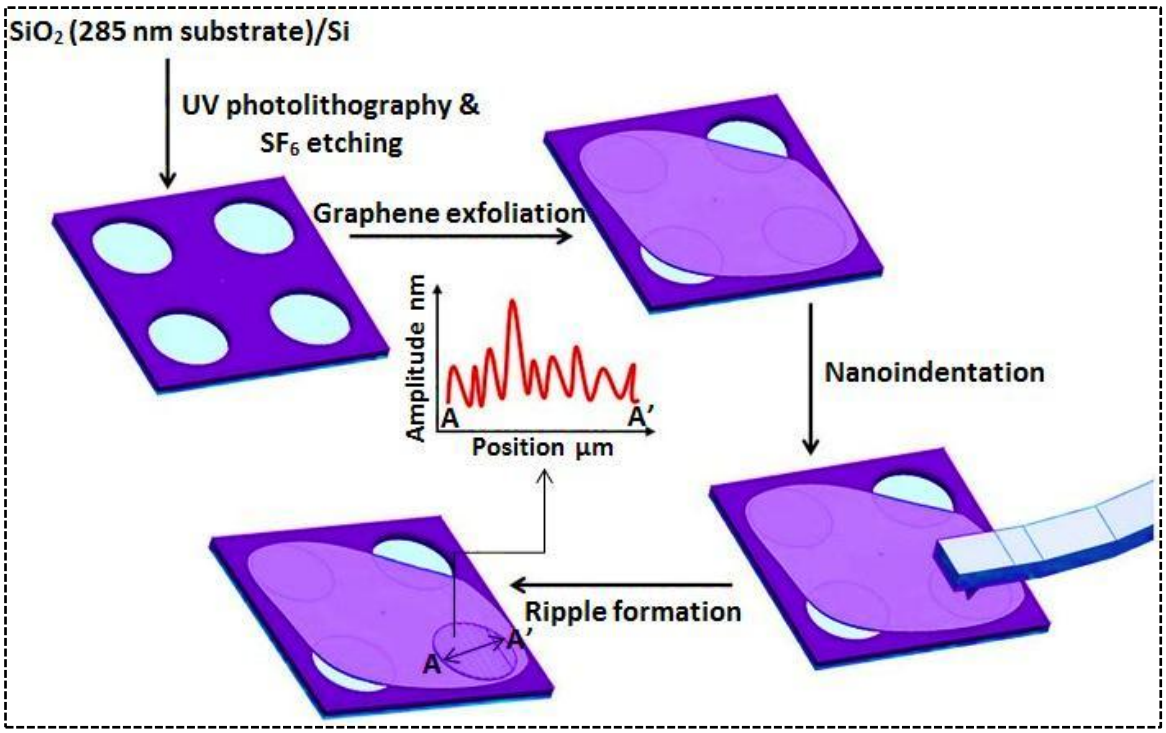

Figure 6-1: Fabrication sequence to obtain suspended graphene structures and test method adopted to study the surface morphology of graphene after mechanical deformation.

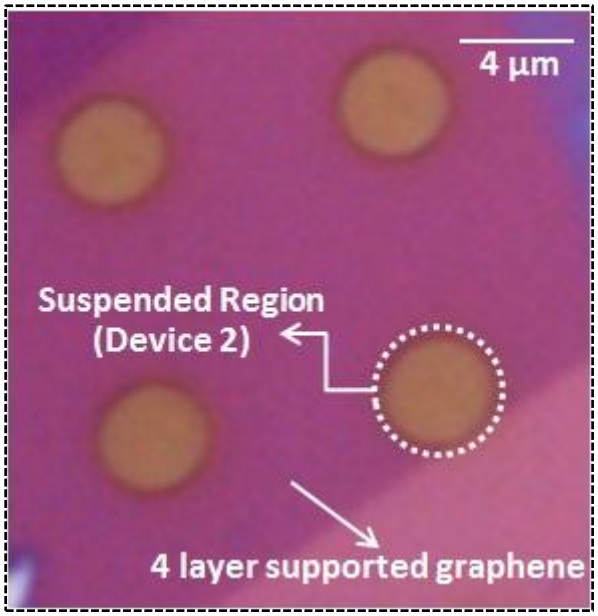

Figure 6-2: An optical microscopy image of a four layer supported and suspended graphene.

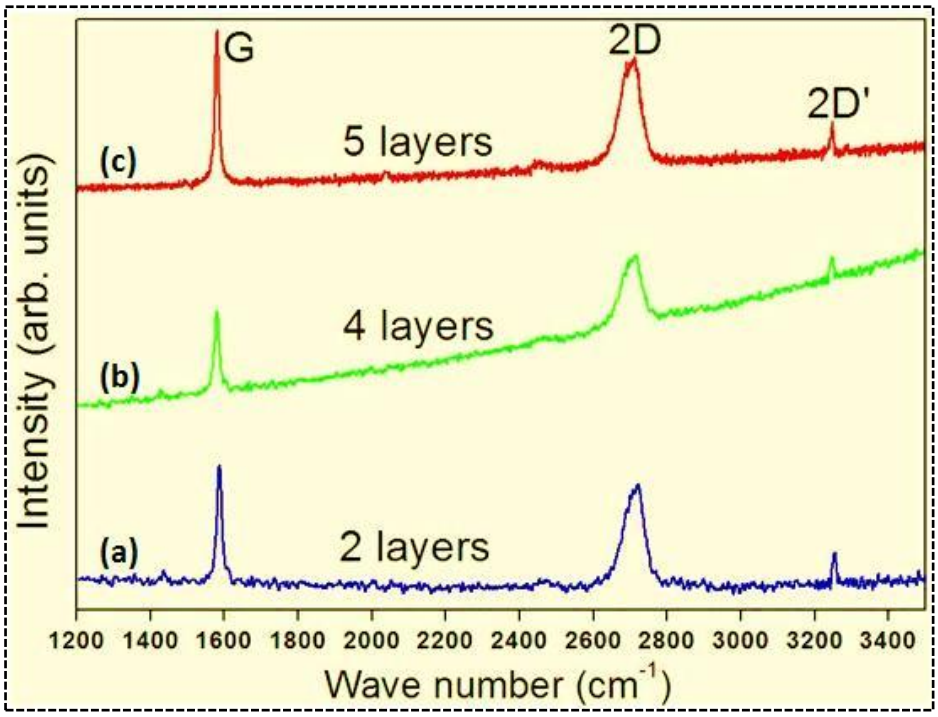

Figure 6-3: (a–c) Raman spectra of 2-, 4- and 5- layer suspended graphene structures respectively.

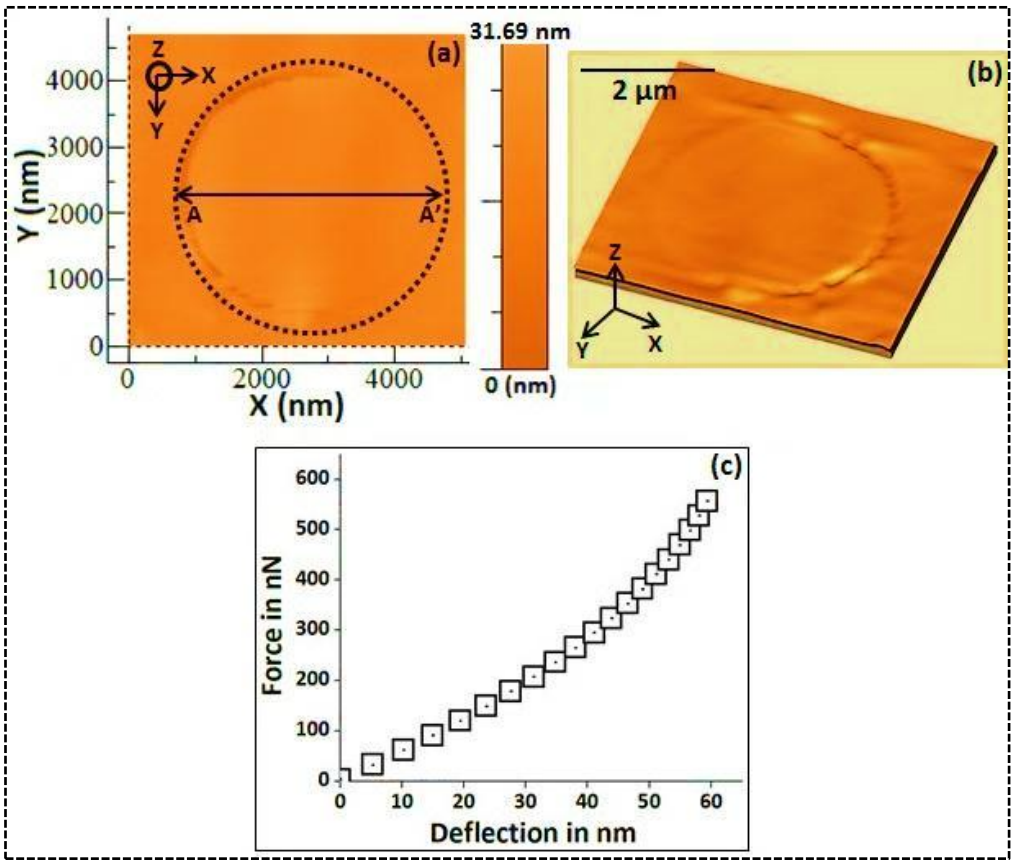

Figure 6-4(a): AFM scan of one of the devices (suspended 5 layer graphene). The diameter of the sample is marked as AA'. (b) A 3D representation of the scan (c) Force versus deflection curve obtained from the nanoindentation of the structure.

6.3 Results and Discussion

6.3.1 Ripple Formation in Few-Layer Graphene

The force curve measurements were carried out for all samples and the estimated pre-tension of 2-, 4- and 5- layer graphene is found to be 1.46 N/m, 2 N/m and 2.3 N/m respectively. Perturbing the 2D system through nanoindentation causes the surface area to change and the system will stabilize by reaching its minimum energy position. The indentation was performed at the same location six times before actually extracting the mechanical properties of the device. The ripple morphology was unaffected after several cycles of indentation. The force versus deflection curves was also observed to be identical after every indentation cycle indicating that there were no irreversible changes to the structure. Therefore extracted mechanical properties of the pristine sample were obtained after confirming the stability of the structure. The effects of nanoindentation on the surface morphology of the devices were investigated by analyzing the post-indentation surface profiles acquired from AFM non-contact mode images. The AFM micrographs obtained before and after nanoindentation of the 2-, 4- and 5- layer suspended graphene structures are shown in Figure 6-5(a-c). The formation of periodic surface corrugations oriented in the lateral direction and displaced in the out-of-plane (z-direction) after indentation is obvious from Figure 6-5(d–f). From Figure 6-5(d) it is also observed that, secondary ripples (ripples in the supported regions of graphene) were formed at the edges of the clamped boundary in the 2- layer sample. The height variation of the ripples across the diameter of the suspended region (across AA') as indicated in Figure 6-4(a) formed in the samples were analyzed [Figure 6-6]. The ripples are found to be with amplitude varying from 7 nm to 22 nm and width ranging from 250 nm to 2 µm across ~4 µm clamped graphene membranes as shown in Figure 6-6(a–c). The number of ripples and the FWHM of the large amplitude ripple in Figure 6-6(a–c) as a function of layer number is plotted in Figure 6-7(a) and Figure 6-7(b) respectively.

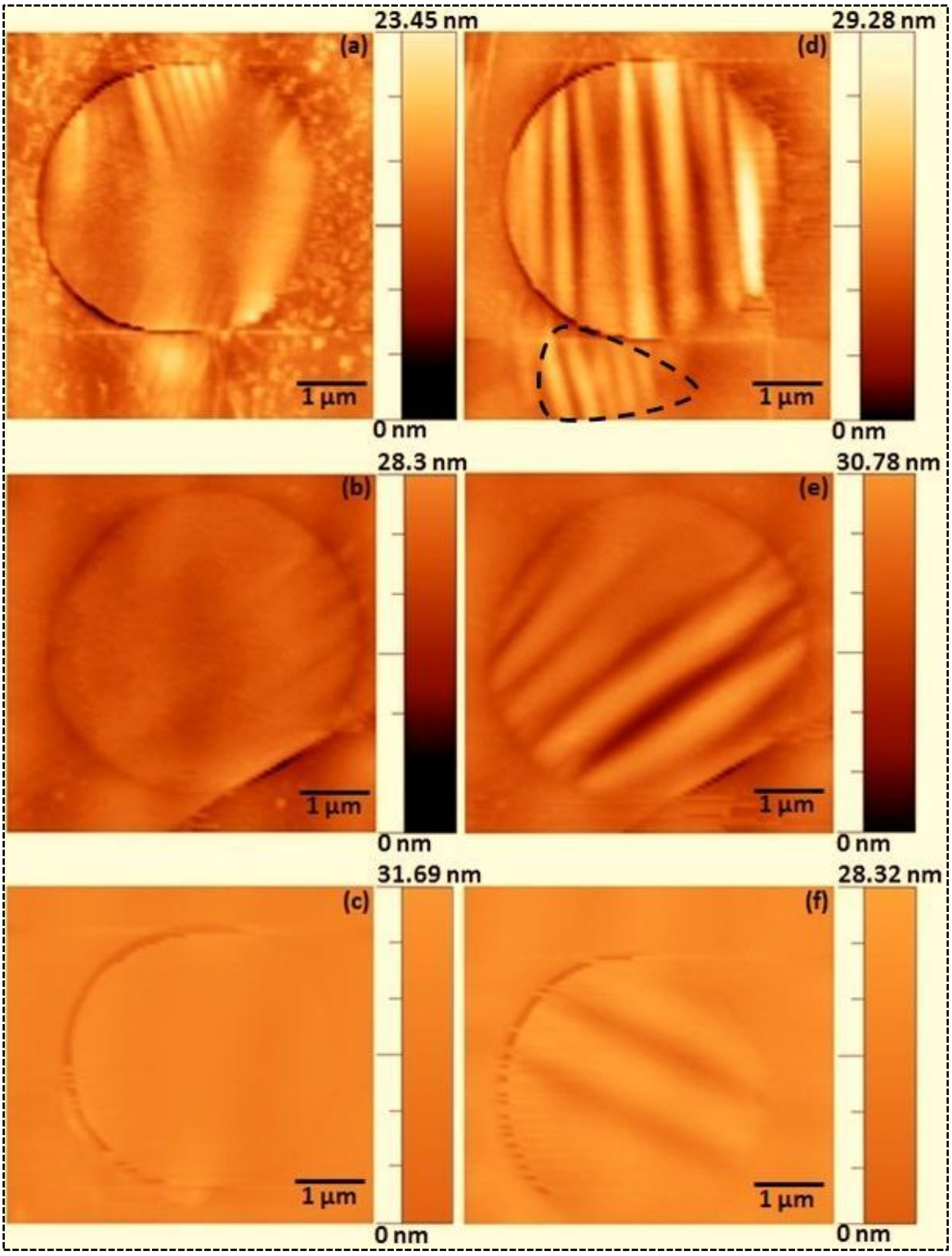

Figure 6-5: (a–c) AFM topography images of 2-, 4- and 5- layer suspended graphene structures obtained before nanoindentation respectively. (d–f) AFM topography images showing surface morphology variation after indentation of 2, 4 and 5 layer graphene respectively. The region marked with dotted lines in 5(d) corresponds to secondary ripples in 2-layer graphene.

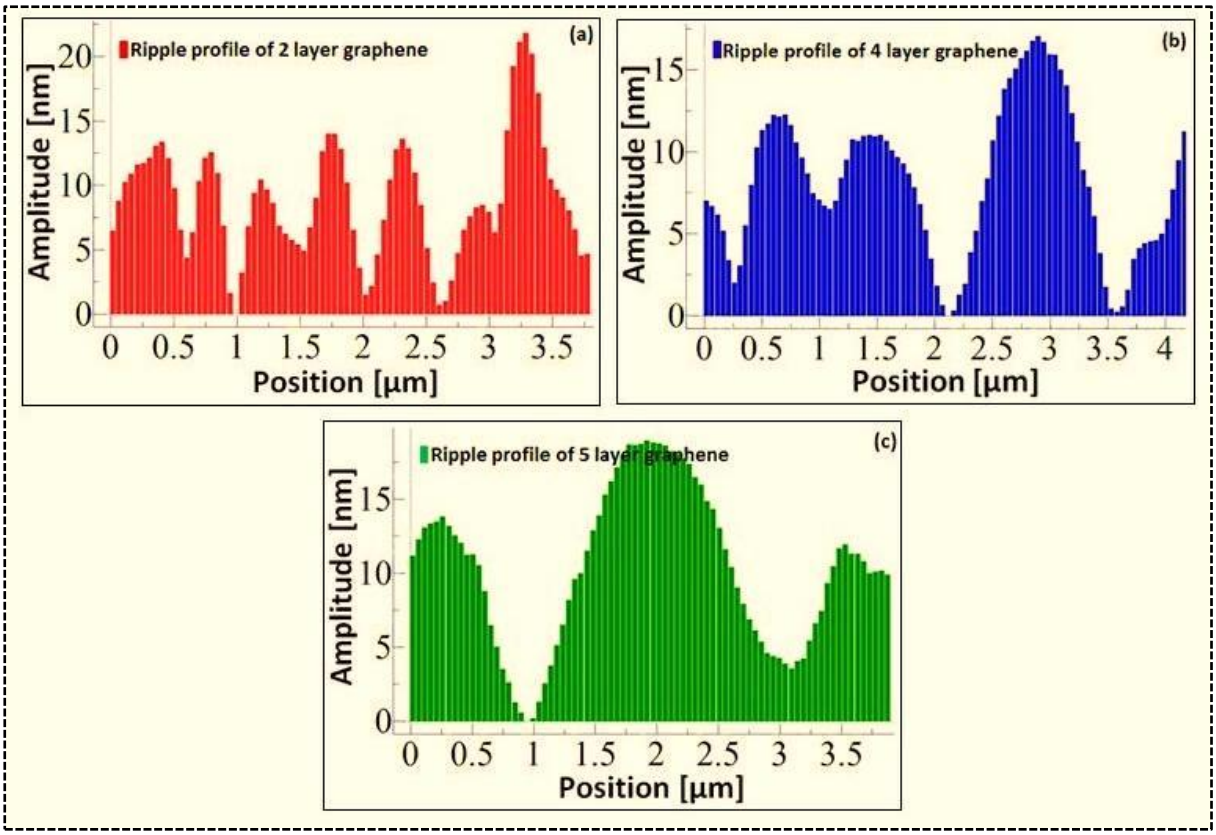

Figure 6-6: (a–c) Profile graphs showing the height variation along the diameter AA' (marked in Fig. 4(a)) of the fabricated devices (2-, 4- and 5- layer graphene respectively) extracted from Fig. 5(d–f).

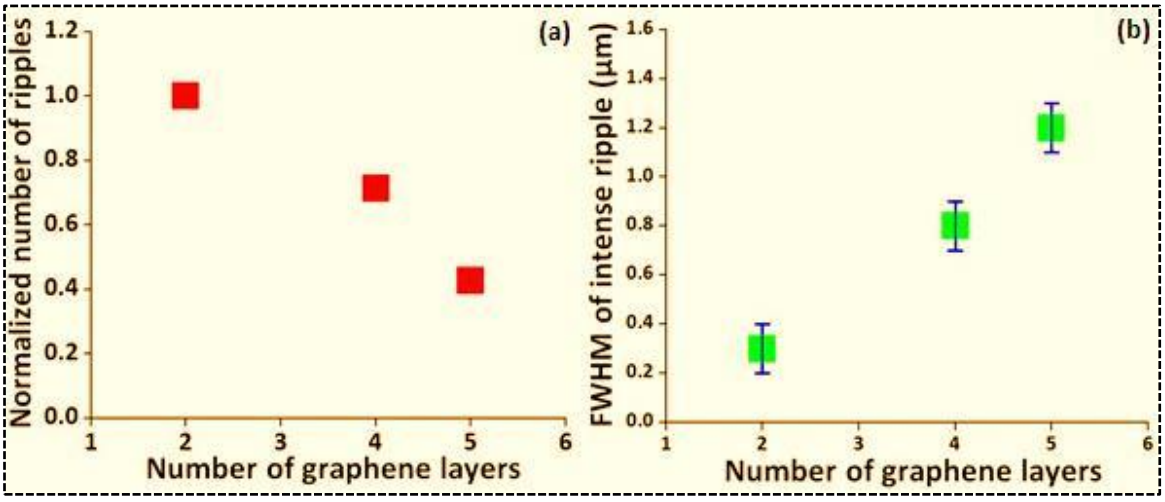

Figure 6-7: (a) Number of ripples versus layer number and (b) FWHM of the large amplitude ripple as a function of layer number.

The formation of ripples in suspended graphene membrane is a result of circumferential compression induced by the nanoindentation process and the stabilization of the instantaneously deformed structure is determined by the in-plane and bending stiffness [145]. The intrinsic ripples already present in the sample could also be modified in this process. The

out-of-plane excitation induced by the AFM probe tip leads to the modification of local surface morphology which includes flattening of the pre-existing thermal ripples and emergence of new high amplitude stable undulations [147]. The intrinsic thermal ripples were found to be flattened due to anharmonic stabilization which causes the bending and stretching modes to be coupled. [18][147].

The orientation angle of the ripples in each structure is found to be unique. The clamping condition of a suspended graphene is not isotropic and therefore the mechanical compression caused during nanoindentation alters the edges of the structure at the clamped contacts. The induced ripples will be oriented along the resultant anisotropic local strain and the orientation of these extrinsic ripples will be unique for each sample due to the above mentioned reasons. Thus the orientation of the ripples in Figure 6-5(d–f) is attributed to the resultant anisotropic strain direction in the structure and hence aligned along the direction of strain [140]. It is clear from Figure 6-6 & Figure 6-7(a) that as the number of graphene layers increases the density of the ripples get suppressed. The FWHM of the large amplitude ripple is found to increase with increase in number of graphene layers as shown in Figure 6-5, Figure 6-6 and Figure 6-7(b). It is also found that, the number of wrinkles decrease with increase in graphene thickness and is barely visible for thicker graphene. The stiffness of a graphene structure increases with increase in thickness and therefore the formation of out-of-plane ripples is less countenanced in thicker graphene. Morozov et al. and Singh et al. have recently reported that the ripples becomes lesser and suppressed with increasing number of graphene layers [151][152]. It should also be noted that, the radius of an AFM nanoindenter tip used is 8±2 nm and if the ripple sizes are less than the size of the probe tip (< 10 nm); it would not be possible to resolve in the current study.

The indendation process proves the capability of producing ripples of amplitude 7–22 nm and wavelength 250 nm – 2 μm in few-layer graphene samples. Xu et al. found that, ripples of

~10 nm in width and ~3 nm in height in graphene results in the formation of midgap states along with a decrease in conductivity [153]. This indicates that corrugations of few nm width and amplitude are found to have a deep impact on the electrical properties of graphene devices [153].

6.3.2 Thermal Engineering of Induced Ripples

To demonstrate the effects of high vacuum annealing on indentation induced ripple structure in graphene, results obtained from bilayer graphene sample is discussed in detail in this section. Bilayer graphene has recently drawn special attention mainly due to the tunability of its bandgap [154]. The electronic bandgap plays a significant role in the transport [155][157] and optical properties [154][159] of graphene based devices such as p-n junctions, field-effect transistors and optoelectronic devices. Hence, tunable bandgap in bilayer graphene helps to realize useful characteristics for flexible electronics and devices. Very recently, Yan et al. have demonstrated a dual-gated bilayer graphene hot-electron bolometer which exhibits an intrinsic speed (>1 GHz) and noise-equivalent power (33 fW $Hz^{-1/2}$) [160]. The mechanical properties of the pristine and annealed samples have also been studied. The capability to introduce extrinsic undulations in bilayer graphene through nanoindentation thus enables new research directions to study the spring constant mapping of rippled structure. Also, the mechanically induced local curvature variations open up possibilities to tune the optical transparency limits of graphene and the different sizes of ripples enable its use for optical lenses with tunable focal length.

6.3.2.1 Results and Discussion

The AFM topography image of the suspended bilayer graphene structure is shown in Figure 6-8(a). The force versus displacement (F-δ) curve of the sample after nanoindentation is shown in Figure 6-8(b).

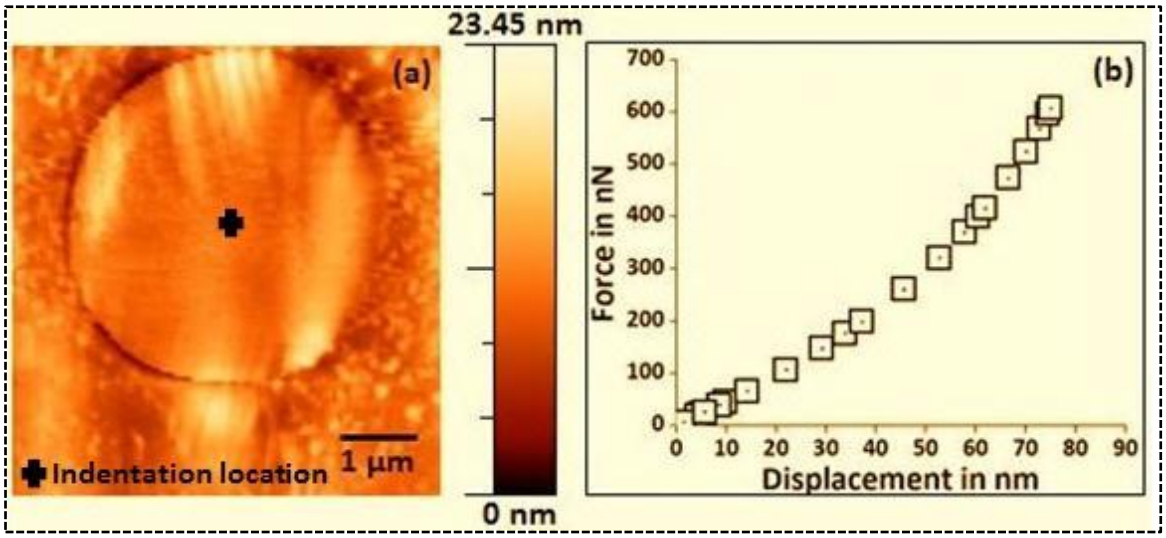

Figure 6-8: (a) Two dimensional AFM scan image of the suspended bilayer graphene. (b) Force versus deflection curve obtained from the nanoindentation of the structure.

From the *F-δ* curves, the spring constants, pre-tension and Young's modulus were estimated and are shown in Table 6-1. Figure 6-8(a) and Figure 6-9(a) show the two dimensional AFM scan image obtained before and after indentation. The mechanical properties and surface morphologies of the same sample were investigated after in-situ vacuum (2.8×10^{-4} Pa) annealing at 350 °C in the AFM chamber. An AFM micrograph of the sample after annealing is given in Figure 6-9(b) and the corresponding line profile is shown in Figure 6-9(b'). The flattening of the nanoindentation induced ripples [Figure 6-8(a) and Figure 6-9(a')] after annealing is evident from Figure 6-9(b). The mechanical properties and variations in surface morphology of the annealed sample were again investigated. The AFM image and the corresponding force versus displacement curve obtained from the annealed structure after nanoindentation is shown in Figure 6-10(a) and Figure 6-10(b) respectively. The increase in amplitude of the thermally generated undulations after indentation can be seen in Figure 6-10(a) and the deduced mechanical properties from Figure 6-10(b) are shown in Table 6-1.

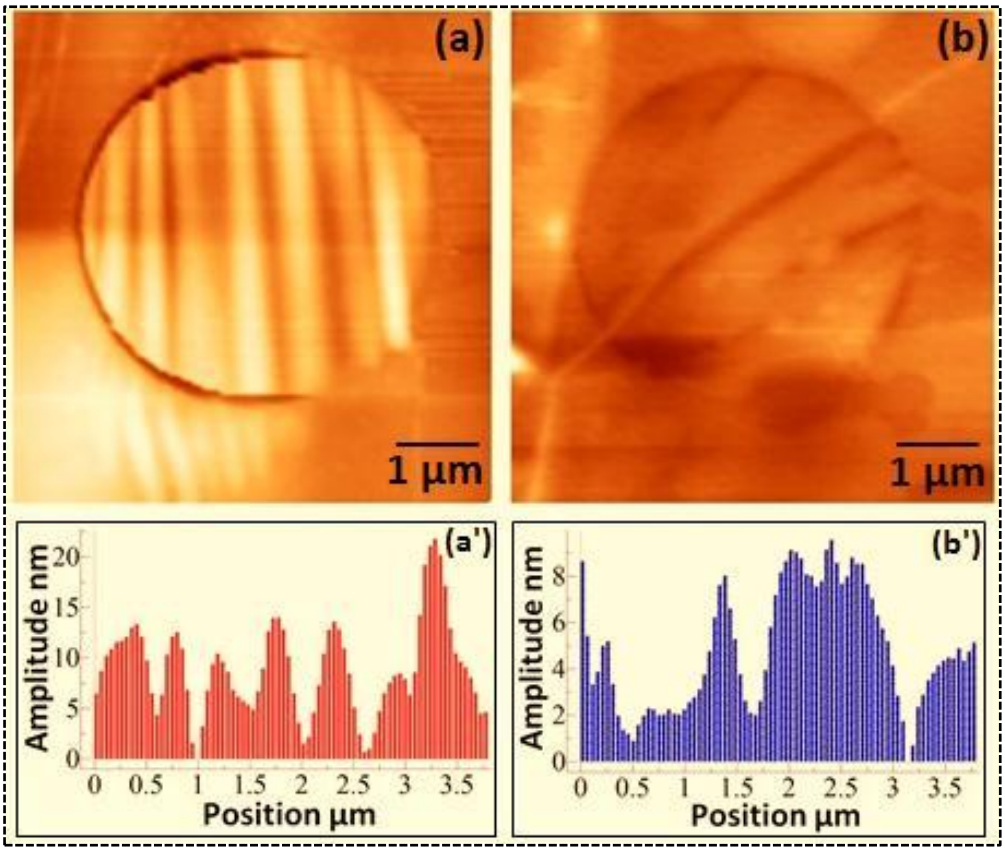

Figure 6-9: AFM topography images obtained (a) After nanoindentation. (b) After vacuum annealing and subsequent cooling. The corresponding line profiles (across diameter AA' as shown in figure 2) of the device structure after nanoindentation and after temperature treatment are shown in (a') and (b') respectively.

Figure 6-10(b) and Figure 6-10(b') clearly show the alteration in the ripple geometry after annealing. The plausible reason for this observation could be the strain induced by the thermal expansion coefficient (TEC) mismatch between the graphene and the substrate. The TEC of graphene is found to be negative while for silicon substrate it is positive, i.e. graphene contracts and silicon expands on heating. The thickness of the SiO_2 (~285 nm) in the substrate is much smaller than the silicon thickness (~550 µm) and hence the effect of SiO_2 TEC can be safely neglected when compared to the contributions from silicon [140]. First principle calculations by Mounet et al. showed that the TEC of graphene is negative for a wide range of temperature (up to 2500 K) [161]. A very recent continuum theory of elasticity study by de Andres et al. also showed that monolayer and bilayer graphene exhibit negative TEC up to 700 K [162]. Silicon possesses a positive TEC for the entire temperature

range (300 K to 1500 K) [163]. The above indicated large TEC mismatch between the graphene membrane and the underlying substrate causes biaxial strain and leads to thermal deformation between graphene and the substrate [140]. During heating, the substrate/trench expands while graphene membrane contracts and hence graphene experiences biaxial tension. In the event of cooling, graphene undergoes compressive stress due to the contraction of the substrate [164]. Hence, surface morphology of graphene is found to have been significantly altered after thermal annealing and cooling. Ripple geometry alteration includes flattening of the nanoindentation induced ripples and appearance of low density static fluctuations. Bao et al. have also observed flattening of pre-existing ripples and emergence longer wavelength ripples at room temperature after annealing the suspended samples at similar temperature (~700 K) used in this study [140][165]. After temperature treatment the direction of this resultant clamping condition would be altered and thus the ripple orientation in figures Figure 6-9(a) and Figure 6-9(b) are found to be different [140].

The mechanical properties (pre-tension, Young's modulus linear and nonlinear spring constants) of the structure have also undergone significant reduction and the values are shown in Table 6-1. The pre-stress associated to graphene after fabrication is found to have been lowered by 50% after thermal treatment. Thus the mechanical properties of the nanostructure have been considerably lowered and under the same applied force, the displacement in the structure after annealing is found to be more than the deflection before heat treatment. Thus thermal annealing if found to be one of the ways to alter the mechanical properties of graphene devices. Annealing graphene at 300 ^{o}C was reported to enhance the performance of graphene based field effect transistors by a factor of 90 and exhibiting very high transconductance value of 5900 µS/µm (corresponding carrier mobility ~2230 cm^2/Vs) [166].

By repeated mechanical loading the texture of the ripple were observed to be modified as indicated in Figure 6-11(a-d) and Figure 6-11(a'-d').

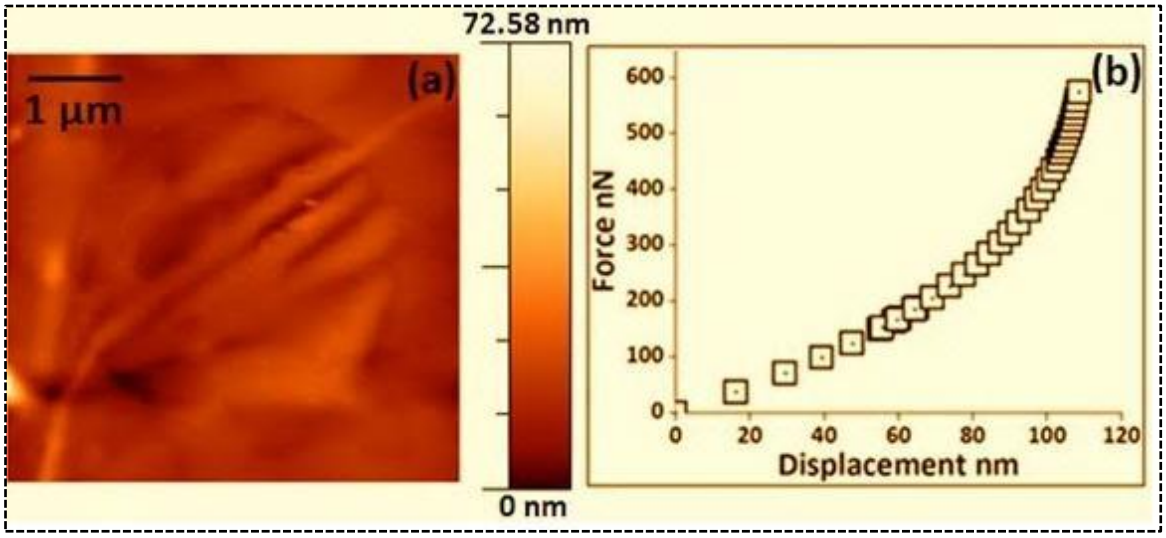

Figure 6-10: (a) AFM micrograph of the annealed suspended bilayer graphene sample obtained after indentation (b) Force versus displacement curve obtained from the nanoindentation of the annealed structure.

Table 6-1: Summary of estimated mechanical properties

Label	Before Annealing	After Annealing
Linear spring constant N/m	4.6	2.27
Nonlinear spring constant × 10^{14} N/m^3	5.8	1.6
Pre-tension N/m	1.46	0.72
Young's modulus TPa	3.25	0.78

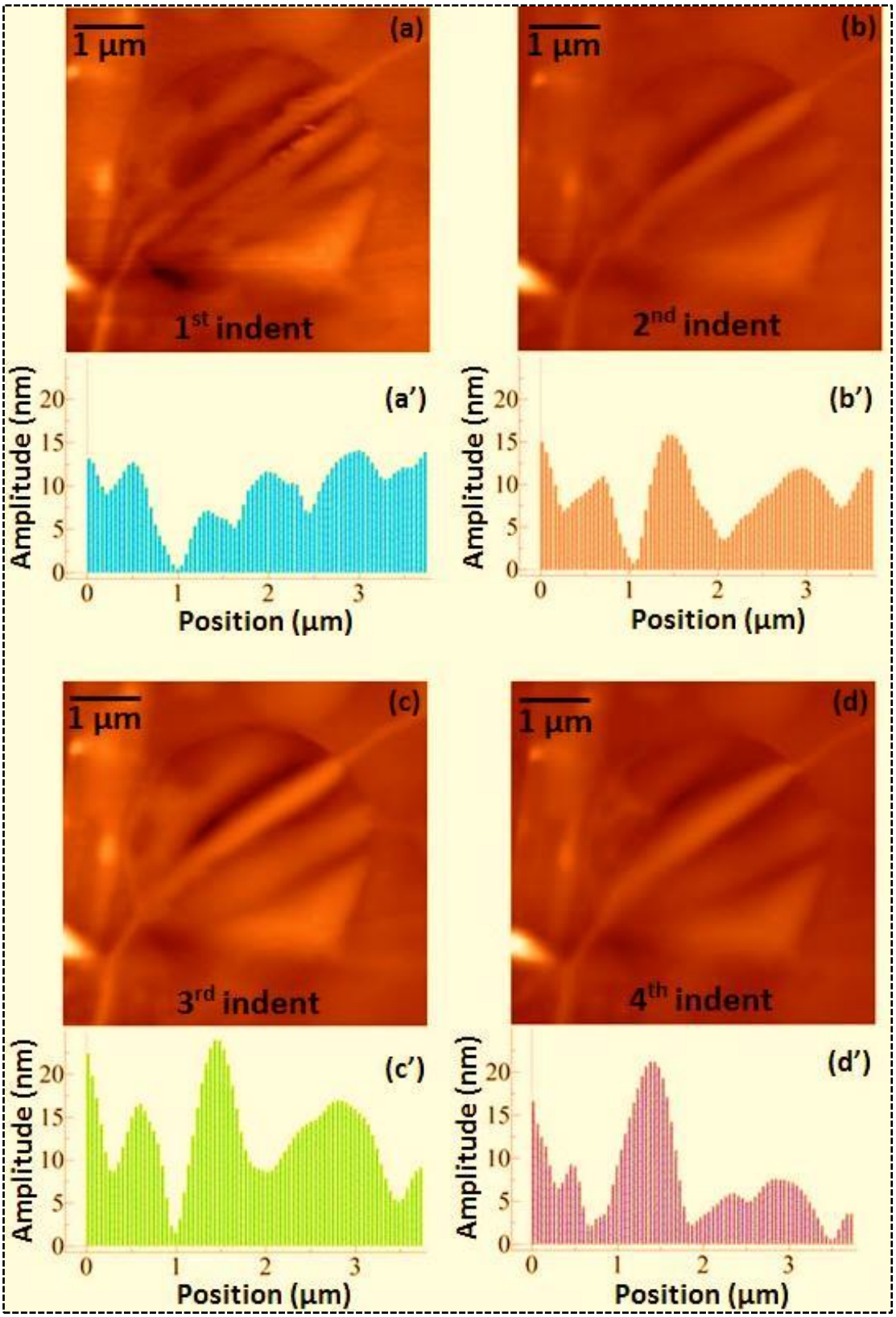

Figure 6-11: (a-d) AFM scan images obtained after each indent cycle. (a'–d') Corresponding profile graphs showing the height variation along the diameter AA' of the device after each indent cycle.

The capability to introduce extrinsic undulations in graphene through nanoindentation thus enables new research directions to study the spring constant mapping of the rippled structure. Also, the mechanically induced local curvature variations open up possibilities to tune the optical transparency limits of graphene and the different sizes of ripples enables its use for optical lenses with tunable focal length [167][168].

6.4 Conclusions

The point-contact perturbation method employed in this study alters only the local surface morphology without modifying the contiguous regions. Controlling the local texture of free-standing graphene by AFM nanoindendation and thus engineering the electrical [126]–[129], chemical [132][153] and magnetic properties [130][131], can lead to future flexible electronic devices. Thermal engineering of the nanoindentation induced ripples have also been demonstrated in bilayer graphene. Significant alteration in ripple morphology after annealing was observed, which include flattening of nanoindentation-induced ripples and presence of thermally generated undulations. NEMS is typically an integration of nanoelectronics and mechanical devices and the ability to produce tunable electronic components based on graphene along with its mechanical benefits enables a tremendous development of NEMS technology.

In the previous chapters, characterization of pristine graphene was demonstrated. It is also important to study the behaviour of such systems with induced defects as they would be prone to lattice imperfections in various environmental conditions. Therefore, in the following chapter, properties of irradiation induced damaged graphene has been explored.

CHAPTER 7 : MECHANICAL PROPERTIES OF IRRADIATED AND PATTERNED GRAPHENE

7.1 Overview of Irradiated Graphene

Graphene being the main focus of interest in material science is found to exhibit unique mechanical and electronic properties as discussed in the previous chapters. It is very important to understand the behaviour of graphene based systems under various environmental conditions which can induce structural defects. This is because the properties of pristine graphene would be affected when used for different applications. Moreover, such study would also be helpful to carefully manipulate its structure which can in turn be used to tailor its properties.

The lattice imperfections (e.g. vacancies, reconstructions with non-six member rings and voids) caused by irradiation using ions, protons or electrons can drastically alter the electronic [169], thermal [170], mechanical [171], magnetic [172] and optical properties of graphene. The damage threshold of supported and suspended graphene samples when exposed to 2 MeV H^+ irradiation was found to increase with layer number [121]. Ion irradiation on graphene sheets deposited on SiO_2 by 500 keV C^+ ions also showed that the disorder in monolayer is more than bilayer and multilayer graphene sheets [173]. Lehtinen et al. have studied the effects of ion bombardment on graphene and have shown that graphene can be used as a wrapping membrane for ion beam analysis on volatile targets or living cells which should be separated from the vacuum system [174]. It has been shown using STM imaging that electronic structure of monolayer graphene can be tuned using 30 keV Ar^+ ions by inducing disorder which substantially reduces the Fermi velocity [176]. Stolyarova et al. have observed graphene bubbles after irradiating graphene using energetic protons (0.4-0.7 MeV) and have demonstrated that these mono-atomic sheets can trap gases for sufficiently long period of time [176]. Electron beam induced defects in graphene field-effect transistors

is also found to decrease the carrier mobilities and minimum conductivity [177]. Lopez et al. reported enhanced resistance of single layer graphene on SiO_2/Si substrate exposed to 30 kV Ga^+ ion beam [178]. Nanopatterning using 30 keV He^+ beam to obtain sub -10 nm feature sizes in suspended graphene have also been achieved [68] and is demonstrated in detail in the following section. Krasheninnikov and Nordlund have reviewed the ion and electron irradiation induced effects in carbon allotropes and other nanostructured materials [179].

In this chapter, suspended graphene nanomechanical devices have been exposed to 500 keV helium ions and the ion beam induced defects were studied using Raman spectroscopy. The corresponding changes in mechanical properties at various ion fluences have also been explored for the very first time. The induced defects were found to decrease with an increase in layer number. Monolayer graphene is found to remain suspended and the surface morphology analysis indicates the bulging of the mono and multilayer graphene even after irradiating with an ion fluence of 1.1×10^{17} ions/cm^2. The variation of Young's modulus with respect to ion fluence has also been investigated in the current work.

7.2 Experimental Details

Suspended graphene samples were prepared by adopting the fabrication technique described in Section 3.1. Graphene samples prepared by exfoliation technique tend to be contaminated with adhesive tape residues and adsorbed molecules from the environment. When the exfoliated graphene samples were irradiated with focussed 30 keV He ions, the hydrocarbons from the sample were found to be re-deposited on the graphene sample [68]. Jones et al. reported the formation of graphane and partially hydrogenated graphene by electron irradiation (5-10 keV) of adsorbates on graphene [180]. Using electrostatic force microscopy study it is reported that a monolayer of water molecules is adsorbed on top of exfoliated graphene samples exposed to air. [181]. The pristine graphene samples used for the ion

irradiation study has thus been annealed at 400 °C for 8 hours inside a tube furnace in the presence of forming gas (5% H_2 and 95% Ar) to remove the tape residues. The annealing temperature and duration used was found to be effective in removing the tape residues. The graphene samples were also heated (250 °C for 30 min) inside the irradiation chamber before each irradiation step to remove the adsorbed molecules that has been adsorbed from the ambient air. The pristine samples mentioned in the later part of the text refer to the graphene annealed in a tube furnace for removing the adhesive tape residues.

Ion irradiations were carried out using a 3.5 MV Singletron facility at CIBA, NUS. The graphene samples were loaded into the nuclear microscopy chamber with a strip heater attached in the sample holder and the samples were annealed before each irradiation step as mentioned before. A collimated beam of 500 keV helium ions was focused to a beam spot size of ~5 μm on the target chamber using a set of quadrupole lenses. The graphene flake was identified using an optical microscope which is attached to the irradiation chamber. The focused ion beam was then raster-scanned under normal incidence over an area of 2×2 mm^2 with the graphene flake positioned at the centre of each scan. The chamber pressure and ion beam current density during the irradiation experiments were maintained at 1×10^{-6} mbar and 50 nA/mm^2 respectively. Visible Raman spectroscopy (excitation wavelength - 532 nm) was carried out using a WITec CRM200 Raman system. The Raman spectrum was analyzed by curve fitting using multiple Lorentzians with a sloping background. AFM imaging (tapping mode) and AFM nanoindentation of the pristine and irradiated samples was carried out using JEOL JSPM 5200.

7.3 Results and Discussion

Ion irradiation experiments were carried out on monolayer, bilayer and 5 layer suspended graphene samples. The optical microscopy image of the samples used is shown in Figure 7-1. The thickness of the graphene samples were confirmed using Raman spectroscopy.

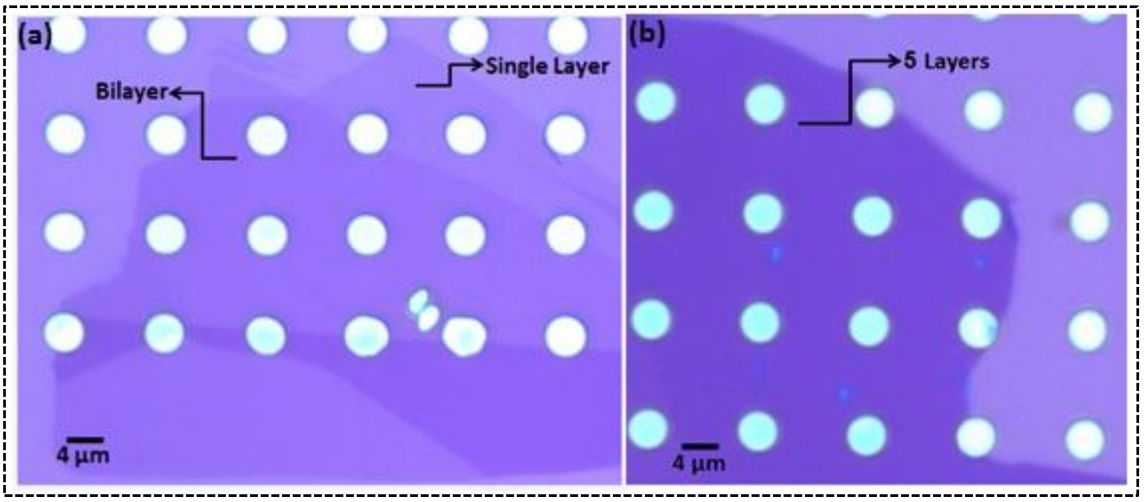

Figure 7-1: Optical micrograph showing (a) Suspended bilayer and monolayer graphene (b) Suspended 5 layer graphene.

7.3.1 Raman Spectroscopy Results

The graphene samples were irradiated at four different ion fluences (8×10^{15}, 3×10^{16}, 7×10^{16} and 1.1×10^{17} ions/cm^2). The corresponding Raman spectra obtained from the pristine and irradiated monolayer, bilayer and 5 layer suspended graphene samples are shown in Figure 7-2, Figure 7-3 and Figure 7-4 respectively.

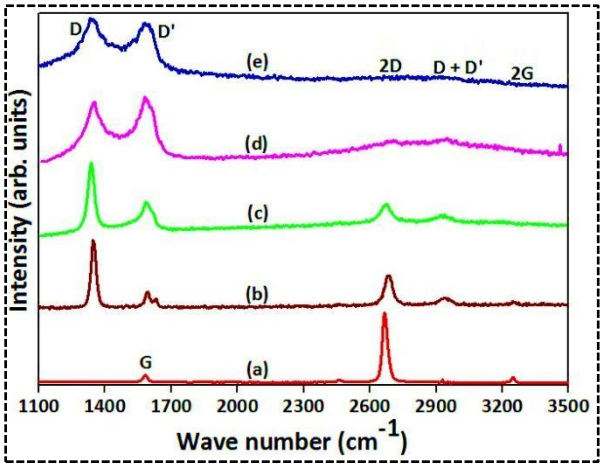

Figure 7-2: Raman spectra obtained on a suspended monolayer graphene (a) Pristine (b) After 1st irradiation (8×10^{15} ions/cm^2) (b) After 2nd irradiation (3×10^{16} ions/cm^2) (c) After 3rd irradiation (7×10^{16} ions/cm^2) (d) After 4th irradiation (1.1×10^{17} ions/cm^2).

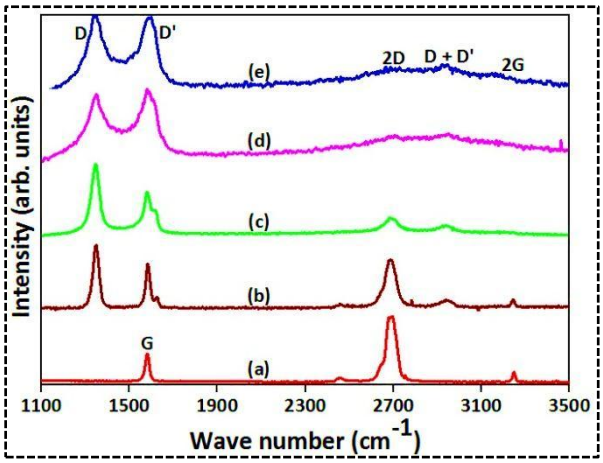

Figure 7-3: Raman spectra obtained on a suspended bilayer graphene (a) Pristine (b) After 1st irradiation (8×10^{15} ions/cm^2) (b) After 2nd irradiation (3×10^{16} ions/cm^2) (c) After 3rd irradiation (7×10^{16} ions/cm^2) (d) After 4th irradiation (1.1×10^{17} ions/cm^2).

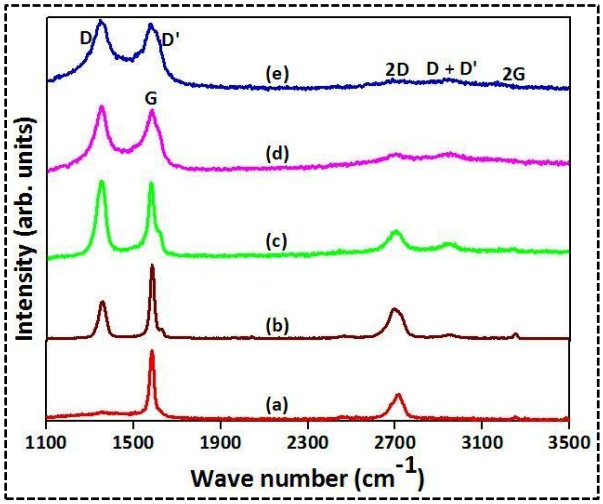

Figure 7-4: Raman spectra obtained on a suspended 5 layer graphene (a) Pristine (b) After 1st irradiation (8×10^{15} ions/cm^2) (b) After 2nd irradiation (3×10^{16} ions/cm^2) (c) After 3rd irradiation (7×10^{16} ions/cm^2) (d) After 4th irradiation (1.1×10^{17} ions/cm^2).

The prominent Raman modes in Figure 7-2(a), Figure 7-3(a) and Figure 7-4(a) are the G mode at ~1580 cm^{-1} and the 2D mode at ~2700 cm^{-1} respectively [182]. The FWHM of the 2D peaks from the three figures Figure 7-2(a), Figure 7-3(a) and Figure 7-4(a) are found to be 33 cm^{-1}, 50 cm^{-1} and 65 cm^{-1} which corresponds to monolayer, bilayer and 5 layer graphene respectively [66].

Graphene samples irradiated at a fluence of ~ 8×10^{15} ions/cm^2 begin to show a D mode at ~1340 cm^{-1} (see Figure 7-2(b), Figure 7-3(b) and Figure 7-4(b)). This is the in-plane breathing mode of A_{1g} symmetry due to the presence of six-fold aromatic rings and requires a

defect for its activation [182]. The ratio of the integrated intensities of D to G (denoted as I(D)/I(G)) increases with ion fluence. In the irradiated samples, apart from D, G, and 2D modes, another peak at ~2930 cm^{-1} which is a combination mode of D and D' is also visible [182]. As the fluence increases, the second order peaks increase in width and in Figure 7-2(d), Figure 7-3(d) and Figure 7-4(d) those peaks are barely seen. The deconvolution of the spectra in the irradiated samples show a sharp mode at ~1623 cm^{-1} called the D' mode [182]. The I(D)/I(G) ratio increases with ion fluence in all the graphene samples. The fluence dependence of the damage from the Raman spectra of the pristine monolayer, bilayer and 5 layer suspended graphene samples are shown in Figure 7-5. The variation of I(D)/I(G) ratio with ion fluence φ for 2- and 5- layers can be fitted using the $f(\varphi) = \alpha\ [1 - e^{-(\varphi/\varphi_0)}]$ where α and φ_0 are the two fitting parameters.

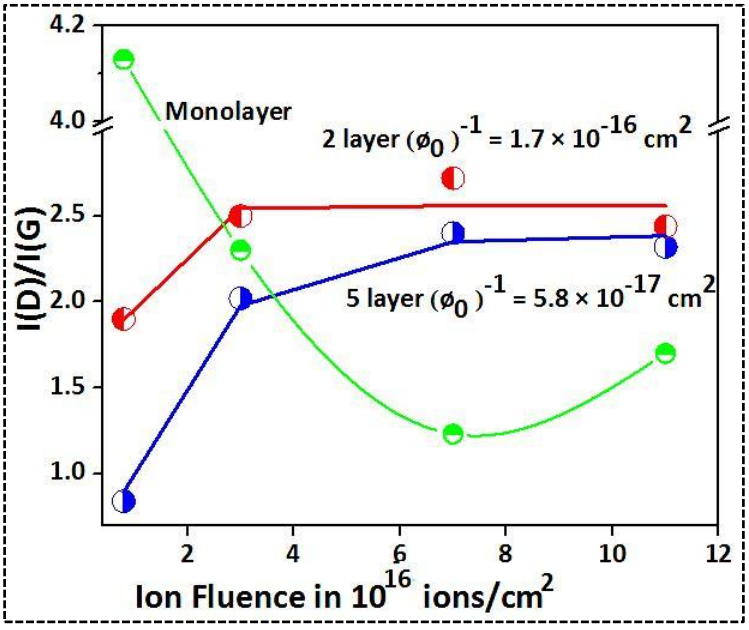

Figure 7-5: The variation of I(D)/I(G) for monolayer (green), bilayer (red) and 5 layer (blue) with ion fluence. The spectra are fitted using $f(\varphi) = \alpha\ [1 - e^{-(\varphi/\varphi_0)}]$.

The best fitted curves with experimental data are shown in Figure 7-5. The parameter α being a fixed value, the non-linearity in defect production comes from the second factor of the equation, which essentially presents the probability of generating defect at a given ion

fluence. The parameter $(\varphi_0)^{-1}$ represents damage cross section for the impact of a single ion. From Figure 7-5, it can be seen that the value of $(\varphi_0)^{-1}$ for a bilayer is found to be higher than that of 5 layer graphene samples. For monolayer graphene, the damage is even higher and the I(D)/I(G) ratio is found decrease with ion fluence as discussed in Ref. [183]. An idea about the contribution of ballistic effects in the present keV He irradiation on graphene system can be estimated by calculating the displacements per target atoms (dpa) using TRIM simulations. If we consider sputtering due to head-on collisions, the calculated displacements per atom from TRIM simulations [184] yield about 0.01 dpa at a fluence of 10^{17} ions/cm^2. For TRIM simulations, the sample is treated as an amorphous matrix with homogenous mass density and the ion kinetic energy is transferred ballistically to the target atom. Also TRIM simulations treats the dissipation of transferred energy in a 3D system, whereas for the case of a 2D system like graphene the transferred energy is dissipated in a two-dimensional plane. The electronic and the nuclear energy loss of 500 keV He^+ ions in an amorphous carbon target with the density of graphite is estimated (using TRIM [184]) to be 43 eV/Å and 0.084 eV/Å respectively. The above factor is based on Ziegler-Biersack-Littmark (ZBL) theory of ion stopping [184] and cannot explain the nature of the observed damage and the quenching of the defects with layer number. Production of defects in nano-systems is different from that in bulk materials. The system dimensions and size significantly affect the dissipation of energy brought in by the energetic particle.

7.3.2 AFM Nanoindentation Results

Nanoindentation experiments were carried out in ambient conditions on the pristine and the irradiated monolayer, bilayer and 5 layer suspended graphene samples and the corresponding mechanical properties were determined (see Chapter 5 for details on the experimental procedure and analysis). All the AFM imaging and nanoindentation experiments were carried out using a ~1.2 N/m AFM cantilever. A typical force curve obtained on a hard SiO_2 surface

and on a pristine monolayer sample is shown in Figure 7-6. Similar force curves were obtained after each irradiation step on all the suspended graphene samples and the curves were analysed using the continuum mechanics model (see Chapter 5 for details) to extract the mechanical properties.

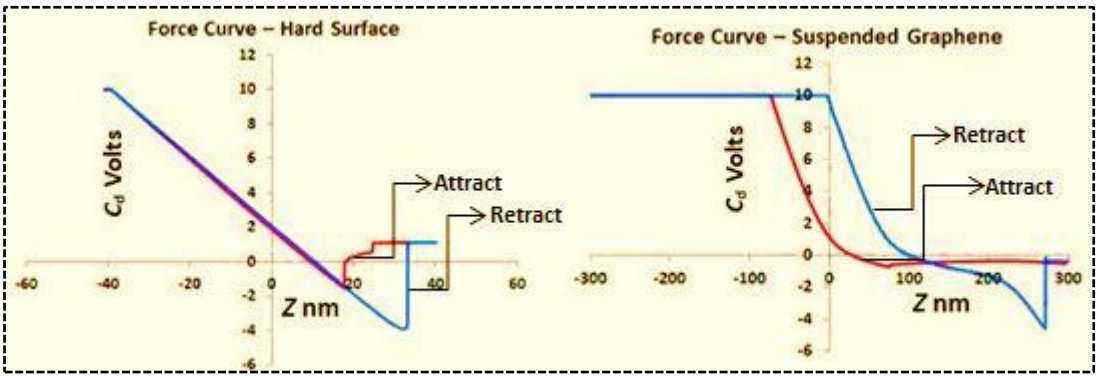

Figure 7-6: Force curves obtained from AFM nanoindentation experiments on a SiO_2 surface (left) and pristine monolayer suspended graphene (right).

The AFM tapping mode image was obtained to confirm the suspension of the graphene samples after each irradiation step. The AFM images obtained on one of the pristine and irradiated (after 4th irradiation) monolayer, bilayer and 5 layers graphene samples are shown in Figure 7-7(a–c). From these images and the corresponding line profiles it is evident that all the graphene samples remain suspended even after exposing it to an ion fluence of 1.1×10^{17} ions/cm^2. Graphene of all thicknesses ranging from monolayer to few-layer shows a formation of bubble (bulge) after irradiation. These bubbles indicate that graphene can trap gases. These samples were imaged again after ~2 months to confirm the stability of such bubbles. The images confirmed the presence of bubbles and this observation indicates the robustness of the quasi two-dimensional material, graphene. This clearly shows that graphene can be used in harsh environmental conditions and also finds intriguing applications such as usage as an ultimate membrane to wrap the targets, like living cells which has to be separated from the vacuum system during ion beam analysis [176].

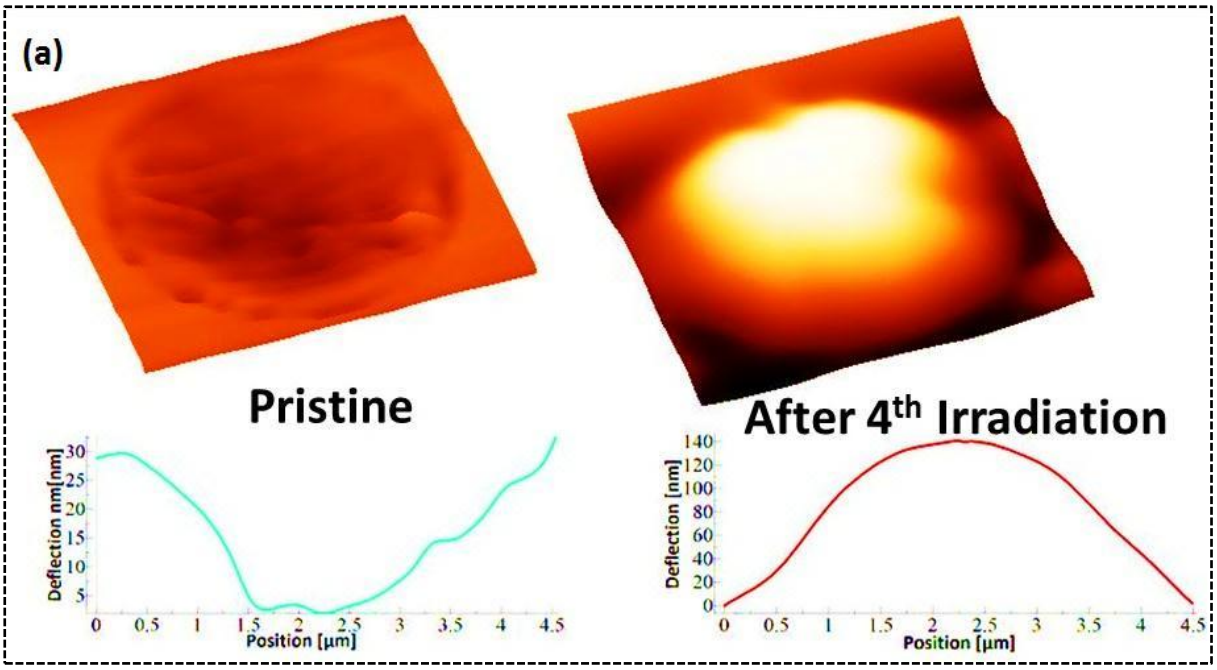
(a)
Pristine
After 4th Irradiation
Deflection nm[nm]
Deflection [nm]
Position [µm]
Position [µm]

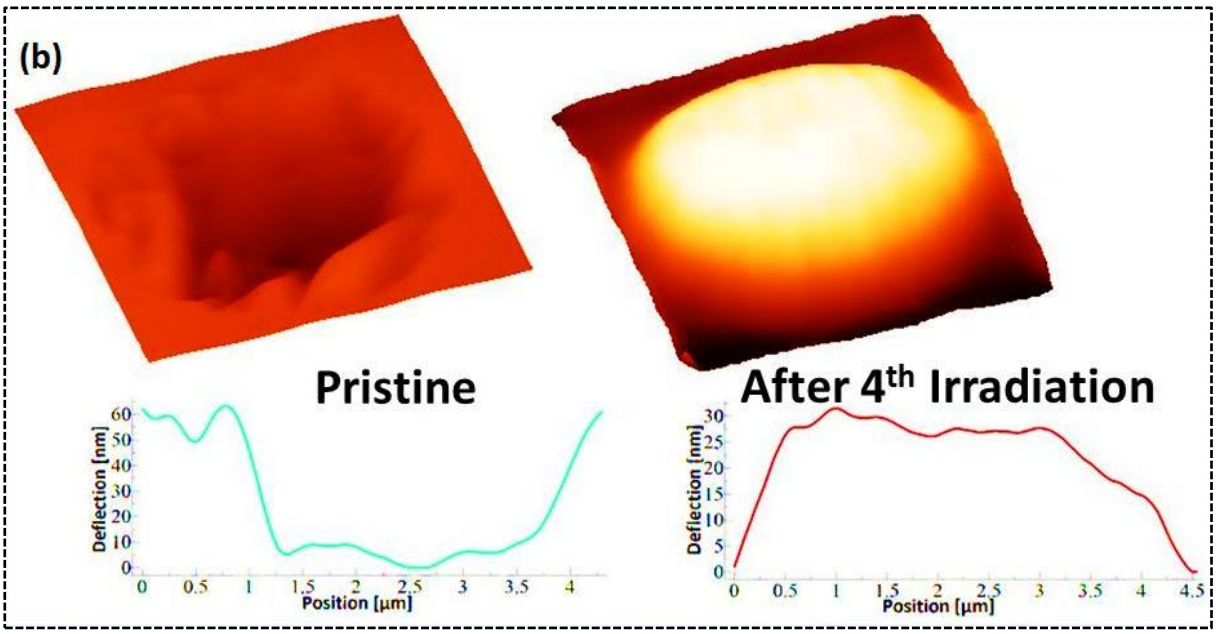
(b)
Pristine
After 4th Irradiation
Deflection [nm]
Deflection [nm]
Position [µm]
Position [µm]

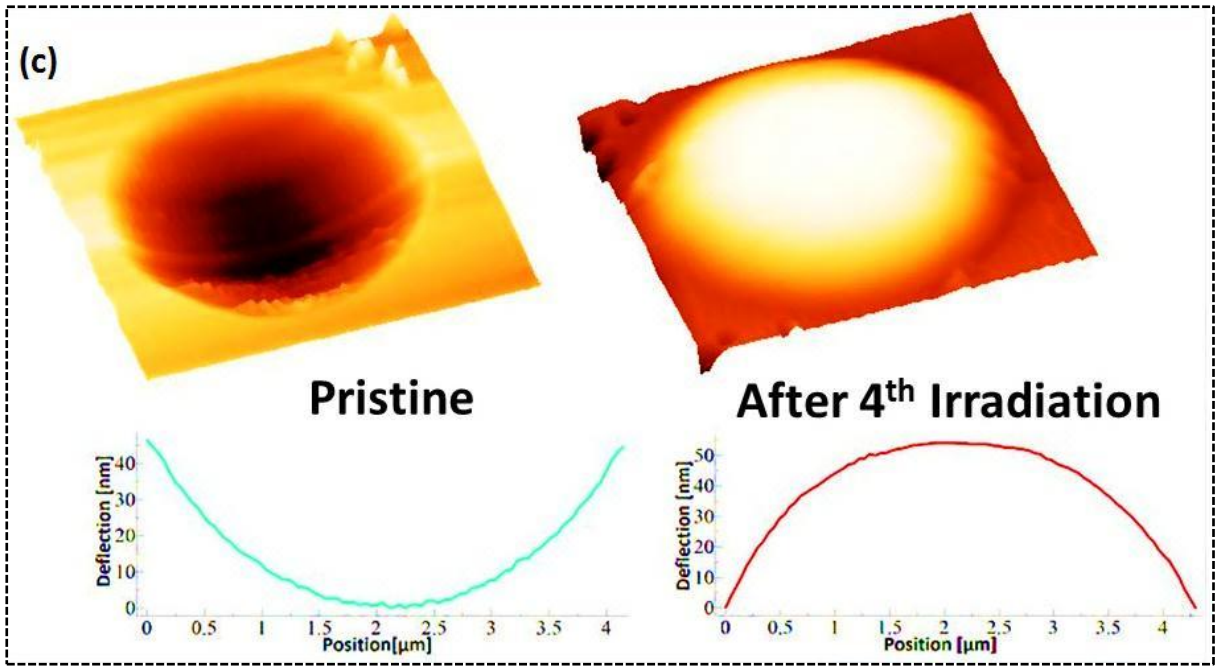

Figure 7-7: AFM topography images obtained using tapping mode on (a) Monolayer pristine and irradiated sample (1.1×10^{17} ions/cm^2) (b) Bilayer pristine and irradiated sample (1.1×10^{17} ions/cm^2) (c) 5 layer pristine and irradiated sample (1.1×10^{17} ion/cm^2).

The mechanical properties from the force versus deflection plots were extracted for the pristine as well the irradiated samples. The deflection plots and the corresponding changes in the mechanical properties (Young's modulus and pre-tension) obtained from one of the 5 layer and bilayer samples with ion fluence are shown in Figure 7-8(a–c) and Figure 7-9(a–c) respectively. It is very clear from the obtained results that the Young's modulus of the 5- and 2- layer graphene has increased after irradiating with an ion fluence of 8×10^{15} ions/cm^2. With subsequent irradiation with increase in ion fluence, the Young's modulus and the pre-tension of the samples were found to decrease. Moreover, in spite of irradiating graphene samples with a high ion fluence of 1.1×10^{17} ions/cm^2, the samples remain suspended without any detrimental effects in its mechanical properties. This clearly demonstrates that, graphene possess very high ion irradiation tolerance even with an increase in irradiation induced damage. These defective graphene structures which include monolayer, bilayer and 5 layer suspended graphene did not show any signs of instability or breakage when exposed to high ion fluences (~1.1×10^{17} ions/cm^2). Even with an increase in accumulation of the

irradiation damage as evident from the Raman spectroscopy results, the AFM nanoindentation results demonstrate the ability of graphene to withstand the consecutive irradiation with an increase in ion fluence.

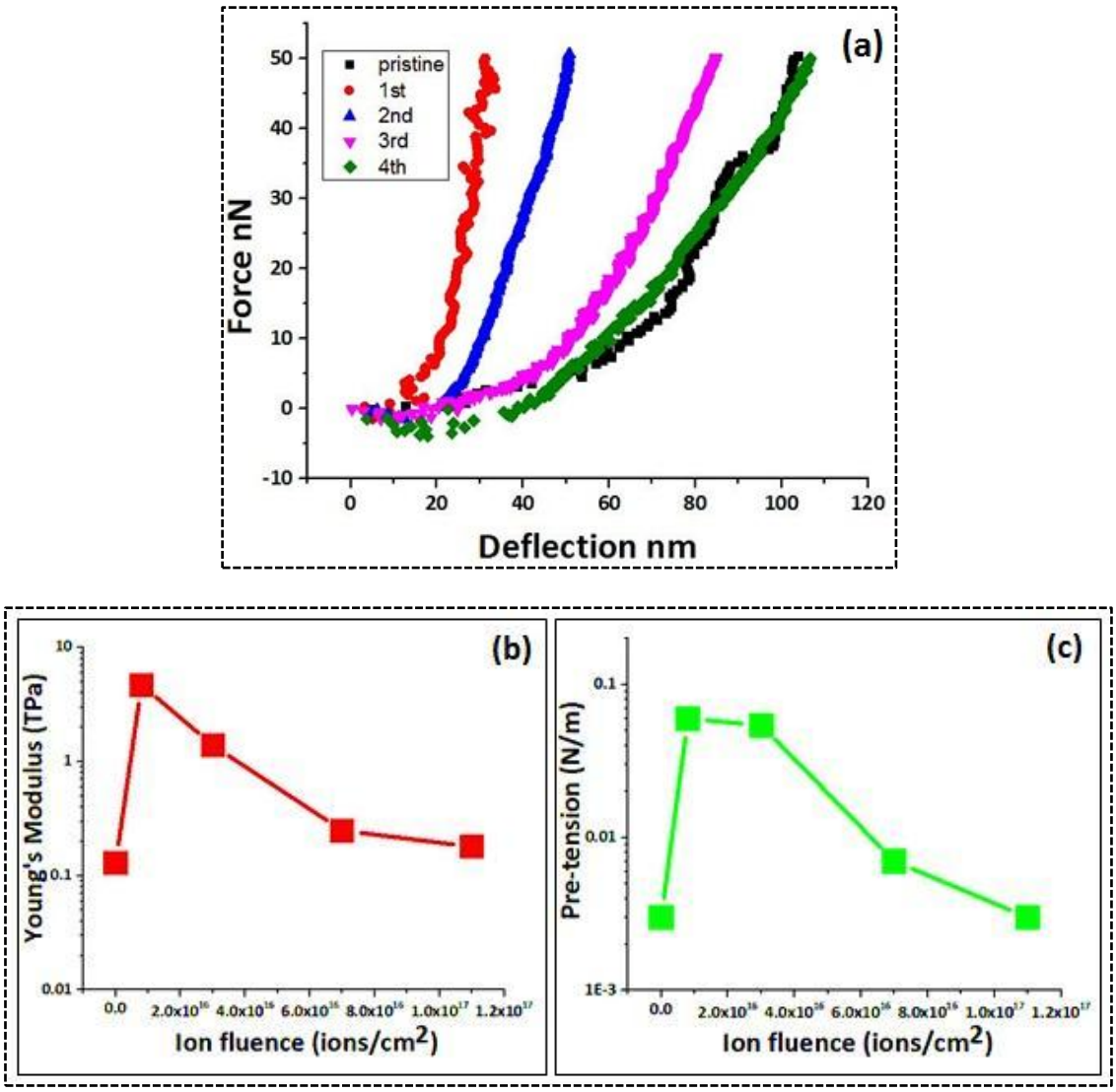

Figure 7-8: (a) Force versus deflection curves obtained from a pristine and irradiated 5 layer graphene sample (b) Young's modulus variation with respect to ion fluence (c) Pre-tension variation with respect to ion fluence.

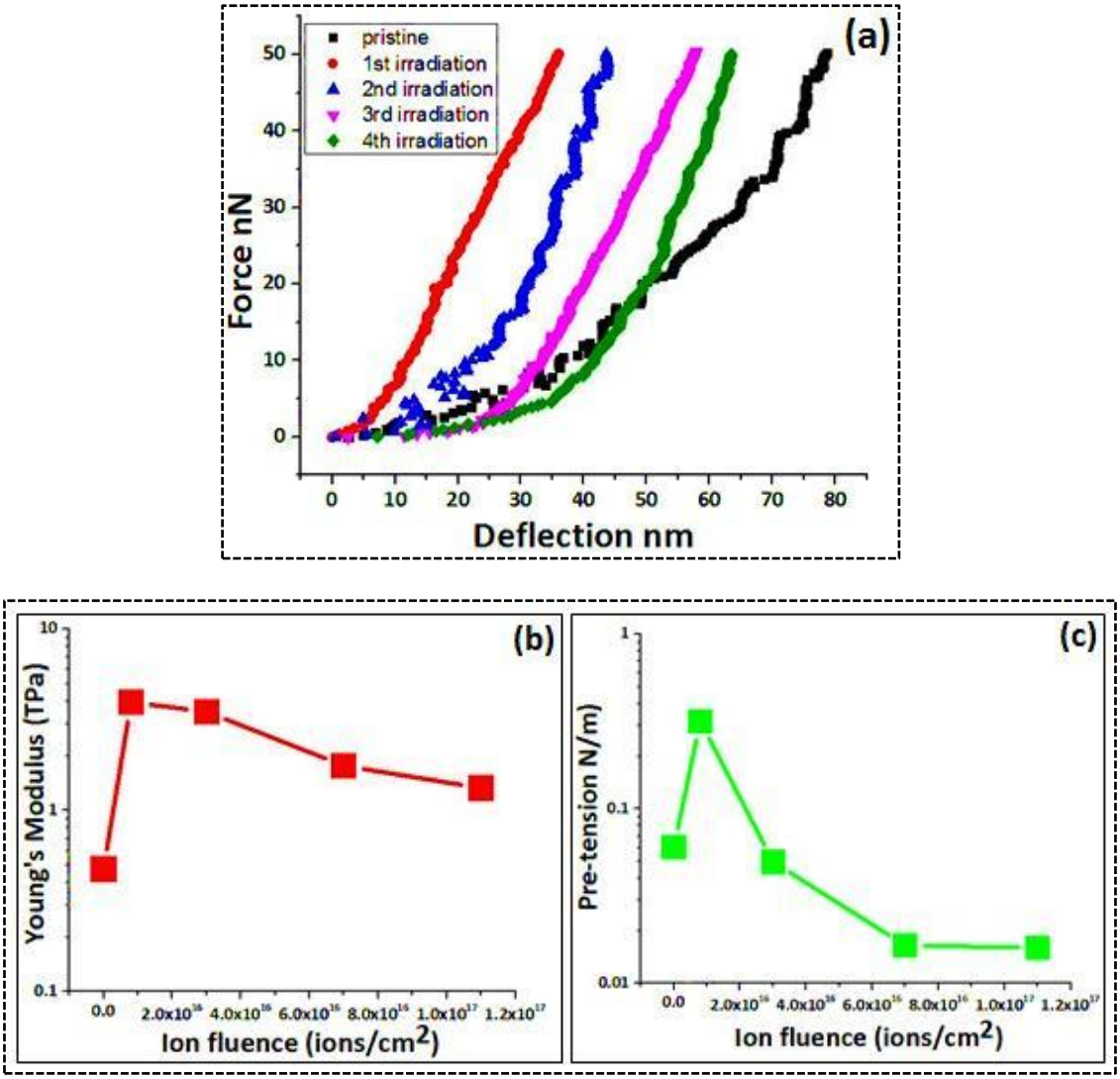

Figure 7-9: (a) Force versus deflection curves obtained from a pristine and irradiated bilayer graphene sample (b) Young's modulus variation with respect to ion fluence (c) Pre-tension variation with respect to ion fluence.

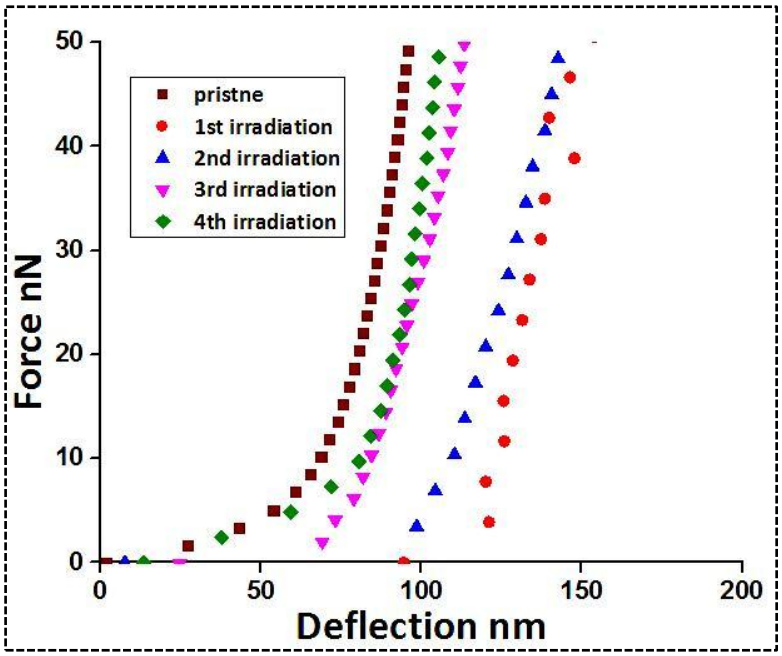

Figure 7-10: Force versus deflection curves obtained from a pristine and irradiated monolayer graphene sample.

The force versus deflection plots obtained for the irradiated monolayer sample could not be fitted using the continuum mechanics model to extract its mechanical properties. It was observed that even for very low forces (~few nN) the membrane had deflected more than 50 nm which resulted in loss of data in the lower force region (see Figure 7-10) due to the use of the same AFM cantilever (stiffness ~1.2 N/m). One needs to use a cantilever of lower stiffness to extract and compare the mechanical properties of monolayer. The induced defects in the monolayer are found to be more than multilayers as indicated in Figure 7-5.

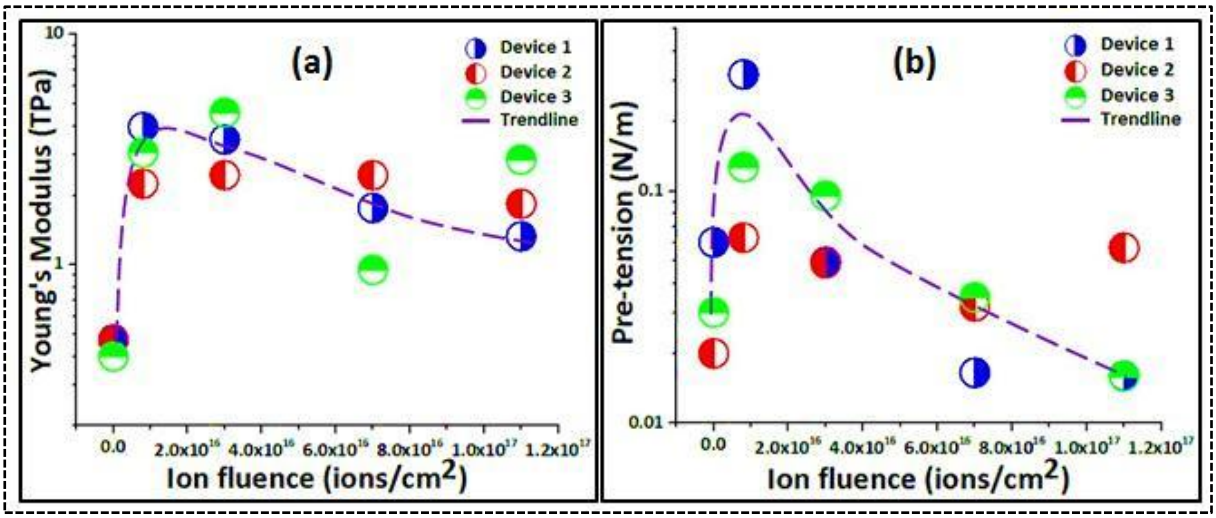

Figure 7-11: (a) Variation of Young's modulus with respect to ion fluence for three suspended bilayer graphene devices (b) Variation of pre-tension with respect to influence for three suspended bilayer graphene devices.

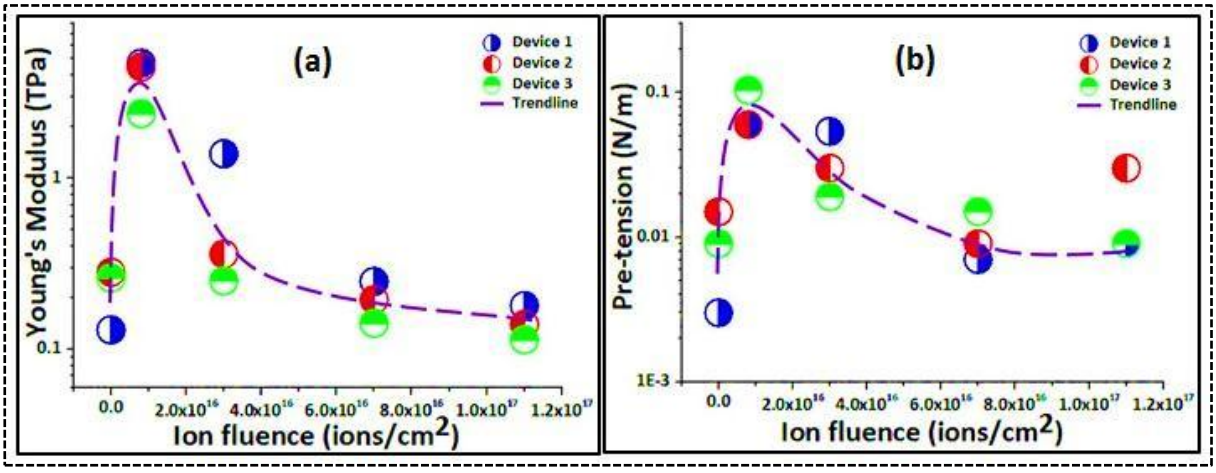

Figure 7-12: (a) Variation of Young's modulus with respect to ion fluence for three suspended 5 layer graphene devices (b) Variation of pre-tension with respect to influence for three suspended 5 layer graphene devices.

In order to show the repeatability and consistency in the measurement results, the mechanical properties of bilayer and 5 layer suspended graphene versus ion fluences is plotted for three different device structures (see Figure 7-11 and Figure 7-12).

7.4 Nanopatterning of Graphene – An Overview

Some of the existing methods to pattern graphene structures include electron beam lithography (EBL), scanning probe methods, focussed ion beam (FIB) milling and direct etching using electron beam in TEM. These milling methods can generate patterns with

feature sizes of several tens of nm but impose certain difficulties. The conventional EBL which is a resist-based lithography, leaves resist residues on graphene and it is also not suitable to pattern suspended graphene structures [185]. Scanning probe methods offers high spatial resolution but the process of patterning is slow and it is not feasible to pattern suspended graphene as well [186]. Focussed ion beam milling based on liquid-metal ion sources (LMIS) is not suitable for patterning narrow structures (beam spot size 3-7 nm) and causes significant damage to the graphene layer [187]. The high energy (80-300 keV) required for direct etching using an electron beam [188] creates undesired deposition of carbon or defects which cause graphene to lose its crystallinity. Moreover, this method requires transfer of graphene to TEM grids and sophisticated sample preparation which make the process very tedious. In order to overcome the difficulties of the conventional methods, suspended graphene structures have been patterned using helium ion microscope. HIM patterning offers high precision milling as well as sub-nm resolution imaging. Helium ions are more massive than electrons which eliminate the diffraction effects due to the short de Broglie wavelength unlike conventional scanning electron microscopes. Helium is also less massive than gallium which overcomes the limitation of sub-surface sample damage usually present in FIB systems. The above stated advantages of HIM provide sub-nm resolution imaging and milling. Typically doses needed for imaging is two orders of magnitude less than the dose used for milling. Therefore, non-destructive imaging of the samples can be obtained before and after nanopatterning. Any complex geometric design or arbitrary patterns can be created using the NPGS software and the milling time to create such patterns would be ~few seconds.

HIM patterning enables a straightforward means to vary the dimensions of the device structures which opens up an excellent opportunity to obtain devices with varying frequencies. The results obtained from nanostructuring of graphene as indicated below,

clearly shows that HIM is an emerging technology to obtain nanoelectromechanical structures with enhanced design and performance variations. Moreover, high resolution imaging with high surface sensitivity has evidently enabled to inspect the patterns created on graphene. The fabrication sequence and the working principle of a HIM have been discussed in detail in Sections 3.1 and 3.5 respectively. Figure 7-13 show as an AFM image of a suspended drum which was patterned to obtain z-axis diaphragm flexure. The potential devices have been annealed at 350 degrees for 4 hours in the presence of forming gas (5% H_2, 95% Ar) in a tube furnace which facilitated the removal of glue residues that gets attached to the samples during graphene transfer. Glue residues, if present will cause adverse effects during patterning.

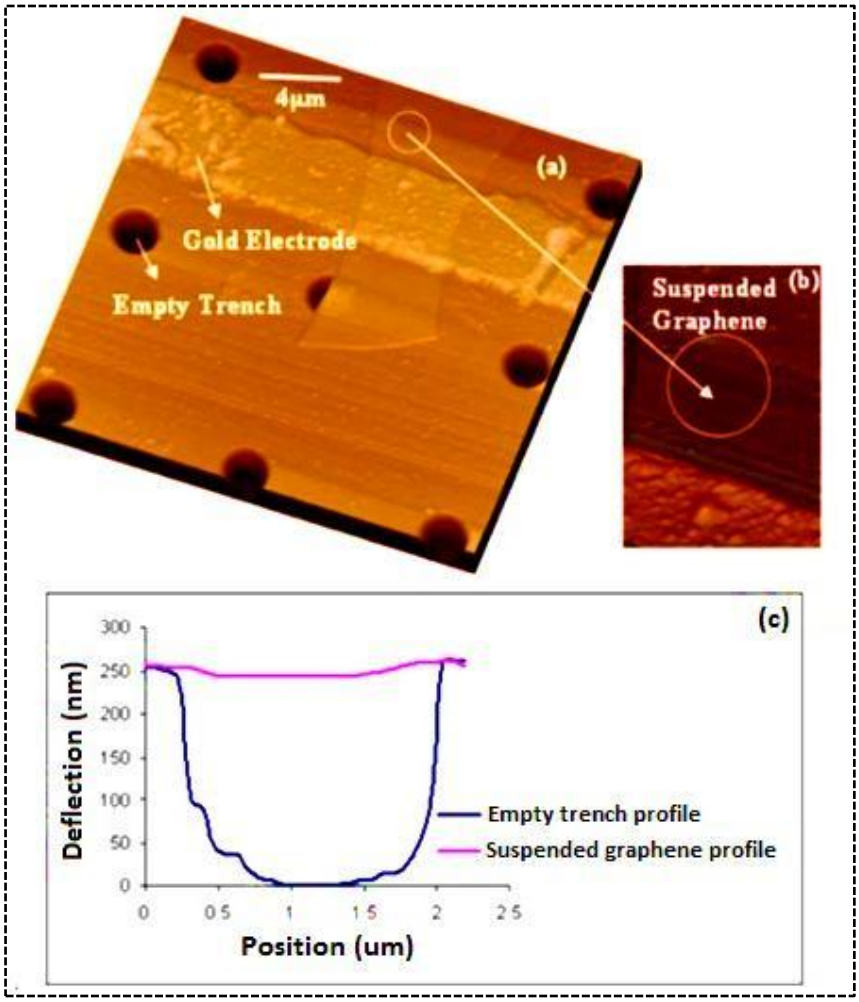

Figure 7-13: (a) Three dimensional AFM image showing suspended graphene membrane and empty trenches (b) An enlarged view of the suspended graphene (c) Superimposed AFM profiles of suspended graphene (initial sag – 10 nm) and an empty trench (~250 nm).

7.5 HIM Patterning

Direct patterning of the different NEMS structures were obtained by helium ion beam with a Nanometer Pattern Generation System (NPGS, from JC Nabity Lithography Systems, Bozeman, Montana). The various patterns achieved are shown in Figure 7-14. These patterns were achieved using 30 keV He^+ ions with an ion beam current of 0.4 pA at a fluence of ~10^{18} ion/cm^2. The helium ion beam was raster scanned on the surface of the graphene membrane to obtain the design created using NPGS. Suspended graphene drum structures have been patterned to obtain z-axis diaphragm flexures. The main advantage of these types of flexures is that they offer smooth elastic motion without introducing nonlinearities like friction. Diaphragm flexures are radial arrangement of flexure beams. Analyses on these types of flexures have been studied previously [189]. Figure 7-14 shows the nested patterns obtained using HIM and they clearly indicate that high precision milling is possible.

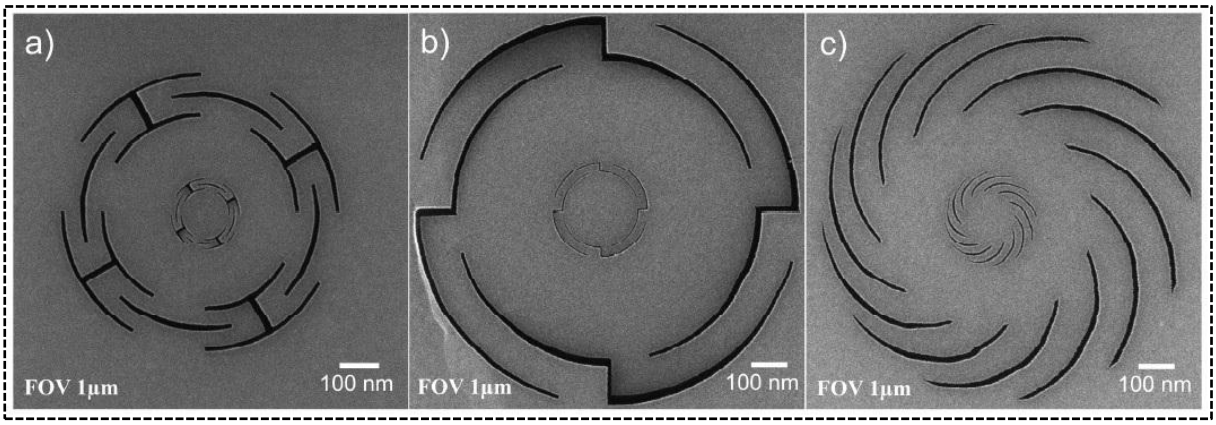

Figure 7-14: Nested planar diaphragm structures demonstrating the range of dimensions achievable with this technique. The inner structures have sub -10 nm features (FOV) – 1 µm. Symmetrical (a) Multi folded flexure (b) Circular diaphragm flexure and (c) Spiral Archimedes.

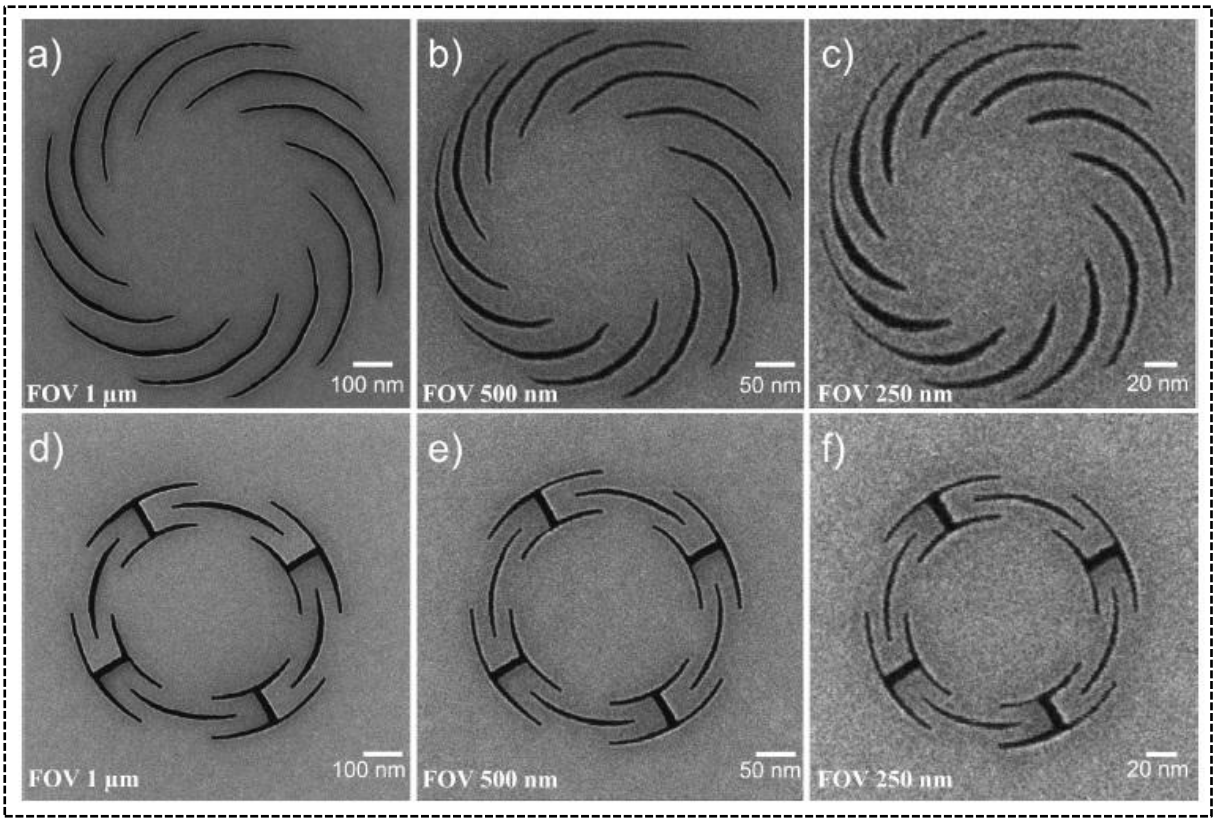

Figure 7-15: Circular diaphragm flexures (a) Spiral Archimedes (FOV – 1 µm) (b) Spiral Archimedes (FOV – 500 nm) (c) Spiral Archimedes (FOV – 250 nm) (d) Symmetrical multi folded flexure (FOV – 1 µm) (e) Symmetrical multi folded flexure (FOV – 500 nm) (f) Symmetrical multi folded flexure (FOV – 250 nm).

The patterned images shown in Figure 7-15 confirm the capability to fabricate a variety of graphene NEMS with sub -10 nm critical dimensions. This opens up a new avenue to fabricate and optimize NEMS based devices such as sensors and resonators with varying mechanical properties.

7.6 FEM Analysis of Patterned Devices

The mechanical response of suspended nanomechanical graphene devices before and after patterning has been estimated using Ansys software. The structures were built using Shell 63 element type. This element type is suited to model thin-wall structures and has both bending and membrane capabilities. The material properties used in finite element modelling include Young's modulus E = 1 TPa, Poisson's ratio $\nu = 0.16$ and material density $\rho = 2200$ kg m^2 [57][81]. Structural characteristics of the fabricated devices and their corresponding

mechanical properties are shown in Table 7-1 and Table 7-2 respectively. FEM results indicate that the suspended nanomechanical graphene structures would potentially vibrate in several 10's of MHz. Their low mass and high operating frequencies make them well suited for mass sensing applications. From the simulations it is obvious that the fabricated devices would possess mass sensitivities greater than 10^{-21} g Hz^{-1}. Figure 7-16 show the simulated mode shape of the devices before and after patterning.

Table 7-1: Structural characteristics of fabricated devices

Label	Structural Characteristics		
	Diameter (μm)	Thickness (nm)	Mass (g)
Device 1	2	11	7.602×10^{-14}
Device 2	3	7	4.948×10^{-17}
Device 3	3	1	7.068×10^{-18}

Table 7-2: Simulated results of suspended graphene

Label	Resonance Frequency f_0 MHz	Mass Sensitivity g Hz^{-1}
Device 1	111	1.369×10^{-21}
Device 2	31.5	3.14×10^{-24}
Device 3	4.5	3.14×10^{-27}

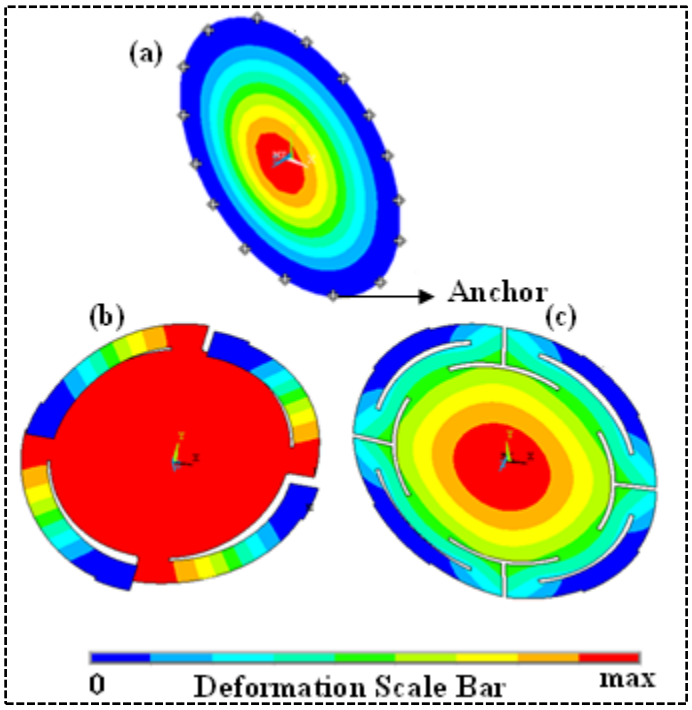

Figure 7-16: Simulated mode shape of suspended graphene. (a) Graphene drum structure (Device 1) before patterning (b) Symmetric circular diaphragm (Device 2) and (c) Multi folded diaphragm (Device 3) after patterning obtained using Ansys.

7.7 Conclusions

Suspended graphene nanomechanical devices were exposed to 500 keV helium ions and the ion beam induced defects and modifications in the mechanical properties have been studied using Raman spectroscopy and AFM nanoindentation respectively. An increase in Young's modulus of bilayer and 5 layer graphene was observed after irradiating with an ion fluence of 8×10^{15} ions/cm^2. Even after subsequent irradiation of the samples with increase in ion fluence did not cause any detrimental effects to the mechanical properties. It has also been demonstrated that graphene bubbles are formed after irradiation and remain without any degradation for sufficiently long period of time. Monolayer, bilayer and 5 layer graphene samples were all found to be suspended in spite of the accumulated damages after irradiating with an ion fluence of 1.1×10^{17} which clearly indicates the unique structural stability of graphene. This study thus shows the high tolerance of graphene to harsh environmental

conditions and hence it would serve as a robust membrane for the future nanoelectromechanical systems.

All the test structures shown in previous chapters are clamped circular graphene membranes. Obtaining sub -10 nm features on the circular membranes with various design capabilities could be achieved through high resolution milling using helium ions. The fabricated suspended graphene membranes have been patterned using Helium ion microscope which has the capability to pattern sub -10 nm features and any arbitrary design can be patterned without any resist. Precision milling at high speed along with high resolution imaging and high surface sensitivity using this technique opens the possibility of mechanical studies in a size range previously unobtainable by current fabrication techniques. Several exemplary graphene drum structures have been presented to demonstrate this capability. Lower mass (~10^{-14} g to 10^{-18} g) and higher operating frequencies (~MHz) make these structures well suited to mass sensing applications and sensitivities greater than 10^{-21} g Hz^{-1} can be achieved.

CHAPTER 8 : CONCLUSIONS AND FUTURE WORKS

"Whatever the future brings, the one-atom-thick wonderland will almost certainly remain in the limelight for decades to come. Engineers will continue to work to bring its innovative by-products to market, and physicists will continue to test its exotic quantum properties. But what is truly astonishing is the realization that all this richness and complexity had for centuries lain hidden in nearly every ordinary pencil mark."

-Andre K Geim and Philip Kim [190]

8.1 Conclusions

Fabrication and characterization of the newly isolated 2D material, graphene, has been addressed in detail in this thesis. The structures were fabricated by micromechanical exfoliation of graphite and subsequent transfer to pre-patterned substrates. Mechanical properties of fabricated multilayer structures have been studied by electrostatic actuation and sensing through AFM imaging. Analytical modelling and FEM simulations have also been incorporated to study the deflection behaviour of graphene. These experiments demonstrates that graphene possesses superior mechanical properties (Young's modulus ~1 TPa) and along with its low mass could make it an alternative material for sensing applications.

In order to overcome the limitations of the electrostatic actuation technique, AFM nanoindentation was used to systematically characterize graphene structures. The effects of layer number on the mechanical properties have been precisely studied. The mechanical properties of the devices have been extracted from the experimental results, by applying a continuum mechanics model. This characterization method is a straightforward and simple technique and can be used to study the mechanical properties of other low dimensional structures. To show this capability, characterization results of suspended MoS_2 prepared by the same exfoliation technique have been presented.

The capability to pattern arbitrary features of sub -10 nm dimensions in the suspended graphene samples through HIM patterning have been demonstrated. This method overcomes

the limitations of conventional lithography techniques and the structures can be directly patterned. This opens the possibilities of mechanical studies in a size range previously unobtainable through other techniques and also enables fabrication of nanoscale devices with varying design and frequencies.

Suspended monolayer and few-layer graphene structures have also been irradiated through helium ion beam at different fluences. The characterized results show the unique nature of graphene to remain suspended even after the formation of defects and lattice reconstruction. Even after subsequent irradiation of the samples with increase in ion fluence did not cause any detrimental effects to the mechanical properties. It has also been demonstrated that graphene bubbles are formed after irradiation and remain without any degradation for sufficiently long period of time. The stability of graphene under such irradiation induced damage proves the robustness of the material and its potential use in the next generation NEMS under harsh environmental conditions.

First experiments showing the capability of inducing nanometer sized ripples in few-layer graphene through nanoindentation have been demonstrated. Tailoring these extrinsic corrugations by vacuum annealing at ~620 K has been achieved. It was also shown that after annealing the mechanical properties of the structures are significantly altered. Ripples in graphene alter the electronic structure of graphene and would thus enable tunable electronic devices. NEMS, being a system with mechanical and electronic components, using graphene's mechanical and electronic benefits will lead to a new technological revolution.

8.2 Recommendations for Future Works

Experimental efforts were taken to study the resonance properties of suspended graphene structures using laser doppler vibrometry (LDV). The device structures (monolayer to few layer) were electrostatically actuated using a sinusoidal ac signal with a dc offset and the

detection of the device vibration was aimed to be sensed through the micro system analyser (MSA 500) which is capable of sensing out-of-plane vibrations up to ~24 MHz with displacements in the order of ~pm. But, unfortunately the resonance peak was not observed and the plausible explanation for this could be the relatively large spot size of the laser beam (~several microns). The diameter of a device structure is ~3.5 µm and the distance between two adjacent holes is ~7 µm. The laser light is thus focussed in the neighbouring regions of a 3 µm diameter device structure and thus causing an enhanced noise from the supported as well as other suspended locations which might mask the actual resonance of the test sample. Therefore developing techniques to study the out-of-plane vibrations of these structures would be worthwhile to find new applications for graphene based devices.

Irradiating few-layer graphene through helium ions show that the Young's modulus of the material increases for certain ion fluence and then decreases with further increase in ion fluence. The fluence used for a monolayer graphene is relatively high which has caused a higher damage cross-section. Hence, performing such irradiation experiments with lower fluences on monolayer graphene and finding the critical fluence up to which the hardness of the material can be increased when compared to the pristine structure will be useful for tuning the physical and mechanical properties of the devices for various applications.

The effects of vacuum annealing on the graphene samples at ~350° C have been discussed in this thesis. Similar test measurements can be carried out at various temperatures in order to study the annealing effects on the mechanical properties of the devices.

The fabrication method adopted in this study produces good quality and defect free graphene sheets. But, producing very large area graphene and transferring it to a specific location on any given arbitrary substrate with certain defined features is an issue. Hence adopting and improving newer methods of fabrication which can produce large area graphene sheets with

quality comparable to exfoliated graphene will be very useful in developing novel devices. The experimental techniques used in this thesis will thus be very useful to explore the properties and applications of such structures.

The field of graphene is very new but enormous progress has been made in the last couple of years since its experimental discovery. Hope more intriguing opportunities open up for physicists and engineers to explore this unique mono-atomic material.

REFERENCES

[1] http://journals.aip.org/Nobel2010.html#6

[2] Lin L W, Howe R T and Pisano A P 1998 Microelectromechanical filters for signal processing *J. Microelectromech. Syst.* **7** 286–294

[3] Wang K, Wong A -C and Nguyen C T -C 2000 VHF free–free beam high-Q micromechanical resonators *J. Microelectromech. Syst.* **9** 347–360

[4] Park J Y, Kim G H, Chung K W and Bu J U 2001 Monolithically integrated micromachined RF MEMS capacitive switches *Sensors Actuators A* **89** 88–94

[5] Liu A Q, Tang M, Agarwal A and Alphones A 2005 Low-loss lateral micromachined switches for high frequency applications *J. Micromech. Microeng.* **15** 157–167

[6] Collier J, Wroblewski D and Bifano T 2004 Development of a rapid-response flow control system using MEMS microvalve arrays *J. Microelectromech. Syst.* **13** 912–922

[7] Geim A K and Novoselov K S 2007 The rise of graphene *Nat. Mater.* **6** 183–191

[8] Zhao H, Min K and Aluru N R 2009 Size and chirality dependent elastic properties of graphene nanoribbons under uniaxial tension *Nano Lett.* **9** 3012–3015

[9] Lee C, Wei X, Kysar J W and Hone J 2008 Measurement of the elastic properties and intrinsic strength of monolayer graphene *Science* **321** 385–388

[10] Smalley R E 1997 Discovering the fullerenes *Review of Modern Physics* **69** 723–730

[11] Morris D G 2001 *Stereochemistry* Royal Society of Chemistry, Cambridge

[12] Kroto H, Heath J, O'Brien S, Curl R and Smalley R 1985 C60: Buckminsterfullerene *Nature* **318** 162–163

[13] Iijima S 1991 Helical microtubules of graphitic carbon *Nature* 354 56–58

[14] Novoselov K S, Geim A K, Morozov S V, Jiang D, Zhang Y, Dubonos S V, Grigorieva I V and Firsov A A 2004 Electric field effect in atomically thin carbon films *Science* **306** 666–669

[15] Peierls R E 1935 Quelques proprieties typiques des corpses solides *Ann. I. H. Poincare* **5** 177–222

[16] Landau L D and Lifshitz E M 1980 *Statistical Physics Part I* Pergamon Press, Oxford

[17] Mermin N D Crystalline order in two dimensions 1968 *Phys. Rev. B* **176** 250–254

[18] Fasolino A, Los J H and Katsnelson M I 2007 Intrinsic ripples in graphene *Nature Materials* **6** 858–861

[19] Meyer J C, Geim A K, Katsnelson M I, Novoselov K S, Booth T J and Roth S 2007 The structure of suspended graphene sheets *Nature* **446** 60–63

[20] Pauling L 1960 *The Nature of the Chemical Bond* Cornell Univ. Press, NY

[21] Cynthia G Z 2007 *Handbook of Electrochemistry* Elsevier, UK

[22] Heyrovska R 2008 Atomic structures of graphene, benzene and methane with bond lengths as sums of the single, double and resonance bond radii of carbon arXiv:0804.4086 [physics.gen-ph]

[23] Schafhaeutl C 1840 On the combinations of carbon with silicon and iron and other metals, forming different species of cast iron, steel, and malleable iron *Phil. Mag.* **16** 570–590

[24] Brodie B C 1859 On the atomic weight of graphite *Phil. Trans. R. Soc. Lond.* **149** 249–259

[25] Boehm H P, Clauss A, Fischer G and Hofmann U 1962 Surface properties of extremely thin graphite lamellae *Proceeding of the 5th Conference on Carbon, Pergamon Press* 73–80

[26] Eswaraiah V, Aravind S S J and Ramaprabhu S 2011 Top down method for synthesis of highly conducting graphene by exfoliation of graphite oxide using focused solar radiation *J. Mater. Chem.* **21** 6800–6803

[27] EI-Kady M F, Strong V, Dubin S and Kaner R B 2012 Laser scribing of high-performance and flexible graphene-based electrochemical capacitors *Science* **335** 1326–1330

[28] Roddaro S, Pingue P, Piazza V, Pellegrini and Beltram F 2007 The optical visibility of graphene: Interference colors of ultrathin graphite on SiO_2 *Nano Lett.* **7** 2707–2710

[29] Bae S S 2010 Roll-to-roll production of 30-inch graphene films for transparent electrodes *Nature Nanotech.* **5** 574–578

[30] Kim K S, Zhao Y, Jang H, Lee S Y, Kim J M, Kim K S, Ahn J H, Kim P, Choi J Y and Hong B H 2009 Large-scale pattern growth of graphene films for stretchable transparent electrodes *Nature* **457** 706–710

[31] Grneis A, Kummer K and Vyalikh D V 2009 Dynamics of graphene growth on a metal surface: a time dependent photoemission study *New Journal of physics* **11** 073050

[32] Sankaran R M 2011 *Plasma processing of nanomaterials* CRC press, USA

[33] Charrier A, Coati A, Argunova T, Thibaudau F, Garreau Y, Pinchaux R, Forbeaux I, Debever M, Sauvage-Simkin M and Themlin J M 2002 Solid-state decomposition of silicon carbide for growing ultra-thin heterepitaxial graphite films *J. App. Phys.* 92 2479–2484

[34] Berger C, Song, Z, Li T, Li X, Ogbazghi A Y, Feng R, Dai Z, Marchenkov A N, Conrad E H, First P N and de Heer W A 2004 Ultrathin epitaxial graphite: 2D electron gas properties and a route toward graphene-based nanoelectronics *J. Phys. Chem. B* **108** 19912–19916.

[35] Moreau F, Ferrer J, Vignaud D, Gody S and Wallart X 2010 Graphene growth by molecular beam epitaxy using solid carbon source *Phys. Status Solidi A* **207** 300–303

[36] N'Diaye T, Coraux J, Plasa T N, Busse C and Michely T 2008 Structure of epitaxial graphene on Ir(111) *New J. Phys.* **10** 043033

[37] Xiaolin L, Xinran W, Li Z, Sangwon L, Hongjie D 2008 Chemically derived, ultrasmooth graphene nanoribbon semiconductors *Science* **319** 1229–1232

[38] Hernandez Y, Nicolosi V, Lotya M, Blighe F M, Sun Z, De S, McGovern I T, Holland B, Byrne M, Gun'Ko Y K, Boland J J, Niraj P, Duesberg G, Krishnamurthy S, Goodhue R, Hutchison J, Scardaci V, Ferrari A C and Coleman J N High-yield production of graphene by liquid-phase exfoliate of graphite *Nature Nanotech.* **3** 563–568

[39] Li D, Windl W and Padture N 2009 Toward site-specific stamping of graphene *Advanced Materials* **21** 1243–1246

[40] Xiaogan L, Zengli F and Chou S Y 2007 Graphene transistors fabricated via transfer-printing in device active-areas on large wafer *Nano Lett.* **7** 3840–3844

[41] Sidorov A N, Yazdanpanah M M, Jalilian R, Ouseph P J, Cohn R W and Sumanasekera G U 2007 Electrostatic deposition of graphene *Nanotechnology* **18** 135301

[42] Liang X, Chang A S P, Zhang Y, Harteneck B D, Choo Hyuck, Olynick D L and Cabrini S 2008 Electrostatic force assisted exfoliation of prepatterned few-layer graphenes into device sites *Nano Lett.* **9** 467–472

[43] Kosynkin D V, Higginbotham A L, Sinitskii A, Lomeda J R, Dimiev A, Price B K, and Tour J M 2009 Logitudinal unzipping of carbon nanotubes to form graphene nanoribbons *Nature* **458** 872–876

[44] Jiao L, Zhang L, Wang X, Diankov G and Dai H 2009 Narrow graphene ribbons from from carbon nanotubes *Nature* **458** 877–880

[45] Choucair M, Thordarson P and Stride J A 2008 Gram-scale production of graphene on solvothermal synthesis and sonication *Nature Nanotech.* **4** 30–33

[46] Chakrabarti A, Lu J, Skrabutenas J C, Xu T, Xiao Z, Maguire J A and Hosmane N S 2011 Conversion of carbondioxide to few-layer graphene *J. Mater. Chem.* **21** 9491–9493

[47] Wallace P R 1947 The band theory of graphite *Phy. Rev.* **71** 622–634

[48] Castro Neto A H, Guinea F, Peres N M R, Novoselov K S and Geim A K The electronic properties of graphene *Rev. Mod. Phys.* **81** 110–155

[49] Wilson M 2006 Electrons in atomically thin carbon sheets behave like massless particles *Physics Today* **59** 21–23

[50] Chen J H, Jang C, Xiao S, Ishigami M and Fuhrer M S 2008 Intrinsic and extrinsic performance limits of graphene devices on SiO_2 *Nature Nanotech.* **3** 206–209

[51] Novoselov K S, Geim A K, Morozov S V, Jiang D, Katnelson M I, Grigorieva I V, Dubonos S V and Firsov A A 2005 Two-dimensional electron gas of massless Dirac fermions in graphene *Nature* **438** 197–200

[52] Novoselov K S, CannMc E, Morozov S V, Fal'ko V I, Katsnelson M I, Zeitler U, Jiand D, Schedin F and Geim A K 2006 Unconvenstional quantum Hall effect and Berry's phase of 2_{π} in bilayer graphene *Nat. Phys.* **2** 177–180

[53] Chen S, Wu Q, Mishra C, Kang J, Zhang H, Cho K, Weiwei C, Balandin A A and Ruoff R S 2012 Thermal conductivity of isotopically modified graphene *Nat. Mat.* **11** 203–207

[54] Novoselov K S, Jiang Z, Zhang Y, Morozov S V, Stormer H L, Zeitler U, Mann J C, Boebinger G S, Kim P and Geim A K 2007 Room-temperature quantum Hall effect in graphene *Science* **315** 1379

[55] First graphene integrated circuit 2011 *IEEE Spectrum*

[56] Matyba P, Yamaguchi H, Eda G, Chhowalla M, Edman L and Robinson N D 2010 Graphene and mobile ions: the key to all-plastic, solution-processed light-emitting devices *ACS Nano* **4** 637–642

[57] Kelly B T Physics of Graphite 1981 *Applied Science, London*

[58] Novoselov K S, Jiang D, Schedin F, Booth T J, Khotkevich V V, Morozov S V and Geim A K 2005 Two-dimensional atomic crystals *Proc. Natl Acad. Sci. USA* **102** 10451–10453

[59] Binning G, Quate C F, Gerber Ch 1986 Atomic force microscope *Phys. Rev. Lett.* **56** 930–933

[60] http://en.wikipedia.org/wiki/Atomic_force_microscopy

[61] http://asdlib.orge/onlineArticle/ecourseware/Bullen/SPMModule_BasicThoryAFM.pdf

[62] http://www.nobelprize.org/nobel_prizes/physics/laureates/1930/ram-lecture.pdf

[63] http://bwtek.com/ram-theory-of-raman-scattering/

[64] Ferrari A C, Meyer J C, Scardaci V, Casiraghi C, Lazzeri M, Mauri M, Piscanec S, Jiang Da, Novoselov K S, Roth S and Geim A K 2006 Raman spectrum of graphene and graphene layers *Phys. Rev. Lett.* **97** 187401

[65] Wang Y Y, Ni Z H, Yu T, Wang H M, Wu Y H, Chen W, Wee A T S and Shen Z X 2008 Raman studies of monolayer graphene: the substrate effect *J. Phys. Chem. C* **112** 10637–10640

[66] Hao Y, Wang Y, Wang L, Ni Z, Wang Z, Wang R, Koo C K, Shen Z and Thong J T L 2010 Probing layer number and stacking order of few-layer graphene by Raman spectroscopy *Small* **6** 195–200

[67] http://www.smt.zeiss.com/C12256E4600307C70/ContainerTitel/Orion_Plus/$File/orion.html

[68] Pickard D, Mathew S, Özyilmaz B , Thong J T L, Venkatesan T, Viswanathan V and Wang Z. –Q, 2009 Direct patterning and imaging of graphene structures with a helium ion microscope *International Conference on Electron, Ion, Photon beam technology and nanofabrication, Florida, USA* May 26–30

[69] Bunch J S, van der Zande A M, Verbridge S S, Frank I W, Tanenbaum D M, Parpia J M, Craighead H G and McEuen P L 2007 Electromechanical resonators from graphene sheets *Science* **315** 490–493

[70] Garcia-Sanchez D, Van Der Zande A M, San Paulo A, Lassagne B, McEuen P L and Bachtold A 2008 Imaging mechanical vibrations in suspended graphene sheets *Nano Lett.* **8** 1399–1403

[71] Chen C, Rosenblatt S, Bolotin K L, Kalb W, Kim P, Kymissis I, Stormer H L, Heinz T F and Hone J 2009 Performance of monolayer graphene nanomechanical resonators with electrical readout *Nat. Nanotech.* **4** 861–867

[72] Robinson J T, Zalalutdinov M, Baldwin J W, Snow E S, Wei Z, Sheehan P and Houston B H 2008 Wafer-scale reduced graphene oxide films for nanomechanical devices *Nano Lett.* **8** 3441–3445

[73] Sone H, Fujinuma Y and Hosaka S 2004 Picogram mass sensor using resonance frequency shift of cantilever *Jpn. J. Appl. Phys.* **43** 3648–3651

[74] Neek-Amal M and Peeters F M 2010 Linear reduction of stiffness and vibration frequencies in defected circular monolayer graphene *Phys. Rev. B* **81** 235437

[75] Hemmasizadeh A, Mahzoon M, Hadi E and Khandan R 2008 A method for developing the equivalent continuum model of a single layer graphene sheet *Thin Solid Films* **516** 7636–7640

[76] Lu Q and Huang R 2009 Nonlinear mechanics of single-atomic-layer graphene sheets *Int. J. Appl. Mech.* **1** 443–467

[77] Sadeghi M and Naghdabadi R 2010 Nonlinear vibrational analysis of single-layer graphene sheets *Nanotechnology* **21** 105705

[78] Scarpa F, Adhikari S, Gil A J and Remillat C 2010 The bending of single layer graphene sheets: the lattice versus continuum approach *Nanotechnology* **21** 125702

[79] Frank I W, Tanenbauma D M, van der Zande A M and McEuen P L 2007 Mechanical properties of suspended graphene sheets *J. Vac. Sci. Technol. B* **25** 2558–2561

[80] Poot M and van der Zant H S J 2008 Nanomechanical properties of few-layer graphene membranes *Appl. Phys. Lett.* **92** 063111

[81] Bunch J S, Verbridge S S, Alden J S, van der Zande A M, Parpia J M, Craighead H G and McEuen P L 2008 Impermeable atomic membranes from graphene sheets *Nano Lett.* **8** 2458–2462

[82] Timoshenko S P and Woinkowsky-Krieger S 1959 Theory of plates and shells *McGraw-Hill, New York*

[83] Timoshenko S P, Young D H and Weaver Jr. W 1974 Vibration Problems in Engineering *John Wiley and Sons, New York* 496–502

[84] Sone H, Fujinuma Y and Hosaka S 2004 Picogram mass sensor using resonance frequency shift of cantilever *Jpn. J. Appl. Phys.* 3648–3651

[85] Ismail A K, Burdess J S, Harris A J, McNeil C J, Hedley J, Chang S C and Suarez G 2006 The principle of a MEMS circular diaphragm mass sensor *J. Micromech. Microeng.* **16** 1487–1493

[86] Meirovitch L 1986 Elements of vibration analysis 2nd ed. *McGraw Hill, New York*

[87] Sakhaee-Pour A, Ahmadian M T and Vafai A 2008 Application of single-layered graphene sheets as mass sensors and atomistic dust detectors *Solid State Commun.* **145** 168–172

[88] Adhikari S and Chowdhury R 2012 Zeptogram sensing from gigahertz vibration: Graphene based nanosensor *Physica E* **44** 1528–1534

[89] Kwon O K, Kim K S, Park J and Kang J W 2013 Molecular dynamic modeling and simulation of graphene-nanoribbon-resonator-based nanobalance as yoctogram resolution detector *Comput. Mater. Sci.* 67 329–333

[90] Schedin F, Geim A K, Morozov S V, Hill E W, Blake P, Katsnelson M I and Novoselov K S 2007 Detection of individual gas molecules adsorbed on graphene *Nature Materials* **6** 652–655

[91] Lemme M C, Echtermeyer T J, Baus M and Kurz H 2007 A graphene field-effect device *IEEE Elec. Dev. Lett.* **28** 282–284

[92] Williams J R, DiCarlo L and Marcus C M 2007 Quantum hall effect in a gate-controlled p-n junction of graphene *Science* **317** 638–641

[93] Barone V, Hod O and Scuseria G E 2006 Electronic structure and stability of semiconducting graphene nanoribbons *Nano Lett.* **6** 2748–2754

[94] Han M Y, Özyilmaz B, Zhang Y and Kim P 2007 Energy band-gap engineering of graphene nanoribbons *Phys. Rev. Lett.* **98** 206805

[95] Wang Z F, Shi Q W, Li Q, Wang X, Hou J G, Zheng H 2007 Z-shaped graphene nanoribbon quantum dot device *Appl. Phy. Lett.* **91** 053109

[96] Özyilmaz B, Jarillo H P, Efetov D and Kim P 2007 Electronic transport in locally gated graphene nanoconstrictions *Appl. Phys. Lett.* **91** 192107

[97] Liu M, Yin X, Ulin-Avila E, Geng B, Zentgraf T, Ju L, Wang F and Zhang X 2011 A graphene-based broadband optical modulator *Nature* **474** 64–67

[98] Wu J, Agrawal M, Becerril H A, Bao Z, Liu Z, Chen Y and Peumans P 2010 Organic light-emitting diodes on solution-processed graphene transparent electrodes *ACS Nano* **4** 43–48

[99] Hill E W, Geim A K, Novoselov K, Schedin F, Blake P 2007 Graphene spin valve devices *IEEE Trans. Magn.* **42** 2694–2696

[100] van der Zande A M, Barton R A, Alden J S, Ruiz-Vargas C S, Whitney W S, Pham P H Q, Parks J S, Parpia J M, Craighead H G, and McEuen P L 2010 Large - scale arrays of single - layer graphene resonators *Nano Lett.* **10** 4869–4873

[101] Wong C -L, Annamalai M, Wang Z -Q and Palaniapan M Characterization of nanomechanical graphene drum structures 2010 *J. Micromech. Microeng.* **20** 115029

[102] Zan R, Muryn C, Bangert U, Mattocks P , Wincott P, Vaughan D, Li X, Colombo L, Ruoff R S, Hamilton B and Novoselov K S 2012 Scanning tunneling microscopy of suspended graphene *Nanoscale* **4** 3065–3068

[103] Xu P, Yang Y, Barber S D, Ackerman M L, Schoelz J K, Qi D, Kornev I A, Dong L, Bellaiche L, Barraza-Lopez S, and Thibado P M 2012 Atomic control of strain in freestanding graphene *Phys. Rev. B* **85** 121406(R)

[104] Ni Z H, Wang H M, Kasim J, Fan H M, Yu T, Wu Y H, Feng Y P and Shen Z X 2007 Graphene thickness determination using reflection and Contrast spectroscopy *Nano Lett.* **7** 2758–2763

[105] Nemes-Incze P, Osvath Z Kamaras K and Biro L P 2008 Anomalies in thickness measurements of graphene and few layer graphite crystals by tapping mode atomic force microscopy *Carbon* **46** 1435–1442

[106] Chen J H, Cullen W G, Jang C, Fuhrer M S and Williams E D 2008 Defect scattering in graphene *Phy. Rev. Lett.* **102** 236805

[107] Canc□ado L G, Jorio A, Martins Ferreira E H, Stavale F, Achete C A, Capaz R B, Moutinho M V O, Lombardo A, Kulmala T S and Ferrari A C 2011 Quantifying defects in graphene via Raman spectroscopy at different excitation energies *Nano Lett.* **11** 3190–3196

[108] Krauss B, Lohmann T, Chae D -H, Haluska M, von Klitzing K and Smet J H 2009 Laser-induced disassembly of a graphene single crystal into a nanocrystalline network *Phy. Rev. B* **79** 165428

[109] Graf D, Molitor F, Ensslin K, Stampfer C, Jungen A, Hierold C and Wirtz L 2007 Spatially resolved Raman spectroscopy of single- and few-layer graphene *Nano Lett.* **7** 238–242

[110] Marco S and Ivan B Tutorial: Mapping adhesion forces and calculating elasticity in contact-mode AFM 2006 *Microscopy and Analysis* **20** S5–S8

[111] Landau L D, Pitaevskii L P, Lifshitz E M and Kosevich A M 1959 Theory of Elasticity *Butterworth-Heinemann*

[112] Gupta S S and Batra R C 2010 Elastic Properties and frequencies of free Vibrations of single-layer graphene sheets *J. of Comp. and Theo. Nanoscience* **7** 2151–2164

[113] Koenig S P, Boddeti N G, Dunn M L and Bunch J S 2011 Ultrastrong adhesion of graphene membranes *Nature Nanotechnology* **6** 543–546

[114] Duan W H and Wang C M 2009 Nonlinear bending and stretching of a circular graphene sheet under a central point load *Nanotechnology* **20** 075702

[115] Konstantinova E, Dantas S O and Barone P M V B 2006 Electronic and elastic properties of two-dimensional carbon planes *Phys. Rev. B* **74** 035417

[116] Hernandex E, Goze C, Bernier P and Rubio A 1998 Elastic properties of single wall carbon nanotubes *Phys. Rev. Lett.* **80** 4502–4505

[117] Lee J U, Yoon D and Cheong H 2012 Estimation of Young's modulus by Raman *31st International conference on physics of semiconductors* (ICPS 2012)

[118] Bao W X, Zhu C C and Cui W Z 2004 Simulation of Young's modulus of single-walled carbon nanotubes by molecular dynamics *Physica B* **352** 156–163

[119] Zhao H, Min K, and Aluru N R 2009 Size and chirality dependent elastic properties of graphene nanoribbons under uniaxial tension *Nano Lett.* **9** 3012–3015

[120] Gere J M and Timoshenko S P 1997 Mechanics of Materials *PWS Pub Co., Boston*

[121] Mathew S, Chan T K, Zhan D, Gopinadhan K, Barman A -R, Breese M B H, Dhar S, Shen Z X, Venkatesan T and John Thong T L 2011 The effect of layer number and substrate on the stability of graphene under MeV proton beam irradiation *Carbon* **49** 1720–1726

[122] Radisavljevic B, Radenovic A, Brivio J, Giacometti V, Kis A 2011 Single-layer MoS_2 transistors *Nature Nanotech* **6** 147–150

[123] Tributsch H and Bennett J C 1977 Electrochemistry and photochemistry of MoS_2 layer crystals *J. Electroanal. Chem.* **81** 97–111

[124] Radisavljevic B, Whitwick M B and Kis A 2011 Integrated circuits and logic operations based on single-layer MoS_2 *ACS Nano* **5** 9934–9938

[125] Castellanos-Gomez A, Poot M, Steele G A, van der Zant H S, Agraït N, Rubio-Bollinger G 2012 Mechanical properties of freely suspended semiconducting graphene-like layers based on MoS_2 *Nanoscale Res. Lett.* **7** 1–7

[126] Martin J, kerman N, Ulbricht G, Lohmann T, Smet J H, Klitzing K V and Yacoby A 2008 Observation of electron–hole puddles in graphene using a scanning single-electron transistor *Nature Physics* **4** 144–148

[127] Deshpande A, Bao W, Miao F, Lau C N and LeRoy B J 2009 Spatially resolved spectroscopy of monolayer graphene on SiO_2 *Phys. Rev. B* **79** 205411

[128] Katsnelson M I and Geim A K 2008 Electron scattering on microscopic corrugations in graphene *Phil. Trans. R. Soc. A* **366** 195–204

[129] Fallahazad B, Seyoung K, Colombo L and Tutuc E 2010 Dielectric thickness dependence of carrier mobility in graphene with HfO_2 top dielectric *Appl. Phys. Lett.* **97** 123105

[130] Huertas-Hernando D, Guinea F and Brataas A 2006 Spin-orbit coupling in curved graphene, fullerenes, nanotubes, and nanotube caps *Phys. Rev. B* **74** 155426

[131] Levy N, Burke S A, Meaker K L, Panlasigui M, Zettl A, Guinea F, Neto A H C and Crommie M F 2010 Strain-induced pseudo-magnetic fields greate than 300 Tesla in graphene nanobubbles *Science* **329** 544–547

[132] Martinez J C, Jalil M B A and Tan S G 2012 Giant faraday and kerr rotation with strained graphene *Opt. Lett.* **37** 3237–3239

[133] Baimova J A, Dmitriev S V, Zhou K, Savin A V 2012 Strain-induced ripples in graphene nanoribbons with clamped edges *Physica Status Solidi B* **249** 7 1393–1398

[134] Wang Z and Devel M 2011 Periodic ripples in suspended graphene *Phys. Rev. B* **83** 125422

[135] Brey L and Palacios J J 2008 Exchange-induced charge inhomogeneities in rippled neutral graphene *Phys. Rev. B* **77** 041403

[136] de Juan F, Cortijo A and Vozmediano M A H 2007 Charge inhomogeneities due to smooth ripples in graphene sheets *Phys. Rev. B* **76** 165409

[137] Wehling T O, Balatsky A V, Tsvelik A M, Katsnelson M I and Lichtenstein A I 2008 Midgap states in corrugated graphene: ab initio calculations and effective field theory *Europhys. Lett.* **84** 17003

[138] Guinea F, Katsnelson M I and Vozmediano M A H 2008 Midgap states and charge inhomogeneities in corrugated graphene *Phys. Rev. B* **77** 075422

[139] Guinea F, Horovitz B and Le Doussal P 2008 Gauge field induced by ripples in graphene *Phys. Rev. B* **77** 205421

[140] Bao W, Miao F, Chen Z, Zhang H, Jang W, Dames C and Lau C N 2009 Controlled ripple texturing of suspended graphene and ultrathin graphite membranes *Nature Nanotech.* **4** 562–566

[141] Kim E and Neto A H C 2008 Graphene as an electronic membrane *Europhys. Lett.* **84** 57007

[142] Neek-Amal M and Peeters F M 2010 Graphene nano ribbons subjected to axial stress *Phys. Rev. B* **82** 085432

[143] Zhang Z, Duan W H and Wang C M 2012 Tunable wrinkling pattern in annular graphene under circular shearing at inner edge *Nanoscale* **4** 5077–5081

[144] Fang T H, Wang T H, Yang J C and Hsiao Y J 2011 Mechanical characterization of nanoindented graphene via molecular dynamics simulations *Nanoscale Res. Lett.* **6** 1–10

[145] Wang C Y, Mylvaganam K and Zhang L C 2009 Wrinkling of monolayer graphene: a study by molecular dynamics and continuum plate theory *Phys. Rev. B* **80** 155445

[146] Huang X and Zhang S 2011 Morphologies of monolayer graphene under indentation *Model. Simul. Mater. Sci. Eng.* **19** 054004

[147] Smolyanitsky A and Tewary V K, *arXiv:1208.0852v1* [con-mat.mes-hall]

[148] Yi W, Rong Y, Zhiwen S, Lianchang Z, Dongxia S, Enge W and Guangyu Z 2011 Super-elastic graphene ripples for flexible strain sensors *ACS Nano* **5**, 3645–3650

[149] Pereira V M and Neto A H C 2009 Strain engineering of graphene's electronic structure *Phys. Rev. Lett.* **103** 046801

[150] Zhan D, Yan J, Lai L, Ni Z, Liu L, Shen Z 2012 Engineering the electronic structure of graphene *Adv. Mater.* **24** 4055–4069

[151] Morozov S.V, Novoselov K S, Katsnelson M I, Schedin F, Ponomarenko L A, Jiang D and Geim A K 2006 Strong suppression of weak localization in graphene *Phys. Rev. Lett.* **97** 016801

[152] Singh A and Richard H G, American Physical Society, APS March Meeting (2012) http://meetings.aps.org/link/BAPS.2012.MAR.X11.4

[153] Xu K, Cao P G and Heath J R 2009 Scanning tunneling microscopy characterization of the electrical properties of wrinkles in exfoliated graphene monolayers *Nano Lett.* **9** 4446–4451

[154] Zhang Y, Tang T T, Girit C, Hao Z, Martin M C, Zettl A, Crommie M F, Shen Y R and Wang F 2009 Direct observation of a widely tunable bandgap in bilayer graphene *Nature* **459** 820–823

[155] Oostinga J B, Heersche H B, Liu X L, Morpurgo A F and Vandersypen L M K 2008 Gate-induced insulating state in bilayer graphene devices *Nature Mater.* **7** 151–157

[156] Zhou K and Zhu J 2010 Transport in gapped bilayer graphene: the role of potential fluctuations *Phys. Rev. B* **82** 081407(R)

[157] Taychatanapat T and Jarillo-Herrero P 2010 Electronic transport in dual-gated bilayer graphene at large displacement fields *Phys. Rev. Lett.* **105** 166601

[158] Yan J and Fuhrer M S 2010 Charge transport in dual gated bilayer graphene with Corbino geometry *Nano Lett.* **10** 4521–4525

[159] Mak K F, Lui C H, Shan J and Heinz T F 2009 Observation of an electric-field induced band gap in bilayer graphene by infrared spectroscopy *Phys. Rev. Lett.* **102** 256405

[160] Yan J, Kim M H, Elle J A, Sushkov A B, Jenkins G S, Milchberg H M, Fuhrer M S and Drew H D 2012 Dual-gated bilayer graphene hot-electron bolometer *Nature Nanotech.* **7** 472–478

[161] Mounet N and Marzari N 2005 First-principles determination of the structural, vibrational and thermodynamic properties of diamond, graphite, and derivatives *Phys. Rev. B* **71** 205214

[162] de Andres P L, Guinea F and Katsnelson M I 2012 Bending modes, anharmonic effects, and thermal expansion coefficient in single-layer and multilayer graphene *Phys. Rev. B* **86** 144103

[163] Okada Y and Tokumaru Y 1984 Precise determination of lattice parameter and thermal expansion coefficient of silicon between 300 and 1500 K *J. Appl. Phys.* **56** 314–320

[164] Miranda R and Vázquez de Parga A L 2009 Graphene: Surfing ripples towards new devices *Nature Nanotech.* **4** 549–550

[165] Bao W, Miao F, Chen Z, Zhang H, Jang W, Dames C and Lau C N 2009 Controlled ripple texturing of suspended graphene and ultrathin graphite membranes (supplementary information) *Nature Nanotech.* DOI: 10.1038/NNANO.2009.191

[166] Clavel M, Poiroux T, Mouis M, Becerra L, Thomassin J L, Zenasni A, Lapertot G, Rouchon D, Lafond D and Faynot O 2011 Influence of annealing temperature on the

performance of graphene / SiC transistors with high-k / metal gate *Ultimate integration on silicon (ULIS), 12th* international conference 1–4

[167] Sedelnikova O V, Bulusheva L G and Okotrub A V 2011 Ab initio study of dielectric response of rippled graphene *J. Chem. Phys.* **134** 244707

[168] Georgiou T, Britnell L, Blake P, Gorbachev R V, Gholinia A, Geim A K, Casiraghi C and Novoselov K S 2011 Graphene bubbles with controllable curvature *Appl. Phys. Lett.* **99** 093103

[169] Zhou Y B, Liao Z M, Wang Y F, Duesberg G S, Xu J, Fu Q, Wu X S and Yu D P 2010 Ion irradiation induced structural and electrical transition in graphene *J. Chem. Phys.* **133** 234703

[170] Mathew S, Chan T K, Zhan D, Gopinadhan K, Barman A -R, Breese M B H, Dhar S, Shen Z X, Venkatesan T and Thong J T L 2011 The effect of layer number and substrate on the stability of graphene under MeV proton beam irradiation *Carbon* **49** 1720–1726

[171] Ahlgren E H, Kotakoski J, Lehtinen O and Krasheninnikov A V 2012 Ion irradiation tolerance of graphene as studied by atomistic simulations *Appl. Phys. Lett.* **100** 233108

[172] Ramos M A, Barzola-Quiquia J, Esquinazi P, Muñoz-Martin A, Climent-Font A and García-Hernández M 2010 Magnetic properties of graphite irradiated with MeV ions *Phys. Rev. B* **81** 214404

[173] CompagniniG, Giannazzo F, Sonde S, Raineri V, Rimini E 2009 Ion irradiation and defect formation in single layer graphene *Carbon* **47** 3201–3207

[174] Lehtinen O, Kotakoski J, Krasheninnikov A V, Tolvanen A, Nordlund K and Keinonen J 2010 Effects of ion bombardment on a two-dimensional target: Atomistic simulations of graphene irradiation *Phys. Rev. B* **81** 153401

[175] Stolyarova E, Stolyarov D, Bolotin K, Ryu S, Liu L, Rim K T, Klima M, Hybertsen M, Pogorelsky I, Pavlishin I, Kusche K, Hone J, Kim P, Stormer H L, Yakimenko V, and Flynn G 2009 Observation of graphene bubbles and effective mass transport under graphene films *Nano Lett.* **9** 332–337

[176] Tapasztó L, Dobrik G, Nemes-Incze P, Vertesy G, Lambin Ph and Biró L P 2008 Tuning the electronic structure of graphene by ion irradiation *Phys. Rev. B* **78** 233407

[177] Childres I, Jauregui L A, Foxe M, Tian J, Jalilian R, Jovanovic I and Chen Y P 2010 Effect of electron-beam irradiation on graphene field effect devices *Appl. Phys. Lett.* **97** 173109

[178] Lopez J J, Greer F and Greer J R 2010 Enhanced resistance of single-layer graphene to ion bombardment *J. Appl. Phys.* **107** 104326

[179] Krasheninnikov A V and Nordlund K 2010 Ion and electron irradiation-induced effects in nanostructured materials *J. Appl. Phys.* **107** 071301

[180] Jones J D, Mahajan K K, Williams W H, Ecton P A, Mo Y and Perez J M 2010 Formation of graphane and partially hydrogenated graphene by electron irradiation of adsorbates on graphene *Carbo*n **48** 2335–2340

[181] Moser J, Verdaguer A, Jimenez D, Barreiro A and Bachtold A 2008 The environment of graphene probed by electrostatic force microscopy *Appl. Phys. Lett.* **92** 123507

[182] Basko D M, Piscanec S and Ferrari A C 2009 Electron-electron interactions and doping dependence of the two-phonon Raman intensity in graphene *Phys. Rev. B* **80** 165413

[183] Lucchese M M, Stavale F, Martins Ferreira E H, Vilani C, Moutinho M V O, Capaz R B, Achete C A and Jorio A 2009 Quantifying ion-induced defects and Raman relaxation length in graphene *Carbon* **48** 1592–1597

[184] Ziegler J F, Biersack J P and Littmark U 1995 The stopping and range of ions in matter *Pergamon Press, New York*

[185] Ishigami M, Chen J H, Cullen W G, Fuhrer M S and William E D 2007 Atomic structure of graphene on SiO_2 *Nano Lett.* **7** 1643–11648

[186] Tapaszto L, Dobrick G, Lambin P and Biro L P 2008 Tailoring the atomic structure of graphene nanoribbons by scanning tunnelling microscope lithography *Nat. Nanotech.* **3** 397–401

[187] Gierak B, Schiedt B, Lucot D, Madouri A, Bourhis E, Patriarche G, Ulysse C, Lafosse X, Auvray L, Bruchhaus L, Bauerdick S, Biance A L and Jede R 2009 Challenges and oppurtunities for focussed ion beam processing at nano-scale *Microsc. Microanal.* **15** 320–321

[188] Fischbein M D, Drndic M 2008 Electron beam nanosculpting of suspended graphene sheets *Appl. Phys. Lett.* **93** 113107

[189] Awtar S and Slocum A H 2005 Design of Flexure Stages Based on a Symmetric Diaphragm Flexure *Proc. ASPE 2005 Annual Meeting, Norfolk, Virginia*, USA, Paper 1803

[190] http://phys.columbia.edu/~millis/1900/readings/graphene.pdf

LIST OF PUBLICATIONS

[1] Annamalai M, Palaniapan M, Wong W K 2009 Acoustic phonon characterisation of fixed-fixed beam MEMS switch *Electronics Letters* **45** 464–466

[2] Wong C -L, Annamalai M, Wang Z -Q and Palaniapan M 2010 Characterization of nanomechanical graphene drum structures 2010 *J. Micromech. Microeng.* **20** 115029

[3] Annamalai M, Mathew S, Jamali M, Zhan D and Palaniapan M 2012 Elastic and nonlinear response of nanomechanical graphene devices *J. Micromech. Microeng.* **22** 105024

[4] Annamalai M, Mathew S, Viswanathan V, Fang C, Pickard D S and Palaniapan M 2011 Design, fabrication and Helium Ion Microscope patterning of suspended nanomechanical graphene structures for NEMS applications *Solid-State Sensors, Actuators and Microsystems Conference (TRANSDUCERS)* 2578–2581

[5] Annamalai M, Mathew S, Jamali M, Zhan D and Palaniapan M 2013 The effects of annealing on ripple texture and mechanical properties of suspended bilayer graphene *J. Phys. D: Appl. Phys.* **46** 145302

[6] Annamalai M, Mathew S, Jamali M, Zhan D and Palaniapan M Nanoindentation induced ripple formation in few-layer graphene (submitted to *Appl. Surf. Sci.*)

[7] Annamalai M, Mathew S, Chan T K, Da Z, Breese M B H, Palaniapan M and Venkatesan T Mechanical properties of suspended graphene under keV He ion irradiation (to be submitted)